Universidade de São Paulo
Instituto de Astronomia, Geofísica e Ciências Atmosféricas
Departamento de Astronomia

Julia de Carvalho Santos

Methyl acetylene in G331.512-0.103: Looking at massive star formation through the lens of chemistry

São Paulo
2021

Julia de Carvalho Santos

Methyl acetylene in G331.512-0.103: Looking at massive star formation through the lens of chemistry

Thesis presented to the Department of Astronomy of Instituto de Astronomia, Geofísica e Ciências Atmosféricas of Universidade de São Paulo as a partial requirement to obtain a Master of Science degree.
Corrected version. The original printed version is available at IAG/USP

Research field: Astronomy
Advisor: Prof. Dr. Jacques R. D. Lépine
Co-advisor: Dr. Edgar Mendoza

São Paulo
2021

Acknowledgements

The pursuit of a graduate degree is never an easy journey, and I certainly did not expect it to be. However, the outbreak of a pandemic during the first year of my master's degree cannot be described as anything less than a colossal setback. From switching to having classes and meetings online, to the unrelenting uneasiness of an unprecedented and completely unpredictable global-health conjecture, this crisis has been a real challenge that will forever remain in the memories of those who survive it. Nonetheless, "life did not stop, and one had to live"(Leo Tolstoy). And so I lived, and wrote this thesis hoping that, in the future, I will be able to look back at this moment and feel a glimpse of pride.

I would like to first and foremost thank my parents, who provided me the support to pursue this arduous career path. I would also like to thank all of my friends, old and new, for the interesting conversations and, perhaps more importantly, the laughter. I want to thank Fabio, my love, who never ceased to believe in me, even when I did. Lastly, I would like to thank myself, however narcissistic it may sound. Heaven knows I struggled.

This study was financed in part by the Coordenação de Aperfeiçoamento de Pessoal de Nível Superior - Brasil (CAPES)

Esta tese/dissertação foi escrita em LaTeX com a classe IAGTESE, para teses e dissertações do IAG.

“If I were not the type of atheist who believes with unflinching faith in the purposelessness of life, who believes in the unrelenting chaos of a cold universe, who believes that life is a brutal cosmic accident, who believes there is no one watching and certainly no one pulling the strings, I would believe there is someone watching and pulling the strings, and that the someone or thing that has it out for me is indeed watching, watching, always watching, damn it.”

Charlie Kaufman - Antkind

Resumo

Nesta dissertação de mestrado, nós pretendemos explorar as propriedades físicas de regiões de formação estelar massiva através de seus espectros de emissão molecular, os quais têm a capacidade de prover informações importantes a respeito da fonte. Dessa forma, nós conduzimos um *survey* espectral de metil-acetileno (CH_3CCH) no *Hot Molecular Core/Outflow* massivo G331.512-0.103, usando o telescópio de 12 m APEX. As nossas observações resultaram na detecção de 41 linhas nítidas e não-contaminadas de CH_3CCH no intervalo de frequências entre 172 e 356 GHz. Através de uma análise assumindo o Equilíbrio Termodinâmico Local, na qual utilizamos diagramas rotacionais, determinamos T_{exc}=47.1±1.2 K, $N_{tot}(CH_3CCH)=6.9\pm0.5\times10^{15}$ cm^{-2} e $X[CH_3CCH/H_2]\approx(1.5–7.6)\times10^{-8}$ para uma região extensa de emissão ($\sim10''$). Nós observamos que as intensidades relativas das linhas com K=2 e K=3 em um determinado *K-ladder* apresentam uma forte correlação negativa com o número quântico J superior da transição (r=-0.84). Essa observação foi analisada em conjunto com simulações dos espectros rotacionais puros de CH_3CCH em diferentes temperaturas, juntamente com adaptações da técnica do diagrama rotacional. Os resultados indicaram que a emissão é caracterizada por um gradiente de temperaturas, com limites inferior e superior de ~40 e ~60 K, respectivamente. Além disso, as larguras das linhas e as velocidades dos picos apresentam, em geral, uma forte correlação com as frequências das transições, sugerindo que o gás mais quente também está associado a efeitos mais fortes de turbulência. As transições com K=0 apresentam uma assinatura cinemática ligeiramente diferente do resto das linhas, indicando que elas podem estar traçando uma componente distinta do gás. Nós especulamos que essa componente é caracterizada por temperaturas mais baixas, e portanto tamanhos maiores. No entanto, observações com maiores resoluções angulares são necessárias para verificar estas conclusões.

Abstract

In the present master's thesis, we aim to explore the physical properties of massive star-forming regions by means of their molecular emission spectra, which can provide powerful information on the source. Thus, we conducted a spectral survey of methyl acetylene (CH_3CCH) toward the Hot Molecular Core/massive outflow G331.512-0.103, using the APEX 12 m telescope. Our observations yielded the detection of 41 clear and uncontaminated rotational lines of CH_3CCH in the frequency range between 172–356 GHz. Through an analysis under the Local Thermodynamic Equilibrium (LTE) assumption, by means of rotational diagrams, we determined T_{exc}=47.1±1.2 K, $N_{tot}(CH_3CCH)=6.9\pm0.5\times10^{15}$ cm^{-2} and $X[CH_3CCH/H_2]\approx(1.5–7.6)\times10^{-8}$ for an extended emitting region ($\sim10''$). We observed that the relative intensities of the K=2 and K=3 lines within a given K-ladder are strongly negatively correlated to the transitions' upper J quantum number (r=-0.84). Pure rotational spectra of CH_3CCH were simulated at different temperatures, in order to explore this observation. Conjointly, adaptations to the rotational diagram technique were also employed. The results indicate that the emission is characterized by a non-negligible temperature gradient with upper and lower limits of ~40 and ~60 K, respectively. Moreover, the line widths and peak velocities show an overall strong correlation with their rest frequencies, suggesting that the warmer gas is also associated with stronger turbulence effects. The K=0 transitions present a slightly different kinematic signature than the remainder, indicating that they might be tracing a different gas component. We speculate that this component is characterized by lower temperatures, and therefore larger sizes. However, observations with higher angular resolution are imperative to verify our conclusions.

List of Figures

1.1 From van Dishoeck (2014). Formation and evolution of the interstellar ices. The H_2O-rich ice is shown in red, while the CO-rich ice is shown in blue. . 29

1.2 Sketch of the three major surface reaction mechanisms. From Herbst and van Dishoeck (2009). 29

1.3 Figure from Sadaghiani et al. (2020), showing the different fragmentation levels of the NGC 6334 star-forming complex from the scale of the filament down to the scale of individual dense cores and protostars. The colors indicate different densities—lighter colors correspond to lower densities, whereas darker colors indicate higher densities—as well as ionized gas (in orange). Vertical and horizontal orientations correspond to the Galactic latitude and longitude coordinates, respectively. The distribution is based on observations by Russeil et al. (2013). 31

1.4 Superimposed maps of the CH_3CN(5–4) traced HMC in the high-mass star-forming region IRAS 20126+4104 (grey scale) and the $C^{17}O$(2–1) traced surrounding molecular clump (contours). From Cesaroni 2005. 35

1.5 Zeroth moment maps of emission from G331, integrated in the range of the systemic velocity. The 862 μm continuum emission map is also shown (bottom right panel). From Hervías-Caimapo et al. (2019). 38

1.6 Schematic view of the physical model proposed for G331. Based on the models of Merello et al. (2013a); Duronea et al. (2019); Hervías-Caimapo et al. (2019) 39

1.7 Transitions between the energy levels E_i and E_j of a given species and the Einstein probabilities. Adapted from Wilson et al. (2009). 42

1.8 Sketch of the ellipsoid of inertia of H_2CO adapted from Levine (1975). Each cross-section contains two principal axes. 44
1.9 Overview of commonly used molecular diagnostics and the respective range of physical conditions that they trace. From Genzel 1991. 47
1.10 3D models of the molecules CH_3CCH, CH_3CN and CH_3OH, for comparison purposes. Symmetric rotors: a) methyl acetylene (CH_3CCH) and b) acetonitrile (CH_3CN). Asymmetric rotor: c) methanol (CH_3OH). The white, gray, blue and red spheres correspond to the H, C, N and O atoms, respectively. Those three molecules have been observed in G331 (Hervías-Caimapo et al., 2019), and play an important role in the inference of the physical conditions of HMCs and related sources. 50
1.11 Rotational energy levels of CH_3CCH. Adapted from Kuiper et al. (1984). . 52

2.1 APEX 12 m telescope. Credit: ESO/B. Tafreshi 54
2.2 Gaussian fitting of the $CH_3CCH(10_0–9_0)$ line (green) over the observed spectrum (black). The upper and lower x-axes are given in frequency units (MHz) and velocity units (km s^{-1}), respectively. The y-axis is given in temperature units (K). 59

3.1 Spectra of CH_3CCH exhibiting the different K-ladders identified from J=10–9 to J=18–17. For each spectrum, a linear baseline was subtracted. K-level transitions are indicated for the J=10–9 K-ladder. 64
3.2 Plot of A_{ij} versus E_{up} of the observed CH_3CCH lines. The transitions are grouped according to their K quantum number: blue cross-marks correspond to transitions with K=0, magenta squares correspond to K=1, green circles correspond to K=2, red triangles correspond to K=3 and yellow diamonds correspond to K=4. 66
3.3 *Upper panel:* Rotational diagram of the CH_3CCH lines for a source size of 5″. Least squares fits with and without opacity corrections are shown in red and blue, respectively. *Lower panel:* Same as the upper panel, but for a source size of 10″. 67

3.4 Optical depth (τ) vs. E_u of the CH_3CCH lines assuming a source size of 10″. Blue cross marks represent transitions with K=0 and K=1, red circles represent transitions with K=2 and K=3, and yellow triangles represent transitions with K=4. Linear fits to the points are shown for each group of K quantum numbers, to guide the eye. 69

3.5 Spectra of CH_3CCH observed toward G331. *Upper pannels*: J=10–9, ∼ 170.87–170.91 GHz; *Lower pannels*: J=18–17, ∼ 307.52–307.59 GHz. *Left pannels*: LTE models simulated for a compact emission (5″). *Right pannels*: LTE models simulated for an extended emission (10″). For all panels, the black and red spectra correspond to the observation and the LTE model, respectively. The dashed line indicates the systemic velocity of the source. The abscissas of all spectra were adjusted to the systemic velocity of the K=0 transition. 70

3.6 Observed spectra of the detected CH_3CCH lines (black), superimposed by the LTE models (red). The dashed line indicates the systemic velocity of the source. The abscissas of all spectra were adjusted to the systemic velocity of the K=0 transition. 71

3.7 Experimental (red, upper panel) and simulated (black, lower panel) pure rotational spectra of CH_3CCH at 300 K. The inset shows the J=10–9 K-ladder. 74

3.8 J=10_K–9_K K-ladder of CH_3CCH simulated at 10 K (upper-left panel), 40 K (upper-right panel), 70 K (lower-left panel) and 100 K (lower-right panel). 75

3.9 Intensity ratios I[K=n]/I[K=0] versus temperature for transitions within a given K-ladder. Purple squares represent ratios with $n = 1$, green circles represent ratios with $n = 2$, and red triangles represent ratios with $n = 3$. Solid and dashed lines correspond to, respectively, the J=10–9 and J=18–17 K-ladders. The red and blue regions are discussed in §3.3.4. 76

3.10 Superposition of the K=2 and K=3 lines of the J=10–9 (red) and K=18–17 (blue) K-ladders, evincing the intensity inversion of the peaks. The abscissa is adjusted to the systemic velocity of the K=2 lines. 77

3.11 Ratios of the areas for K=2 and K=3 lines versus the upper J value of the transition. Areas and uncertainties were obtained through gaussian fittings of the observed data using CLASS. 78

3.12 *Upper panel:* Modified rotational diagram of the CH_3CCH lines for a source size of 5″. Least squares fits with and without opacity corrections are shown in red and blue, respectively. *Lower panel:* Same as the upper panel, but assuming a source size of 10″. 79

3.13 rotational diagram of the CH_3CCH lines for a source size of 10″. The points were divided into two subsets indicated by the dashed line. The points pertaining to the low- and high-energy subsets are shown in blue and red, respectively. Least squares fits to the points within each subset are shown. Circles and squares correspond to the lines with and without opacity corrections, respectively. 80

3.14 Peak velocities versus line frequency obtained from gaussian fittings to the CH_3CCH lines. Each plot contains only transitions with the same K quantum number. 83

3.15 Line widths vs. rest frequencies obtained from gaussian fittings of the observed transitions. Each subplot contains only transitions with the same K quantum number 84

3.16 Line widths vs. peak velocities obtained from gaussian fittings of the observed transitions. Blue cross marks represent transitions with K=0, purple squares represent transitions with K=1, green circles represent transitions with K=2 and red triangles represent transitions with K=3. The black dashed line separates the blue- and red-shifted regions of the plot. G331 has a systemic velocity of -90 km s^{-1}. 86

3.17 *Top pannel:* Spectrum of G331 showing the 10_0–9_0 and 10_1–9_1 transitions of CH_3CCH in solid red line. Dashed green lines are the Gaussian profile fittings. The red dash-dot line indicates the peak velocity of the 10_0–9_0 transition. *Bottom pannel:* Same as the top pannel, but for the 18_0–17_0 and 18_1–17_1 transitions—in blue instead of red. 87

A.1 Spectral bands: ∼170630–171030 MHz; ∼187690–188130 MHz; ∼204750–205220 MHz 112
A.2 Spectral bands: ∼221800–222320 MHz; ∼238840–239430 MHz; ∼255920–256520 MHz 113
A.3 Spectral bands: ∼272970–273610 MHz; ∼290030–290710 MHz; ∼307080–307800 MHz 114

List of Tables

1.1 Generic gas-phase reactions and typical rate coefficients (Tielens, 2005; van Dishoeck, 2014). [a] Highly reaction specific. [b] In the exothermic direction. [c] In the unshielded radiation field. [d] In the exothermic direction and assuming no activation barrier. The rate coefficient units will depend on the rate expression and therefore on the order of the reaction. First-order and second-order reactions yield, respectively, k=[s^{-1}] and k=[cm^3s^{-1}]. 24

1.2 Elemental abundance with respect to total hydrogen in dark clouds. From the AL model in Acharyya and Herbst (2017). 28

2.1 Frequency channels of the SHeFI instrument. SIS stands for superconductor-insulator-superconductor mixer; SSB stands for single sideband receiver; HEB stands for hot electron bolometer mixer; and DSB stands for double sideband receiver. 55

2.2 Frequency channels of the SEPIA instrument. SIS stands for superconductor-insulator-superconductor mixer and 2SB stands for dual sideband receiver. 55

3.1 Spectral lines of CH_3CCH observed toward G331 and their parameters obtained from Gaussian fits. 65

3.2 Values of T_{exc} and N_{tot} of CH_3CCH toward G331 obtained from the analysis of the rotational diagrams. 68

3.3 Abundances of CH_3CCH observed toward high- and low-mass star-forming sites. [a] From Taniguchi et al. (2019). 72

3.4 Spectroscopic parameters employed in the spectrum simulations. The experimental measurements of the B rotational constant and the centrifugal distortion constants were obtained from Dubrulle et al. (1978). The dipole moment was measured by Muenter and Laurie (1966). Since the A rotational constant cannot be determined directly from the measured spectra, the estimated constant from the JPL database was used. 73

3.5 Values of χ^2_{red} obtained from the least square fits of the traditional and modified rotational diagrams. 79

3.6 Values of T$_{exc}$ and N$_{tot}$ of CH_3CCH obtained from the 2-component rotational diagrams for a source size of 10$''$. 81

Contents

1. Introduction 23

- 1.1 Interstellar chemistry 24
  - 1.1.1 Gas-phase processes 24
    - 1.1.1.1 Bond-formation processes 25
    - 1.1.1.2 Bond-destruction processes 26
    - 1.1.1.3 Bond-rearrangement processes 27
  - 1.1.2 Solid-phase processes 28
- 1.2 Massive star formation 29
  - 1.2.1 Core-accretion model 32
  - 1.2.2 Competitive-accretion model 33
  - 1.2.3 Protostellar-collision model 33
- 1.3 Hot Molecular Cores 34
  - 1.3.1 The HMC G331.512-0.103 36
- 1.4 Spectral lines' fundamentals 39
- 1.5 Rotational transitions 42
  - 1.5.1 The types of rotors 43
  - 1.5.2 The rotational Hamiltonian 45
  - 1.5.3 Dipole moment and selection rules 46
- 1.6 Rotational diagrams 46
  - 1.6.1 Opacity correction factor 48
  - 1.6.2 Beam dilution factor 49
- 1.7 The spectral tracer methyl acetylene 49

2. Facilities and methods 53

2.1 The Atacama Pathfinder EXperiment (APEX) 53

2.1.1 SHeFI 54

2.1.2 SEPIA 55

2.2 Observations and data calibration 56

2.3 Data reduction 57

2.4 Line identification and gaussian fitting 57

2.5 LTE analyses 58

2.5.1 Rotational diagrams 58

2.5.2 Synthetic LTE spectra 60

2.6 Rotational-spectrum simulations 61

3. Results and discussion 63

3.1 Line properties 63

3.2 LTE analyses 66

3.2.1 Rotational diagrams 66

3.2.2 Synthetic spectra 69

3.2.3 CH_3CCH abundance 71

3.3 Intensity inversion 73

3.3.1 Rotational-spectrum simulations 73

3.3.2 Inversion in the observed spectra 76

3.3.3 Modified rotational diagrams 78

3.3.4 Quantifying the temperature gradient 80

3.4 Kinematics 82

3.4.1 Velocity vs. frequency 82

3.4.2 FWHM vs. frequency 82

3.4.3 FWHM vs. velocity 85

4. Conclusions and future perspectives 89

4.1 Conclusions 89

4.2 Future perspectives 91

Bibliography 93

A. Total spectrum of G331 111

A.1 Here we present the total spectrum of G331, including the observations conducted with the SEPIA180, APEX-1 and APEX-2 receivers of the APEX 12 m telescope. 111

Chapter 1

Introduction

Since the beginning of written history, humanity has contemplated the question as to what is the origin of the stars, planets, and ultimately life. The Greek philosopher Thales of Miletus is believed to be the first individual in Western civilization to explore the formation of the universe from a naturalistic standpoint, earning him the *sobriquet* “the first philosopher”. According to his ideas, likely influenced by Mesopotamian beliefs, water would be the Primary Principle from which the cosmos and everything it encompasses come into being. Other presocratric thinkers, such as Leucippus and Democritus, also theorized on the elements that compose the natural world. They are regarded as the creators of the Atomist Doctrine, in which the world would be composed by two fundamentally different elements: atoms and void. The former are perfectly solid and indivisible bodies, which can only move about in the latter.

Later, during what the French philosopher Auguste Comte described as the third stage of human society, the combination of rational thinking and observation resulted in more solid theories to describe the origin of the stellar bodies. His epistemological arguments were preceded by the ideas of notable characters such as Galileo Galilei, Isaac Newton, Francis Bacon and René Descartes, who heavily contributed to the consolidation of the scientific method. Now, over 200 years after the beginning of Comte’s so-called “positive stage”, modern science has developed an impressive amount of facilities and techniques to explore thoroughly those fundamental questions. In this context, this master’s thesis aims to contribute ever so slightly to our understanding of massive star formation processes, and its entanglement with the chemistry of the Interstellar Medium (ISM).

1.1 Interstellar chemistry

To date, nearly 200 individual molecules, comprising 16 different elements, have been definitively detected in the interstellar and circumstellar media[1]. Those species, which are majorly organic, have also had numerous isotopologue detections. The chemical processes that occur in those environments and result in the formation of molecular species can be divided into two broad classes: reactions that take place on the surface of interstellar grains and reactions that occur in the gas phase. In the following sections, we provide a brief overview of those processes.

1.1.1 Gas-phase processes

Gas-phase reactions can be further separated into three different categories: bond-formation processes, bond-destruction processes, and bond-rearrangement processes. In Table 1.1, we summarize the generic examples of those processes and their typical reaction rate coefficients.

Table 1.1 - Generic gas-phase reactions and typical rate coefficients (Tielens, 2005; van Dishoeck, 2014). [a] Highly reaction specific. [b] In the exothermic direction. [c] In the unshielded radiation field. [d] In the exothermic direction and assuming no activation barrier. The rate coefficient units will depend on the rate expression and therefore on the order of the reaction. First-order and second-order reactions yield, respectively, k=[s^{-1}] and k=[cm^3s^{-1}].

	Reaction	Rate coefficient
Bond-formation processes		
Radiative association	$X + Y \rightarrow XY + h\nu$	10^{-17} to 10^{-14} cm^3s^{-1} [a]
Associative detachment	$X^- + Y \rightarrow XY + e$	$\sim 10^{-9}$ cm^3s^{-1} [b]
Bond-destruction processes		
Photodissociation	$XY + h\nu \rightarrow X + Y$	10^{-10} to 10^{-8} s^{-1} [c]
Dissociative recombination	$XY^+ + e \rightarrow X + Y$	10^{-7} to 10^{-6} cm^3s^{-1}
Bond-rearrangement processes		
Ion-molecule exchange	$X^+ + YZ \rightarrow XY^+ + Z$	10^{-9} to 10^{-8} cm^3s^{-1} [b]
Charge-transfer	$X^+ + YZ \rightarrow X + YZ^+$	10^{-9} cm^3s^{-1} [b]
Neutral-neutral	$X + YZ \rightarrow XY + Z$	10^{-11} to 10^{-9} cm^3s^{-1} [d]

For unimolecular reactions, the rates of formation or destruction of a species are given by:

---

[1] see `https://cdms.astro.uni-koeln.de/`

$$\frac{dn(A)}{dt} = -kn(A) = -\frac{dn(C)}{dt} \tag{1.1}$$

Where k is the reaction rate coefficient in s^{-1} and n is the concentration in cm^{-3}. Analogously, for bimolecular reactions:

$$\frac{dn(A)}{dt} = -kn(A)n(B) = -\frac{dn(C)}{dt} \tag{1.2}$$

Where k is the reaction rate coefficient in $cm^3\ s^{-1}$. Chemical processes that involve three or more bodies are only significant for densities above 10^{13} cm^{-3} (van Dishoeck, 2014), which is far too high for the regions explored in this work. In the following subsections, we give a panoptic view of the main chemical processes that occur in the gas-phase of the ISM.

1.1.1.1 Bond-formation processes

In radiative association reactions, the binding energy of the newly formed molecule is carried away through the emission of radiation, which stabilizes the collision product. With the exception of large molecules (e.g., Polycyclic Aromatic Hydrocarbons (PAHs)) or tightly bound species, those processes are typically very slow, and therefore are highly inefficient (van Dishoeck, 2014).

In a scenario where the reagent species form a long-lived activated complex before the emission of a photon and stabilization of the final product, the radiative-association process becomes more likely to happen. In this case, the reaction can be represented by:

$$X + Y \underset{k_d}{\overset{k_a}{\rightleftharpoons}} XY^* \xrightarrow{k_r} XY \tag{1.3}$$

where k_a, k_d, and k_r are the association, dissociation, and radiative stabilization rates, respectively. X and Y are the reactants and XY^* is the activated complex. This complex temporarily stores the kinetic energy and interaction energy as vibrational energy, which is eventually released through a vibrational transition accompanied by the emission of a photon. The radiative rate of those transitions is $\sim 10^{-3}$ s^{-1}, which is usually much slower that collision timescales. For this reason, laboratory measurements of those rate coefficients are generally not feasible, and estimations are obtained through theoretical calculations.

In associative-detachment reactions, the neutral product of the collision of an anion and an atom is stabilized by the emission of an electron. In general, reactions involving anions as reactants do not contribute significantly to the chemistry of the ISM (the formation of negative ions being the limiting step), although there is one notable exception. The reaction

$$H + H^- \rightarrow H_2 + e \tag{1.4}$$

has a rate coefficient of $k = 1.3 \times 10^{-9}$ cm^3 s^{-1}, and potentially played an important role in the formation of H_2 in the early Universe (Tielens, 2005).

1.1.1.2 *Bond-destruction processes*

The UV radiation that permeates diffuse interstellar clouds leads to the destruction of molecular bonds through photodissociation (Millar and Williams, 1988). While typical bonding energies of molecules are below 10 eV, direct absorption into the dissociating continuum state induced by UV radiation is generally not an important effect. Instead, photodissociation more commonly occurs following one of the three routes: through a transition to the continuum of an electronically excited state, through the mixture of the excited electronic state with a dissociative state, or through the radiative decay of an excited electronic state to the continuum of the ground electronic state. In diffuse clouds, where there is an intense UV radiation flux, typical molecular lifetimes are of only ∼100–1000 years (van Dishoeck, 2014).

Upon penetrating interstellar clouds, the UV radiation is attenuated due to dust absorption and scattering effects. For this reason, the radiation field will depend on the opacity into the cloud. UV absorption by abundant species can also impact the penetration capability of the radiation and therefore the photodissociation rates. Those reactions are induced by absorption lines, which can in turn become optically thick. In this scenario, the molecular species lying deeper into the cloud are shielded from the radiation by the so-called "self-shielding"effect (van Dishoeck and Black, 1988). This phenomenon is particularly important for species such as H_2 (Abgrall et al., 2000), CO (Visser et al., 2009), and N_2 (Li et al., 2013; Heays et al., 2014).

Besides the external radiation field, UV photons can also be produced inside the cloud. Primary electrons generated by cosmic rays can electronically excite H_2 molecules, which decay radiatively and release UV photons. Since cosmic rays are energetic enough to penetrate deep into the clouds, this mechanism result in a constant UV flux even at long depths.

Another bond-destruction process, dissociative recombination, involves the capture of an electron by a molecular ion, which forms a neutral species in an excited electronic state that can eventually dissociate. This process is usually very quick at low temperatures, thus efficiently destroying molecular ions.

1.1.1.3 Bond-rearrangement processes

Besides forming and destructing molecular bonds, chemical reactions can also lead to the formation of more complex species by means of bond-rearrangement processes. In the case of exothermic ion-molecule exchange, energy barriers can be easily overcome by their strong polarization-induced interaction potential, thus resulting in generally high rate coefficients. That is to say, ion-molecule reactions are usually very fast, and because of that they play an important role in the chemistry of the ISM. In general, those processes are driven either by cosmic ray ionization or photoionization, and their rate coefficients are independent of temperature. Reactions involving ions and molecules with permanent electric dipole moments (e.g., $C^+ + H_2O \rightarrow H + HOC^+$) have even larger rate coefficients, due to their enhanced long-range attraction. Furthermore, charge exchange reactions involving atoms are particularly important to the ionization balance of the environment, as is the case for O and H^+ in HII regions (Tielens, 2005).

Contrarily to ion-molecule reactions, neutral-neutral reactions usually involve considerable activation barriers, as a consequence of the bond-breaking associated with the molecular rearrangement. Since their attractive interaction due to van-der-Waals forces is weak, activation barriers can significantly hinder those processes. For this reason, neutral-neutral reactions are generally important only for warm gas—such as in stellar ejecta or hot cores (Tielens, 2005).

Naturally, the importance of each reaction route in forming a particular species will depend on the elemental abundances, the enthalpy of the reaction (i.e., if it's endothermic or exothermic), and whether or not there is an activation barrier. Thus, exothermic reactions involving H and H_2 usually dominate interstellar chemical networks. In Table 1.2, typical low-metal elemental abundances used for modeling the chemistry of dark clouds are listed.

Table 1.2 - Elemental abundance with respect to total hydrogen in dark clouds. From the AL model in Acharyya and Herbst (2017).

Element	Abundance	Element	Abundance
H_2	0.5	S^+	8×10^{-8}
He	0.09	Fe^+	3×10^{-9}
C^+	7.3×10^{-5}	Na^+	2×10^{-9}
N	2.14×10^{-5}	Mg^+	7×10^{-9}
O	1.76×10^{-4}	Cl^+	1×10^{-7}
F	1.8×10^{-8}	P^+	2×10^{-10}
Si^+	8×10^{-9}		

1.1.2 Solid-phase processes

The interstellar solid-phase chemistry happens in the surface of dust particles that are shrouded by ice mantles. Those bodies have a layered structure consisting of a carbonaceous core, followed by a layer of water-rich ice and a layer of water-poor ice (see Figure 1.1). This stratified shape is due to the condensation of the ice: at the earlier evolutionary stages of the cloud, hydrogenation of atomic oxygen forms the water-rich layer; then, the freeze-out of CO leads to the formation of the CO-rich and water-poor layer (van Dishoeck, 2014). Those icy surfaces act as catalysts (Tielens, 2005), facilitating the formation of many different molecular species even without any energy input (e.g., see Linnartz et al. 2015; Qasim et al. 2020).

The three major mechanisms whereby grain-surface chemistry occurs are the Langmuir-Hinshelwood, the Eley-Rideal, and the Harris-Kasemo—also known as hot atom. In the first one, also called the diffusive mechanism, the accreted reactants first reach thermal equilibrium with the surface, and then one or both diffuse through the biding sites of the ice until reaching one-another and reacting. In the Eley-Rideal mechanism, the gas-phase species does not diffuse, but rather lands on top of another species and promptly reacts, without reaching thermal equilibrium beforehand. Finally, in the hot-atom mechanism, the accreted reactant diffuses through the ice and reacts with another adsorbed species before reaching thermal equilibrium (Herbst and van Dishoeck, 2009; Linnartz et al., 2015). In Figure 1.2, we present a schematic view of these three processes.

While grain-surface reactions indeed contribute significantly to the chemical inventory of the ISM, solid-phase species lack rotational degrees of freedom and therefore are not

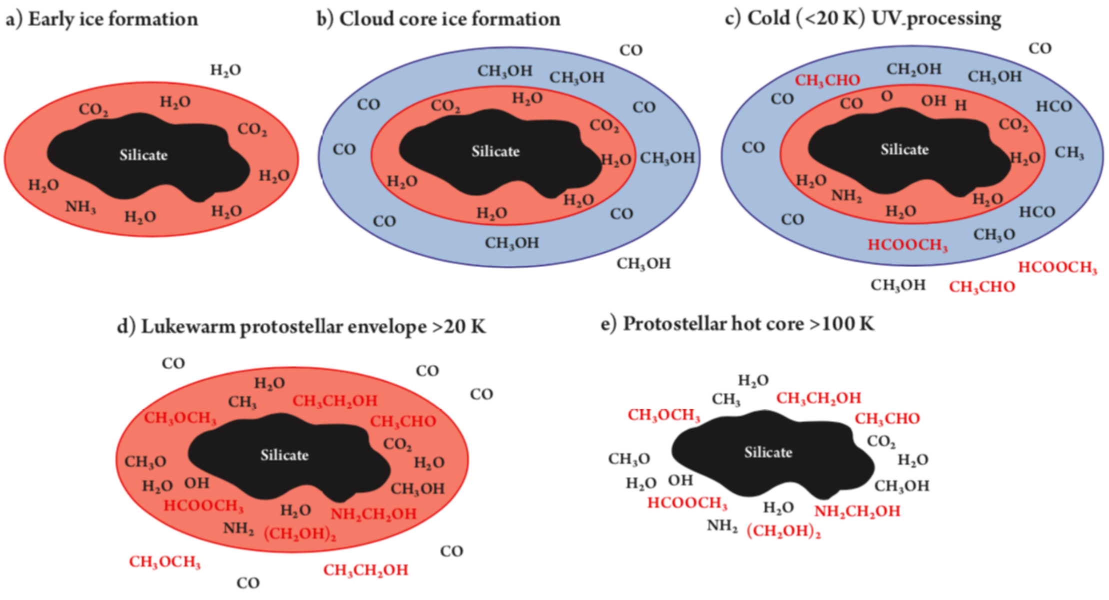
a) Early ice formation
Silicate
H_2O
CO_2
NH_3
b) Cloud core ice formation
Silicate
CO
CH_3OH
H_2O
CO_2
c) Cold (<20 K) UV processing
Silicate
CO
CH_3OH
CH_3CHO
O
OH
H
HCO
CH_3
CH_3O
$HCOOCH_3$
H_2O
CO_2
NH_3
d) Lukewarm protostellar envelope >20 K
Silicate
CO
H_2O
CH_3
CH_3CH_2OH
CH_3OCH_3
CH_3CHO
CO_2
CH_3O
OH
CH_3OH
$HCOOCH_3$
NH_2CH_2OH
NH_2
$(CH_2OH)_2$
e) Protostellar hot core >100 K
Silicate
H_2O
CH_3
CH_3CH_2OH
CH_3OCH_3
CH_3CHO
CO_2
CH_3O
OH
CH_3OH
$HCOOCH_3$
NH_2CH_2OH
NH_2
$(CH_2OH)_2$

Figure 1.1: From van Dishoeck (2014). Formation and evolution of the interstellar ices. The H_2O-rich ice is shown in red, while the CO-rich ice is shown in blue.

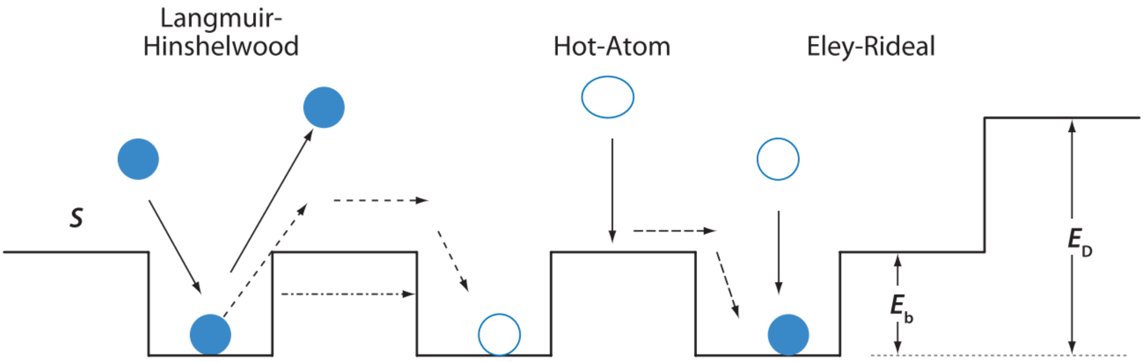
Langmuir-Hinshelwood
Hot-Atom
Eley-Rideal
S
E_D
E_b

Figure 1.2: Sketch of the three major surface reaction mechanisms. From Herbst and van Dishoeck (2009).

typically observable with radio telescopes. For this reason, the present work focuses on gas-phase processes. The reader is referred to specialized literature (e.g., Williams and Cecchi-Pestellini 2016 and the references cited in this subsection) for more in-depth discussions on interstellar solid-phase chemistry.

1.2 *Massive star formation*

Massive stars, as the name suggests, are characterized by gargantuan masses ($M > 8M_\odot$) and luminosities ($L > 10^3 L_\odot$). Through turbulence-enhancing phenomena, such as massive outflows and expanding HII regions, they greatly affect the energy budget of the galaxies. Moreover, they are the main sources of heavy-element and UV-radiation injection into the ISM. Thus, massive stars play a crucial role in shaping galactic structure and evolution.

They are born within cloud corpuscles of ∼1–10 pc and ∼10–10^6 $M_\odot$, known as massive clumps, which in turn are predominantly observed in hyper-massive and hyper-dense molecular clouds (Tan, 2018). The formation process of those stars, however, is still poorly understood. While, for low-mass stars, there is a solid and well-established evolutionary sequence (see Shu et al. 1987; Andre et al. 2000), many open questions still remain for the massive counterparts. The difficulty associated with the study of massive star formation is mostly due to their substantially shorter evolutionary timescale ($t_{KH} \leq 10^4$ yr for O-type stars), combined with observational constrains, such as their complex cluster environments ($n_\star \gtrsim 100pc^{-3}$) and large distances involved ($d \geq 1kpc$) (Garay and Lizano, 1999; Zinnecker and Yorke, 2007; Silva et al., 2017). Inasmuch as the observational study of those environments continues to be hampered by their scarcity and other intrinsic limitations, theoretical models that incorporate astrochemistry are key to successfully work toward building a massive star formation paradigm (see Tan 2018).

Massive gas clumps are defined following Tan et al. (2014) and Tan (2018), in which they are self-gravitating structures that fragment into massive star clusters. According to the core-accretion model of massive star formation (see §1.2.1), this fragmentation occurs through the formation of dense, self-gravitating cores, which in turn collapse to form either single or multiple stars. A schematic view of the different levels of fragmentation involved in the formation of massive stars is shown in Figure 1.3, from Sadaghiani et al. (2020).

In the first hierarchical level, there is the example molecular cloud NGC 6334, which has an elongated filamentary structure. This filament is fragmented into clumps with masses of a few hundred $M_\odot$. The clumps are in turn fragmented into cores, within which the stars are formed. Furthermore, observations and numerical models indicate that some of these cores can be further fragmented to form bound clusters, at scales between 500–5000 au (Offner et al., 2010; Hunter et al., 2014; Brogan et al., 2016; Sadaghiani et al., 2020). In the following subsections, we briefly outline the main formation scenarios of massive stars embedded in those structures.

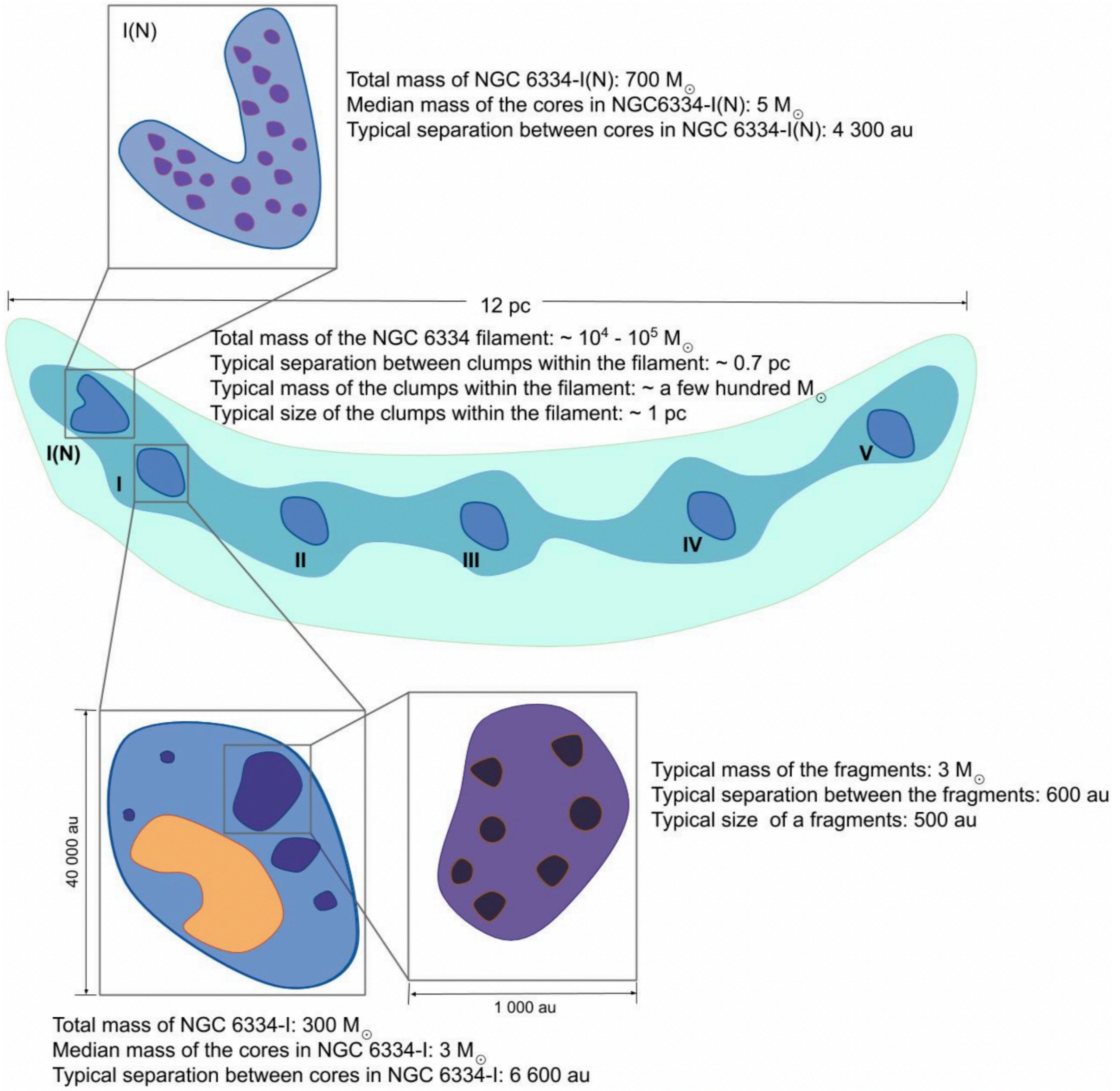
I(N)
Total mass of NGC 6334-I(N): 700 M⊙
Median mass of the cores in NGC6334-I(N): 5 M⊙
Typical separation between cores in NGC 6334-I(N): 4 300 au
12 pc
Total mass of the NGC 6334 filament: ~ 10⁴ - 10⁵ M⊙
Typical separation between clumps within the filament: ~ 0.7 pc
Typical mass of the clumps within the filament: ~ a few hundred M⊙
Typical size of the clumps within the filament: ~ 1 pc
I(N)
I
II
III
IV
V
40 000 au
Typical mass of the fragments: 3 M⊙
Typical separation between the fragments: 600 au
Typical size of a fragments: 500 au
1 000 au
Total mass of NGC 6334-I: 300 M⊙
Median mass of the cores in NGC 6334-I: 3 M⊙
Typical separation between cores in NGC 6334-I: 6 600 au

Figure 1.3: Figure from Sadaghiani et al. (2020), showing the different fragmentation levels of the NGC 6334 star-forming complex from the scale of the filament down to the scale of individual dense cores and protostars. The colors indicate different densities—lighter colors correspond to lower densities, whereas darker colors indicate higher densities—as well as ionized gas (in orange). Vertical and horizontal orientations correspond to the Galactic latitude and longitude coordinates, respectively. The distribution is based on observations by Russeil et al. (2013).

1.2.1 Core-accretion model

The core-accretion model is the most conservative and simplest approach to massive star formation. It treats those processes as simply scaled-up versions of low-mass star formation theories, in which gas accretion occurs when gravity overcomes the thermal pressure gradient (Shu et al., 1987; Lada and Kylafis, 1999). In this theory, the final mass of the star is related to the mass of the core from which it forms. Thus, it predicts that the initial mass function is determined by the core mass function.

For a single, isothermal sphere, the low-mass accretion rate follows (Shu, 1977):

$$\dot{m}_* = 0.975\frac{c_{th}^3}{G} = 4.36 \times 10^{-6}\left(\frac{T}{20\ K}\right)^{3/2} M_\odot\ yr^{-1} \tag{1.5}$$

where c_{th}^3 corresponds to the isothermal sound speed and assuming $n_{He} = 0.2\ n_{H_2}$. However, some difficulties arise when we expand this theory to high-mass stars. Since the predicted accretion rate is a function of only the gas temperature, and since they are positively correlated, the first massive stars that form in a region (that is, from a gas with T∼10–20 K) will have low accretion rates and thus will take too long to form. To address this issue, McKee and Tan (2003) propose the so-called Turbulent Core Model (TCM), in which the internal supersonically turbulent motions observed in the cores induce internal substructures that then lead to an increase in the accretion rate with time (Myers and Fuller, 1992; Caselli and Myers, 1995; McLaughlin and Pudritz, 1997). This model is based on the fact that Equation 1.5 holds approximately when the non-thermal effects of turbulence and magnetic fields are incorporated (Stahler et al., 1980; Shu et al., 1987). Therefore, the pressure support of the massive cores is provided by turbulence and/or magnetic fields. As a result, the free-fall timescale of the dense cores will be shortened, and the accretion rates will be higher, once they become unstable and collapse.

One of the challenges of the core accretion model is related to the fact that the dense cores have many Jeans masses[2] for a temperature of ∼10 K (Tan et al., 2014). Thus, instead of forming a single massive star, it should fragment further into forming a cluster of low-mass stars. This problem is addressed by McKee and Tan (2003), in which they assume that most of the density fluctuations in a core at a given moment are gravitationally stable. Furthermore, Krumholz (2006) suggested that the radiative feedback from the first stars would heat up the surrounding gas in the core and thus suppress the fragmentation. This was later confirmed by a number of simulations (see Krumholz and Bonnell 2007; Krumholz et al. 2010, 2011).

---

[2] The Jeans mass corresponds to the mass threshold above which the cloud undergoes gravitational collapse.

1.2.2 Competitive-accretion model

In the competitive-accretion model (Bonnell et al., 2001; Wang et al., 2010), the massive clumps fragment into protostellar seeds with initial masses of the order of the thermal Jeans mass. Then, they later accrete the surrounding gas, eventually forming massive stars. Unlike the core-accretion model, in this theory the gas is initially not gravitationally bound to the star. Instead, it is drawn chaotically from a wider region of the clump. In other words, the protostellar seeds are formed through gravitational collapse, but then grow by tidally-modified Bondi-Hoyle[3] accretion, competing for the mass available in the clump.

The environment where those seeds are formed is highly dense and clustered. The number of stellar objects directly affects the mass accretion rates of the cluster members, thus signaling a causal relationship between the formation processes of clusters and massive stars. As a consequence of this model, massive stars should be segregated toward the center of the cluster, where the global clump infall leads to high gas densities.

This model also presents intrinsic difficulties that have yet to be solved. One of them is related to the radiation pressure feedback of the star, which disrupts the Bondi-Hoyle accretion for stellar masses above $\sim$10 $M_\odot$ (Edgar, 2004). As a result, the competitive accretion should not operate for stellar masses above this threshold. Moreover, this model also does not account for turbulent (virialized) media, in which the accretion rate would be too small to allow formations within timescales $\lesssim$1 Myr (Krumholz et al., 2005).

1.2.3 Protostellar-collision model

In the protostellar-collision model, high-mass stars are proposed to be formed via direct collisions of lower-mass protostars (Bonnell et al., 1998; McKee and Tan, 2003). Because they are optically thick, merging protostars are not affected by stellar feedback, thereby overcoming the problem of radiation pressure halting massive star formation. This model also yields high accretion rates—and, consequently, short formation timescales. However, in order to account for the stellar evolution timescale, those collisions should take place during a brief period in which the protostellar and stellar densities of a forming massive cluster must reach notably high values of $\sim 10^8$ stars pc^{-3} (e.g., Bonnell et al. 1998; Bonnell and Bate 2002). Such a hypothesized ultradense region should presumably be very luminous, and yet has never been observed. Thus, this model is unlikely to play an important role in typical massive star-forming regions.

---

[3] Bondi-Hoyle accretion is a spherical accretion onto a compact object moving through a uniform gas free of self-gravity. For more information, see Edgar (2004) and references therein.

1.3 Hot Molecular Cores

Despite the lack of a thoroughly defined evolutionary sequence, some precursors of high-mass stars are well established. One example are Hot Molecular Cores (HMCs), which are believed to be one of the first observable stages of massive star formation (Osorio et al., 1999). HMCs are characterized by compact sizes ($\lesssim$ 0.1 pc), relatively high temperatures ($\gtrsim$ 100 K) and high densities ($n_{H_2} \sim 10^5 - 10^8$ cm^{-3}), as well as large luminosities ($> 10^4$ L$_\odot$) and masses ($\sim$ 10 − 1000 M$_\odot$) (Heaton et al., 1989; Gomez et al., 1995; Cesaroni et al., 1998). They are associated with a rich molecular emission spectrum, including high-excitation transitions of multifarious "exotic" molecules (e.g., Comito et al. 2005), as well as H_2O masers, and, oftentimes, ultracompact (UC) HII regions (Cesaroni, 2005). The HMC phase is thought to last from $\sim 10^5$ yr (van Dishoeck and Black, 1988) to $\sim 10^6$ yr (Garrod and Herbst, 2006). Comparatively, smaller regions ($\lesssim$100 au) with similar characteristics are observed around solar-type protostars. Those low-mass counterparts are designated "hot-corinos"(Cazaux et al., 2003; Bottinelli et al., 2004; Ceccarelli, 2005).

HMCs are embedded in more extended molecular clumps, typically 10 times larger and more massive than the cores themselves (Cesaroni et al., 1991; Plume et al., 1997; Hofner et al., 2000). The temperature and density profiles of those clumps vary as:

$$\begin{aligned} n &\propto R^{-p} \\ T &\propto R^{-q} \end{aligned} \tag{1.6}$$

where R is the distance from the core. Generally, $p \simeq 1.5 - 2.5$ and $q \simeq 0.5$ (Hatchell et al., 2000; Fontani et al., 2002). In Figure 1.4, an image of a HMC observed toward IRAS

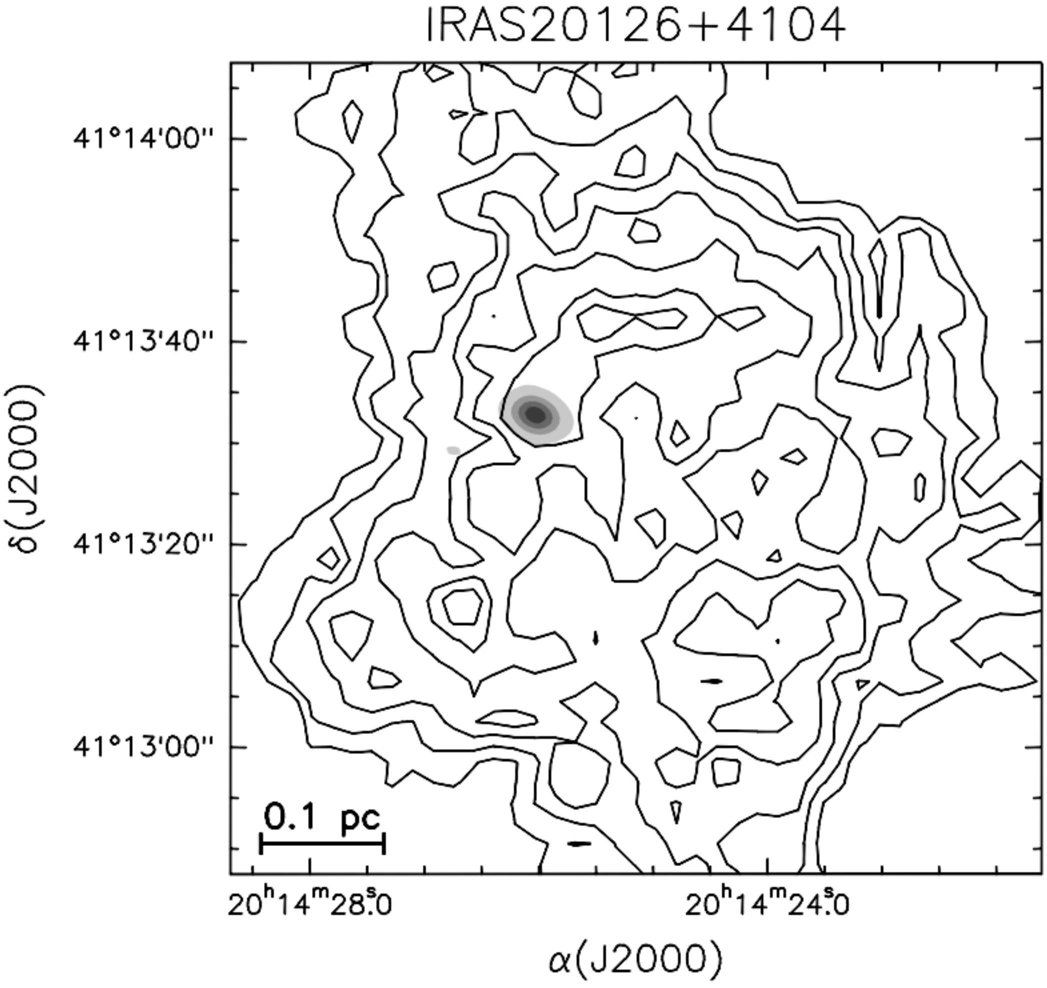

Figure 1.4: Superimposed maps of the CH_3CN(5–4) traced HMC in the high-mass star-forming region IRAS 20126+4104 (grey scale) and the $C^{17}O$(2–1) traced surrounding molecular clump (contours). From Cesaroni 2005.

20126+4104 in the CH_3CN(5–4) line is shown in combination with a $C^{17}O$(2–1) map of the surrounding molecular clump (Cesaroni, 2005).

The velocities associated with HMCs are virtually indistinguishable from those of the corresponding clumps. Moreover, Fontani et al. (2002) have shown that the density profile of the clump agrees with the mean density of the embedded HMC. Thus, the distinction between HMCs and their surrounding clump (i.e., the HMC diameter) can be blurry. Indeed, a more accurate description would be that HMCs correspond to a particular region inside the clump where density and temperature peak, as a result of the Massive Young Stellar Objects (MYSOs) embedded in them. This hypothesis is supported by the high masses and luminosities associated with HMCs, as well as the recurrent observations of H_2O masers and UC HII regions toward those sources. Hence, HMCs could be further perceived as the very sites where collapse presumably takes place and fragmentation leads to star formation (see Cesaroni 2005).

The presence of powerful molecular outflows in many observed HMCs (e.g., Cesaroni et al. 1997, 1998; Gibb et al. 2004; Zhang et al. 2007; Bronfman et al. 2008; Qiu et al. 2008) also agrees with this scenario, in which it is speculated that the outflows determine the last stages of the HMC phase and the subsequent development of UC HII regions (Cesaroni, 2005). Outflows provide optically thin channels through which the radiation can escape, thus reducing the radiation pressure barrier on the infalling gas and enabling the accretion onto the protostar (see, e.g., Kuiper and Yorke 2013). The resulting intense mass-accretion rates quench the development of an HII region around the massive star (Walmsley et al., 1995; Keto, 2002, 2003). The fact that free-free emission is not usually detected in those sources supports the hypothesis that HMCs precede UC HII regions.

1.3.1 The HMC G331.512-0.103

The radio source G331.5-0.1 is located at the tangent point of the Norma spiral arm, in the Southern Galaxy, at a distance of ∼7.5 kpc (Bronfman et al., 1989, 2008). It consists of an extended, exceptionally luminous, and massive region of ionized gas at the center of a Giant Molecular Cloud (GMC) with a FIR luminosity of 3.6×10^6 $L_\odot$ and with a total CO mass of 8.7×10^6 $M_\odot$ (Bronfman et al., 2008; Merello et al., 2013a). Hydrogen recombination lines yield a systemic velocity of -89 km s^{-1} for this source (Caswell and Haynes, 1987). Moreover, as evinced by its high luminosity and intense maser emission of OH and CH_3OH (Nyman et al., 2001; Bronfman et al., 2008; Mendoza et al., 2018), as well as its various observed UC HII regions (Bronfman et al., 2000), this cloud harbors active sites of massive star formation.

The radial distribution of massive star forming regions in the Galactic disk is correlated with the azimuthally averaged radial distribution of the molecular gas—also known as the "molecular ring"—for all galactocentric radii. In the southern Galaxy, both molecular and massive-star-formation-rate rings peak within the range $0.5 \leq R/R_\odot \leq 0.6$ (Bronfman et al., 2000), in a region that coincides with the location of the parent GMC (García et al., 2014). Indeed, this GMC consists of one of the most massive and active star forming clouds in the southern Galaxy. Likewise, the Norma spiral arm seems to be one of the most active spiral features in forming massive stars. García et al. (2014) have derived a massive star formation rate per unit H_2 mass (MSFR) of 0.58 ± 0.09 $L_\odot/M_\odot$ for the most massive clouds in the Norma arm. Comparatively, the average MSFR for their entire sample of GMCs was of 0.41 ± 0.06 $L_\odot/M_\odot$. Conceivably, the MSFR of the most massive GMCs within the Norma arm, including G331.5-0.1, could even be used as a standard scale to compare the massive star formation activity in the rest of the Galaxy (as suggested by García et al. 2014).

Dust continuum observations at 1.2 mm have revealed six massive dust concentrations spread along the source, with a total mass of $\sim 1.4 \times 10^4$ $M_\odot$ (Nyman et al., 2001). Within the brightest of them, Bronfman et al. (2008) observed a massive and powerful molecular outflow—namely, G331.512-0.103—by means of line emission maps of the entire G331.5-0.1 core in the CS(7–6), ^{13}CO(3–2), CO(3–2), CO(4–3), and CO(7–6) transitions. The molecular outflow/HMC G331.512-0.103 (henceforth G331) is one of the most distinctive HMCs known to date. It is associated with a very rich emission spectrum, including simple hydrocarbons, radical species, and a plethora of complex organic molecules (Merello et al., 2013a,b; Mendoza et al., 2018; Duronea et al., 2019; Hervías-Caimapo et al., 2019). Observational evidence indicates that a MYSO at the center of G331 drives a powerful outflow with $\sim$55 $M_\odot$ of mass and a momentum of $\sim 2.4 \times 10^3$ $M_\odot$ km s^{-1}, with lobes closely aligned with the line of sight. The shock of the outflow against the surrounding dense gas produces UV photons that, combined with the protostellar radiation, result in free-free emission that is observed in the radio continuum (Bronfman et al., 2008; Merello et al., 2013b). Moreover, observations with the Atacama Large Millimeter/submillimeter Array (ALMA) of the SiO(8-7), $H^{13}CO^+$(4-3), HCO^+(4-3), and CO(3-2) transitions revealed an expanding shocked shell driven by stellar winds, which probably arises from the protostar confined in a hyper-compact HII region of $\sim$5 arcsec (projected size of $\sim$0.2 pc). Those observations lead to an estimated source age of $\sim$2000 yr, making G331 one of the youngest hot cores/molecular outflows known to date (Merello et al., 2013b). In Figure 1.5, from Hervías-Caimapo et al. (2019), integrated emission maps of G331 in multiple transitions are shown, together with the 862 μm continuum emission map.

As shown in Figure 1.5, Hervías-Caimapo et al. (2019) have conducted ALMA observations of various molecular transitions toward G331. They concluded that the observed molecular lines could be divided into two groups based on their widths: one that presents narrow lines that trace the core ambient gas (e.g., CH_3OH, CH_3CCH, $H^{13}CO^+$), and one

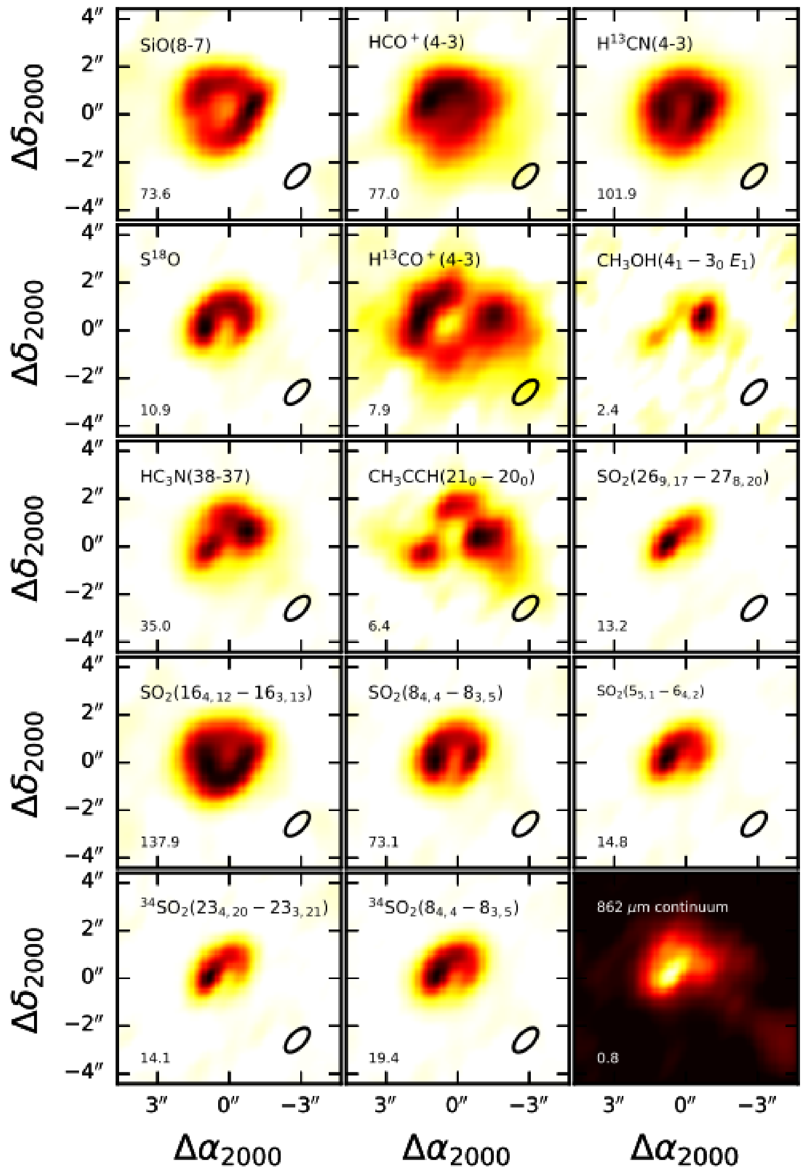

Figure 1.5: Zeroth moment maps of emission from G331, integrated in the range of the systemic velocity. The 862 μm continuum emission map is also shown (bottom right panel). From Hervías-Caimapo et al. (2019).

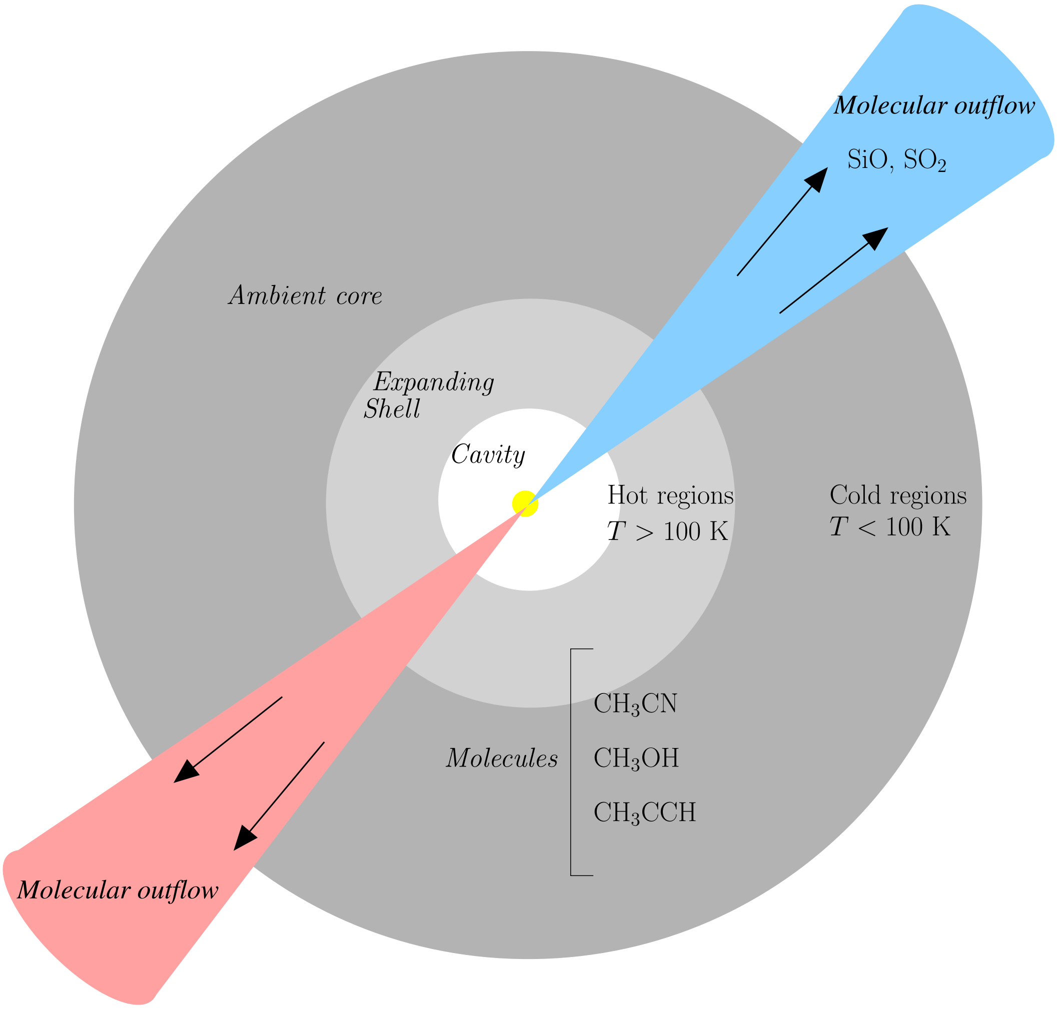
Molecular outflow
SiO, SO$_2$
Ambient core
Expanding Shell
Cavity
Hot regions
$T > 100$ K
Cold regions
$T < 100$ K
Molecules
CH$_3$CN
CH$_3$OH
CH$_3$CCH
Molecular outflow

Figure 1.6: Schematic view of the physical model proposed for G331. Based on the models of Merello et al. (2013a); Duronea et al. (2019); Hervías-Caimapo et al. (2019)

that presents broader lines that trace the high-velocity outflow (e.g., HC$_3$N, SiO, S^{18}O, HCO$^+$, H^{13}CN). Thus, different molecules will give information on different morphological features of this source. The ambient core is characterized by lower temperatures (T$_K$ ∼70 K), whereas the outflow yields higher values (T$_K$ ∼150–200 K). Duronea et al. (2019) further speculate that the HC$_3$N emission originates from an intermediate region between the ambient core and the expanding shell, based on the rotational temperatures they obtained. A schematic view of the physical model of G331 is presented in Figure 1.6.

1.4 Spectral lines' fundamentals

The interaction of a ray of electromagnetic radiation with matter can result in the addition or subtraction of energy from the ray by either emission or absorption. The energy emitted by the matter will result in an intensity addition to the beam (Rybicki and Lightman, 1985):

$$dI_\nu = j_\nu ds \tag{1.7}$$

where j_ν is the monochromatic emission coefficient and ds is the distance traveled by the beam. Conversely, the loss of intensity in a beam due to absorption by the matter is described by:

$$dI_\nu = -\alpha_\nu I_\nu ds \tag{1.8}$$

where α_ν is the absorption coefficient, defined as $\alpha_\nu = n\sigma_\nu$, to wit: the product of the density n of the absorbing particles times their absorption cross section σ_ν. Since both "true" absorption and stimulated emission are proportional to the intensity of the incoming beam, both phenomena are considered as "absorption" in Equation 1.8.

The combined effects of emission and absorption result in an expression for the variation of specific intensity along a ray (Rybicki and Lightman, 1985):

$$\frac{dI_\nu}{ds} = -\alpha_\nu I_\nu + j_\nu \tag{1.9}$$

Equation 1.9 is know as the Radiative Transfer Equation. In the limiting cases of either no absorption or no emission, its solutions are:

- Emission only: In this case, $\alpha_\nu = 0$ and $\frac{dI_\nu}{ds} = j_\nu$. This expression has the solution:

$$I_\nu(s) = I_\nu(s_0) + \int_{s_0}^{s} j_\nu(s')ds' \tag{1.10}$$

- Absorption only: In this case, $j_\nu = 0$, and $\frac{dI_\nu}{ds} = -\alpha_\nu I_\nu$. This expression has the solution:

$$I_\nu(s) = I_\nu(s_0) + \exp\left[-\int_{s_0}^{s} \alpha_\nu(s')ds'\right] \tag{1.11}$$

When the medium is under Thermodynamic Equilibrium, the radiation is in complete equilibrium with its surroundings, and the brightness distribution can be described by the Planck function:

$$\frac{dI_\nu}{ds} = 0 \tag{1.12}$$

$$I_\nu = \frac{j_\nu}{\alpha_\nu} = B_\nu(T) = \frac{2h\nu^3}{c^2}\frac{1}{e^{h\nu/kT} - 1} \tag{1.13}$$

The concepts hitherto presented apply for both continuous and line radiation. However, since this thesis revolves around molecular lines, we will henceforth focus the discussion on the latter. The expression $j_\nu = \alpha_\nu B_\nu$ (Equation 1.13), also know as Kirchhoff's law, implies the existence of a relationship between emission and absorption at a microscopic level. This relationship is described by the Einstein coefficients, which represent the probability of a system to make a transition from one energy level to another either by absorbing or emitting a photon. The Einstein coefficients are associated with three different processes (Rybicki and Lightman, 1985):

- Spontaneous emission: This process occurs when the system drops from a level with higher energy to a level with lower energy, resulting in the emission of a photon. It occurs even in the absence of a radiation field. It is described by the Einstein A coefficient:

  $$A_{ji} = \text{transition probability per unit time for spontaneous emission} \tag{1.14}$$

- Absorption: The system makes a transition from a lower-energy level to a higher-energy level by absorbing a photon. The probability for this process is proportional to the density of photons:

  $$B_{ij}\bar{J} = \text{transition probability per unit time for absorption} \tag{1.15}$$

  where the Einstein B coefficient is the proportionality constant.

- Stimulated emission: This process is also proportional to $\bar{J}$, but causes the emission of a photon. Thus, we have another Einstein B coefficient:

  $$B_{ji}\bar{J} = \text{transition probability per unit time for stimulated emission} \tag{1.16}$$

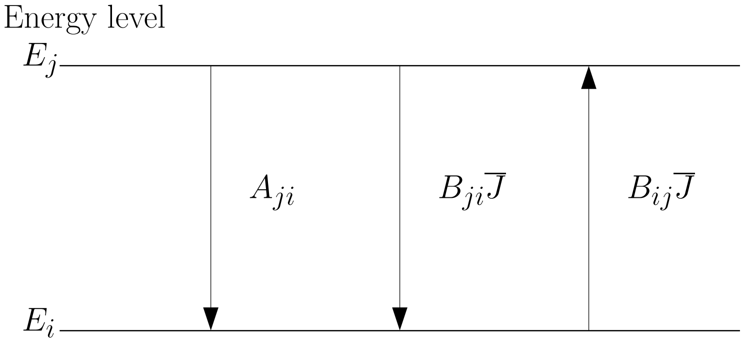

Figure 1.7: Transitions between the energy levels E_i and E_j of a given species and the Einstein probabilities. Adapted from Wilson et al. (2009).

For a system in a stationary state, the number of transitions per unit time per unit volume out of a given state should meet the number of transitions into this state. Hence, the number of absorbed and emitted photons are equal. Assuming that n_i and n_j correspond to the number densities of species in levels i and j, respectively, we find the relation (Rybicki and Lightman, 1985):

$$n_i B_{ij} \bar{J} = n_j A_{ji} + n_j B_{ji} \bar{J} \tag{1.17}$$

which in turn imply the following Einstein relations:

$$\begin{aligned} g_i B_{ij} &= g_j B_{ji} \\ A_{ji} &= \tfrac{2h\nu^3}{c^2} B_{ji} \end{aligned} \tag{1.18}$$

where g_1 and g_2 are the statistical weights of levels 1 and 2. Equation 1.18 must hold whether or not the system is under thermodynamic equilibrium. In figure 1.7, we present a schematic view of the processes that lead to transitions between the states 1 and 2 of a given species, and their corresponding Einstein coefficients.

1.5 Rotational transitions

Among the numerous molecules detected in the gas phase of the ISM, the vast majority of them (~80%) has been observed in their rotational lines (McGuire, 2018). Because of the low absolute energy associated with rotational levels, warm interstellar regions (such as hot cores) can provide enough energy to populate those levels, resulting in molecular emission spectra falling in submm/mm wavelengths (e.g., Belloche et al. 2013). Conversely, in colder interstellar environments (such as dark clouds), where there is not enough energy to supply a population distribution of the rotational energy levels, molecules can still be observed through absorption transitions against the background continuum (e.g., Neufeld et al. 2012). Thus, radio observations provide the advantage of enabling the search for molecular transitions in nearly any source. Indeed, the remarkable sensitivity and resolution attained by modern radio facilities (e.g., ALMA) result in extremely rich line surveys that represent an unique opportunity to thoroughly explore the chemical inventory of the ISM. Furthermore, the analysis of rotational lines can also give powerful information on the physical properties of the source (e.g., Blake et al. 1987; Goldsmith and Langer 1999), as well as its morphology and evolutionary stage (e.g., Wyrowski et al. 1999; Beuther et al. 2005; Guzmán et al. 2018). In this context, experimental and theoretical rotational spectroscopy share a symbiotic relationship that is fundamental to broaden our percipience of the physics and chemistry of the ISM (see, e.g., Puzzarini 2017; Puzzarini and Barone 2020; Cerqueira et al. 2020; Santos et al. 2020). In order to understand radio observations of molecular lines and its implications on astronomical matters, it is crucial to become acquainted with rotational spectroscopy and its theoretical description. Accordingly, we provide the main concepts involving non-linear rotors in the following subsections.

1.5.1 The types of rotors

In classical mechanics, the moment of inertia of a rigid rotor along an arbitrary axis (α) is defined as:

$$I_\alpha \equiv \sum_{i=1}^{n} m_i r_i^2 \tag{1.19}$$

where m_i is the mass of the ith particle and r_i is its distance to α. Consider a molecule with an axis that passes through its center of mass. In both ends of this axis, we mark a point where the distance to the center of mass corresponds to $I_\alpha^{-1/2}$. If we repeat the same procedure for the infinite number of axes that pass through the molecule's center of mass, we obtain an ellipsoidal surface known as the "ellipsoid of inertia". The three orthogonal axes of this ellipsoid are called the "principal inertial axes", a, b, and c, with corresponding moments of inertia I_a, I_b, and I_c (Levine, 1975; Hollas, 2004). In Figure 1.8, we show a sketch of the ellipsoid of inertia of H_2CO.

According to their moments of inertia, nonlinear molecules can be classified as spherical

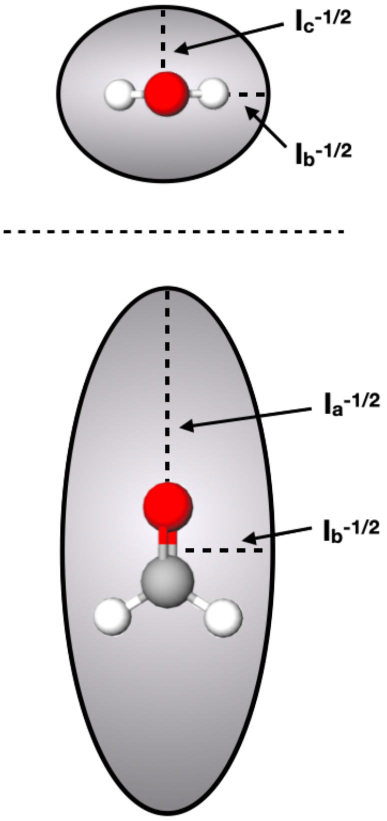

Figure 1.8: Sketch of the ellipsoid of inertia of H_2CO adapted from Levine (1975). Each cross-section contains two principal axes.

tops ($I_a = I_b = I_c$), prolate symmetric tops ($I_a \neq I_b = I_c$), oblate symmetric tops ($I_a = I_b \neq I_c$), or asymmetric tops ($I_a \neq I_b \neq I_c$). Analogously to linear molecules, we can define three rigid rotational constants, A, B, and C, as:

$$A \equiv \frac{h}{8\pi^2 I_a} \geq B \equiv \frac{h}{8\pi^2 I_b} \geq C \equiv \frac{h}{8\pi^2 I_c} \tag{1.20}$$

where, in the case of asymmetric tops, the B rotational constant can assume any value between A and C. Prolate and oblate symmetric tops, therefore, correspond to the limiting cases in which $B = C$ and $B = A$, respectively. In the present thesis, rotational lines of methyl acetylene (CH_3CCH), which is a symmetric top, were observed and used to explore the physical conditions of the source. Thus, special focus is given to this type of rotor. For more information on asymmetric tops, the reader is referred to specialized literature (e.g., Santos et al. 2020 and references therein).

1.5.2 The rotational Hamiltonian

The rotational energy of a rigid rotor is classically expressed as:

$$T_{rot} = \frac{1}{2}(I_a\omega_a^2 + I_b\omega_b^2 + I_c\omega_c^2) \tag{1.21}$$

where ω_a, ω_b, and ω_c are the angular velocities of the system with respect to the principal molecule-fixed axes a, b, and c. The rigid-rotor Hamiltonian can therefore be described as a kinetic energy operator expressed in terms of the components of the angular momentum $\hat{J}$ with relation to the principal axes (Gordy and Cook, 1984):

$$\hat{H}_{rot} = \frac{1}{2}\frac{\hat{J}_a^2}{I_a} + \frac{1}{2}\frac{\hat{J}_b^2}{I_b} + \frac{1}{2}\frac{\hat{J}_c^2}{I_c} \tag{1.22}$$

In an astrochemical context, a highly accurate description of the energy levels is needed in order to properly perform line assignments. Thus, corrections to the rotational Hamiltonian beyond the rigid-rotor and harmonic-oscillator approximations ought to be accounted for (i.e., centrifugal-distortion and vibrational-rotational-coupling effects). This complete Hamiltonian is obtained through a perturbation treatment of the rigid-rotor Hamiltonian, as described elsewhere (Mills 1972; Townes and Schawlow 1975, and references therein). As a result, the rotational Hamiltonian is defined in terms of the zeroth-order rotational constants (A, B, and C), and the higher-order centrifugal-distortion constants (e.g., D_J, D_{JK}, D_K, H_J, H_{JK}, H_{KJ}, and H_K, for symmetric tops). Those constants are measured from laboratory experiments guided by theoretical simulations (see Puzzarini et al. 2010 and references therein).

The energies of the rotational levels are the eigenvalues of this effective rotational Hamiltonian, which can be obtained by solving the secular equation (Levine, 1975):

$$\det\left[\langle\psi_m|\hat{H}|\psi_n\rangle - E_i\delta_{mn}\right] \tag{1.23}$$

For symmetric tops, those energy levels are described by two quantum numbers: J, which gives the total angular momentum, and K, which gives the angular momentum component along the molecule-fixed axis c:

$$\begin{gathered}\hat{J}^2|J,M,K\rangle = J(J+1)|J,M,K\rangle \\ \hat{J}_c|J,M,K\rangle = \pm K|J,M,K\rangle\end{gathered} \tag{1.24}$$

1.5.3 Dipole moment and selection rules

Rotational transitions are induced by the interaction of the molecule-fixed components of the electric dipole moment with the space-fixed components of the radiation field. Ergo, a permanent electric dipole moment is required in order for the molecule to interact appreciably with the microwave electromagnetic field, resulting in absorption or emission features. The intensities of the rotational transitions are proportional to the square of the dipole moment, which, for symmetric tops, lays along the molecular axis.

The selection rules for dipole radiation of a symmetric top are:

$$\begin{aligned} \Delta J &= 0, \pm 1 \\ \Delta K &= 0 \end{aligned} \tag{1.25}$$

That is to say, the electric dipole matrix elements will be nonzero only for the transitions given by those selection rules (Townes and Schawlow, 1975).

1.6 Rotational diagrams

Once believed to be barren, the ISM is nowadays well-known for harboring a myriad of different molecular, ionic, and radical species. With the advent of broadband heterodyne receivers—such as the memorable HIFI instrument on board of Hershel Space Observatory—spectral surveys teeming with rotational lines became wonted. Each one of those transitions is associated with a characteristic critical density and excitation energy, and thereby can be collectively employed as a very effective tool to study the physical properties of their environments. An overview of the probing capabilities of different molecular lines is shown in Figure 1.9.

A widely used technique to determine the molecule's excitation temperature and column density consists of constructing rotational diagrams using observed rotational lines (see Goldsmith and Langer 1999). Assuming that (*i*) the lines are optically thin, (*ii*) the source is homogeneous and fills the telescope beam, and (*iii*) the emission is thermalized, the observed line intensities can be converted into the upper level column density according to:

$$N_u = \frac{8\pi k \nu^2 \int T_a dv}{hc^3 A_{ji}} \tag{1.26}$$

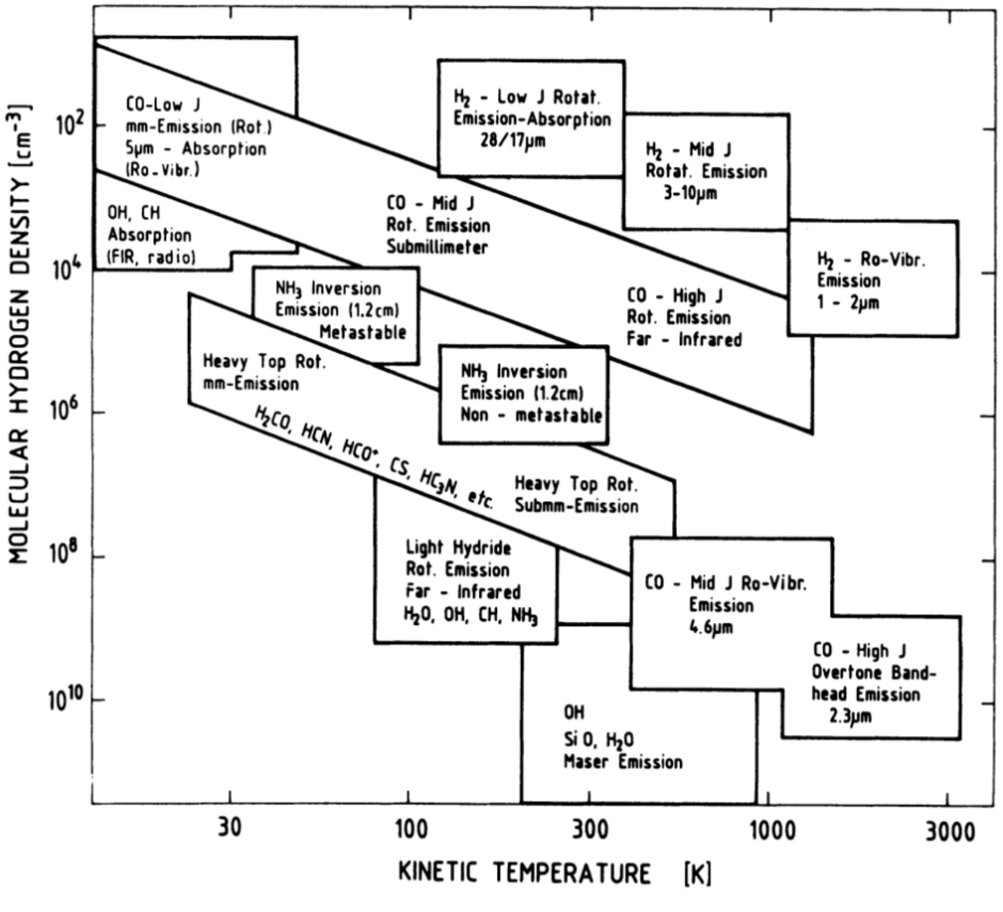

Figure 1.9: Overview of commonly used molecular diagnostics and the respective range of physical conditions that they trace. From Genzel 1991.

where ν and A_{ji} are the frequency and the Einstein A coefficient of the transition, respectively. $\int T_a dv$ is the integrated intensity of the line. Thus, N_u can be obtained directly from the observed radio spectra.

Under Local Thermodynamic Equilibrium (LTE), the level populations of a given species follow a Boltzmann distribution, and therefore can be characterized by a single excitation temperature (T_{exc}):

$$N_u = \frac{N_{tot}}{Q(T_{exc})} g_u \ \exp\left(-\frac{E_j}{kT_{exc}}\right) \tag{1.27}$$

where g_u is the statistical weight and E_u is the energy of the upper level. N_{tot} and $Q(T_{exc})$ are the total column density of the given species and its rotational partition function at a temperature T_{exc}, respectively.

By rewriting Equation 1.27, we derive the expression of the rotational diagram:

$$\ln\left(\frac{N_u}{g_u}\right) = \ln\left[\frac{N_{tot}}{Q(T_{exc})}\right] - \frac{E_j}{kT_{exc}} \tag{1.28}$$

Thus, a plot of $\ln(N_u/g_u)$ versus E_j of the observed transitions will correspond to a straight line, whose slope and y-intercept are defined by $-1/T_{exc}$ and $N_{tot}/Q(T_{exc})$, respectively. For completely thermalized transitions, the excitation temperature derived from the rotational diagram should equal the kinetic temperature (T_K) of the gas. If the molecule's transitions are not thermalized, however, the level populations deviate from the Boltzmann distribution, and so this approach becomes *kaput*.

1.6.1 Opacity correction factor

In a scenario where the emission has finite values of optical depth, a correction factor C_τ should be included on the right-hand side of Equation 1.28 (Goldsmith and Langer, 1999):

$$\ln\left(\frac{N_u}{g_u}\right) = \ln\left[\frac{N_{tot}}{Q(T_{exc})}\right] - \ln C_\tau - \frac{E_j}{kT_{exc}} \tag{1.29}$$

in which C_τ corresponds to a photon escape probability formulation:

$$C_\tau = \frac{\tau}{1 - e^{-\tau}} \tag{1.30}$$

For the limiting case of $\tau \ll 1$ (i.e., the optically thin scenario), $C_\tau \simeq 1$ and Equation 1.29 reduces to 1.28. Hence, if the emission is mistakenly assumed to be optically thin, each of the upper level populations will be underestimated by a factor C_τ, which will affect the derived N_{tot}. Moreover, since τ (and therefore C_τ) vary from line to line, the slope of the diagram will also be affected, leading to overestimated values of T_{exc}.

1.6.2 Beam dilution factor

For point-like sources, the assumption that the telescope beam is filled by the emission is preposterous. In this case, Equation 1.29, must be corrected by the so-called "beam-dilution factor" $(\Delta\Omega_a/\Delta\Omega_s)$:

$$\ln\left(\frac{N_u}{g_u}\right) = \ln\left[\frac{N_{tot}}{Q(T_{exc})}\right] - \ln C_\tau - \ln\left(\frac{\Delta\Omega_a}{\Delta\Omega_s}\right) - \frac{E_j}{kT_{exc}} \tag{1.31}$$

where $\Delta\Omega_a$ and $\Delta\Omega_s$ are, respectively, the beam solid angle and the source solid angle. In other words, when the emitting region does not fill the beam, the observed antenna temperatures will be systematically reduced by the beam dilution factor. This effect, in turn, will also influence the inferred optical depths. Moreover, for broad surveys encompassing a wide range of frequencies, such as the present work, the dilution factor does not remain constant for the whole spectral range. As a result, not only the derived N_{tot} but also T_{exc} are affected by this correction—or lack thereof.

1.7 The spectral tracer methyl acetylene

The present thesis revolves around the observed rotational lines of a particularly fruitful molecule: methyl acetylene (CH_3CCH). This species is a prolate symmetric rotor that pertains to the point group C_3v[4], and therefore its rotational transitions are characterized by the quantum numbers J and K (see §1.5). At standard temperature and pressure, it is a very flammable and reactive gas[5]. A 3D model of this molecule is presented In Figure 1.10, together with other important molecular tracers.

The earliest tentative detection of CH_3CCH in the interstellar medium (ISM) was reported by Buhl and Snyder (1973), toward the Sgr B2 molecular cloud. Later, Lovas

---

[4] `https://cccbdb.nist.gov/pglist.asp`

[5] `https://pubchem.ncbi.nlm.nih.gov/compound/Propyne`

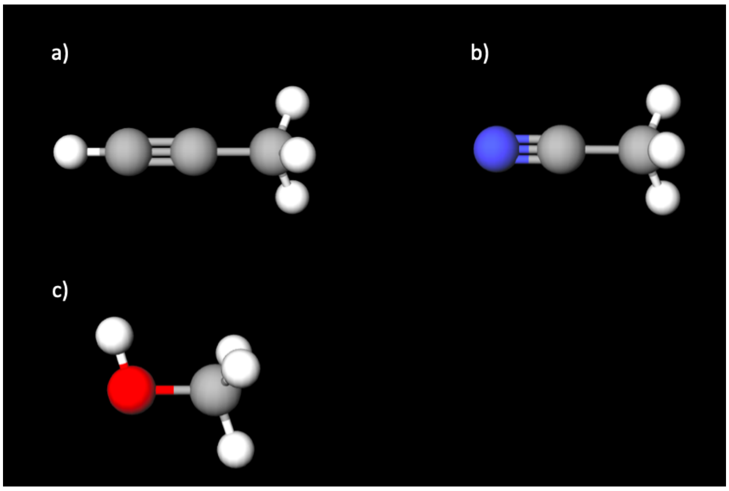

Figure 1.10: 3D models of the molecules CH_3CCH, CH_3CN and CH_3OH, for comparison purposes. Symmetric rotors: a) methyl acetylene (CH_3CCH) and b) acetonitrile (CH_3CN). Asymmetric rotor: c) methanol (CH_3OH). The white, gray, blue and red spheres correspond to the H, C, N and O atoms, respectively. Those three molecules have been observed in G331 (Hervías-Caimapo et al., 2019), and play an important role in the inference of the physical conditions of HMCs and related sources.

et al. (1976) observed CH_3CCH, among other molecules containing the methyl group (e.g., CH_3OH, CH_3CN and CH_3CHO), toward the Orion A region. In the following years, Hollis et al. (1981) performed a survey toward Sgr B2 and recorded new observations of CH_3CCH that confirmed Buhl & Snyder's detection. Similarly, Kuiper et al. (1984) conducted a successful search for CH_3CCH in Sgr B2, as well as in various other dense interstellar clouds. Since its first detection, CH_3CCH has been extensively studied toward star-forming regions (e.g., Zhang et al. 2014; Taniguchi et al. 2018; Guzmán et al. 2018; Bøgelund et al. 2019; Calcutt et al. 2019), and has proven to be a reliable tracer of their physical conditions (e.g., Bergin et al. 1994). It has also been observed toward extagalactic sources, such as M 82, NGC 253, and NGC 1068 (Mauersberger et al., 1991; Qiu et al., 2020), and even toward a planetary nebula, as recently reported by Schmidt and Ziurys (2019). As a matter of fact, the widespread detection of CH_3CCH even extends to planetary atmospheres (e.g., de Graauw et al. 1997; Fouchet et al. 2000; Burgdorf et al. 2006; Cordiner et al. 2015).

Formation pathways of CH_3CCH in the gas-phase have been extensively investigated. Ion-neutral routes with $C_2H_2^+$ as a precursor (Schiff and Bohme, 1979; Millar and Freeman, 1984), neutral-neutral reactions such as $CCH + CH_4 \rightarrow CH_3CCH + H$ (Turner et al., 1999), as well as dissociative recombination reactions involving larger hydrocarbons (Calcutt et al., 2019) are all subsumed under the suggested gaseous formation routes of CH_3CCH. However, those pathways alone fail to reproduce the observed abundances in dense molecular clouds (Li et al., 2013; Öberg et al., 2013; Vastel et al., 2014). For this reason, grain-surface reactions are additionally proposed as formation routes (Hickson et al., 2016; Guzmán et al., 2018). If this is the case, however, its solid-phase formation and consecutive desorption mechanisms should be efficient at temperatures as low as ∼20 K, as pointed out by Giannetti et al. (2017). Moreover, Qasim et al. (2019) have shown that solid-phase methyl acetylene can play an important role as a precursor of alcohols under dark-cloud conditions. Using a combination of experiments and theoretical chemistry, they found that n-propanol ($CH_3CH_2CH_2OH$) and isopropanol ($(CH_3)_2CHOH$) were efficiently formed at low temperatures (T=10 K) and without any energy input (such as UV radiation or cosmic rays), through the radical-addition reaction of $CH_3CCH + OH$.

Because it is a symmetric rotor, the rotational levels of CH_3CCH with a given J quantum number are divided into multiple levels with different K quantum numbers (see Figure 1.11). The effects of centrifugal distortion lead to small energy differences between each K level, splitting their degeneracy. As a result, for each J transition, there are many lines with different K quantum numbers encompassing a wide range of energies above the ground state. Those different K lines with the same J quantum numbers—the so-called K-ladders—are closely spaced in frequency, and therefore can all be observed in the same bandwidth. This procedure has the advantage of reducing calibration uncertainties, thus yielding more precise predictions. Moreover, due to its small electric dipole moment ($\mu = 0.75$ D, Dubrulle et al. 1978), line thermalization occurs at densities as low as $\sim 10^4$ cm^{-3} (e.g., Bergin et al. 1994; Fontani et al. 2002; Molinari et al. 2016), well below the expected density at G331 ($n(H_2) \sim 10^7$ cm^{-3}, Mendoza et al. 2018). Thus, the LTE requirement for the rotational diagram analysis (see §1.6) is easily met. Furthermore, since the dipole moment for symmetric tops lays parallel to the symmetry axis, radiative transitions with $\Delta K \neq 0$ are forbidden. As a result, the relative population of the K-ladders are dictated by the kinetic temperature of the colliding particles, which makes CH_3CCH an excellent temperature probe.

This molecule is generally observed to have an extended emitting region and to trace relatively cold gas (Fontani et al., 2002; Bisschop et al., 2007; Giannetti et al., 2017; Andron et al., 2018). It is also highly sensitive to the warm-up process that takes place during the development of a hot core (Giannetti et al., 2017). Indeed, methyl acetylene provides a cornucopia of powerful information on the physics and chemistry of the environment. Its

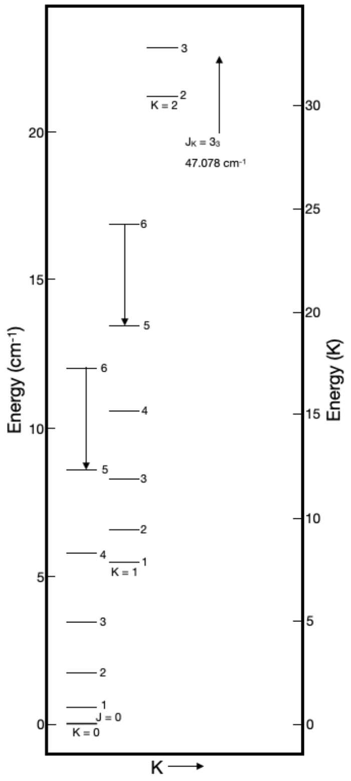
3
2
K = 2
$J_K = 3_3$
47.078 cm^{-1}
6
5
6
4
5
3
2
4
1
K = 1
3
2
1
J = 0
K = 0
Energy (cm^{-1})
0
5
10
15
20
Energy (K)
0
5
10
15
20
25
30
K →

Figure 1.11: Rotational energy levels of CH_3CCH. Adapted from Kuiper et al. (1984).

temperature probing potential can go even beyond the statistically-averaged, large-scale analysis obtained through rotational diagrams. Rather, as is going to be elucidated along this thesis, the intrinsic spectroscopic properties of CH_3CCH allows not only to assess the overall temperature of the source, but also to explore its small scale temperature profile even with single-dish data.

Chapter 2

Facilities and methods

In this chapter, we outline the different steps executed throughout this research project to explore the excitation conditions of CH_3CCH in the HMC G331. Those include: information on the facilities, observations, and subsequent data reduction procedures, a description of the line-fitting and LTE-analysis techniques, as well as an overview of the theoretical-chemistry methods that were employed in order to further investigate the observed spectra. Since the relevant theoretical background has been addressed in the previous chapter (see §1), we will hereupon focus on a pragmatic approach to the routines and technicalities associated with those methods (e.g., software, keywords, and other apposite details).

2.1 The Atacama Pathfinder EXperiment (APEX)

In the present work, the physical properties of G331 were explored using molecular line observations from the APEX radio telescope. For this reason, we now give a brief introduction on this facility. See Figure 2.1 for a prepossessing picture of the antenna.

The 12 m Atacama Pathfinder EXperiment (APEX) telescope is located at Llano de Chajnantor, in northern Chile, at an altitude of ~5100 m above the sea level. It is a collaboration between the Max Planck Institut für Radioastronomie (45% observing time), the European Southern Observatory (24%), and the Onsala Space Observatory (21%). As the host country for the project, Chilean research institutions have access to 10% of the available observing time.

APEX is based on an ALMA prototype antenna modified to suit single-dish operations. It was manufactured by VERTEX Antennentechnik GmbH, in Germany, and started

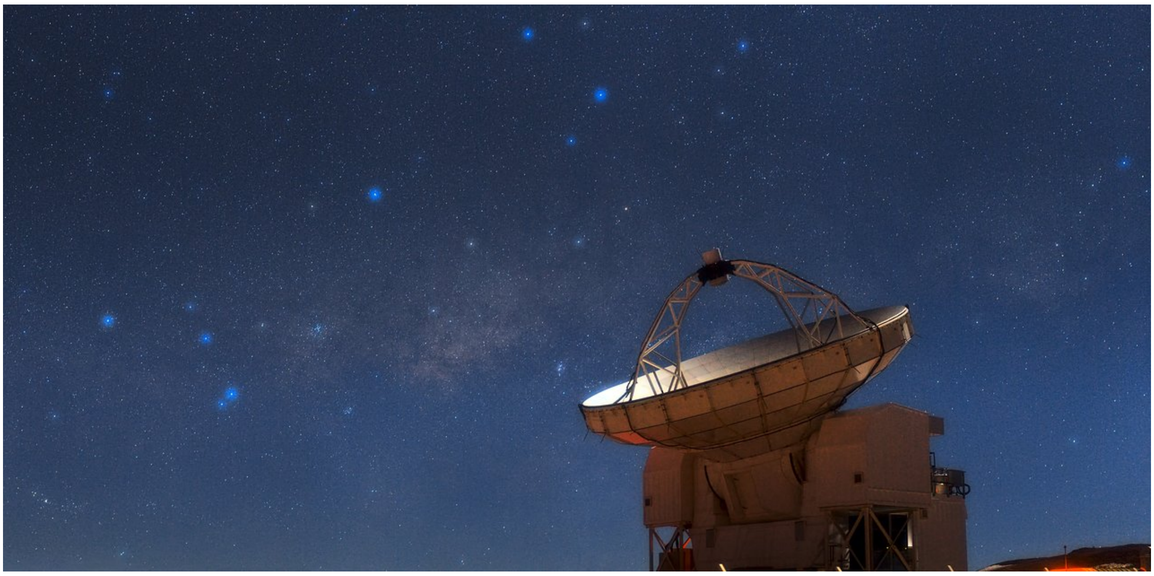

Figure 2.1: APEX 12 m telescope. Credit: ESO/B. Tafreshi

operating in 2005. The telescope is built over an alt-azimuthal mount, and consists of a Cassegrain system with a paraboloidal main reflector. The effective surface accuracy is calculated to be ∼17 μm rms (Güsten et al., 2006). Because of the high altitude, the amount of Precipitable Water Vapor (PWV) at the APEX site is typically 1.0 mm and falls below 0.5 mm ≤25% of the time.[1]

The instrumentation programme at APEX is very extense and diverse. Multiple facilities are available in order to cover a broad range of scientific purposes. In the present work, two different instruments were used to conduct our spectral survey of CH_3CCH toward G331: the Swedish Heterodyne Facility Instrument (SHeFI) and the Swedish-ESO PI Instrument (SEPIA). General information on those insruments are given below.

2.1.1 SHeFI

Decommissioned since 2017, the Swedish Heterodyne Facility Instrument (SHeFI) consisted of four wide-band heterodyne receiver channels located in the Nasmith cabin A of APEX. Since SHeFI only allows observations with one frequency band at a time, a channel-switching mirror directs the beam into a specific channel window. The coupled cryostat is equipped with a liquid He pot for temperature stabilization, and yields temperatures of ∼3.6 K.

Collectively, the four bands of SHeFI covered a frequency range between 211 and 1390

---

[1] `http://www.apex-telescope.org/ns/weather/`

GHz. Their information are summarized in Table 2.1.[2] For more details on the instrument configuration and on each particular channel, see Vassilev et al. (2008).

Table 2.1 - Frequency channels of the SHeFI instrument. SIS stands for superconductor-insulator-superconductor mixer; SSB stands for single sideband receiver; HEB stands for hot electron bolometer mixer; and DSB stands for double sideband receiver.

APEX Band	Frequency GHz	Technology	*HPBW* arcsec
1	213–275	SIS,SSB	30-23
2	267–378	SIS,SSB	23-17
3	385–506	SIS,DSB	17-13
4	1250–1390	HEB, DSB	5

2.1.2 SEPIA

The Swedish-ESO PI Instrument (SEPIA) was brought to APEX in the beginning of 2015 and installed in Cabin A. At the moment, it accommodates three ALMA-like heterodyne receivers (the so-called “cartridges”): SEPIA660, SEPIA345, and SEPIA180. Their information is summarized in Table 2.2.[3]

Table 2.2 - Frequency channels of the SEPIA instrument. SIS stands for superconductor-insulator-superconductor mixer and 2SB stands for dual sideband receiver.

SEPIA	Frequency GHz	Technology	*HPBW* arcsec
660	597–725	SIS,2SB	10-9
345	272–376	SIS,2SB	23-17
180	157–211	SIS,2SB	39-30

Similarly to SHeFI, only one receiver can be used at a given time. However, this issue is partially mitigated by the fast switching time between receivers (of only a few minutes). More information on this instruments, and particularly on the SEPIA180 receiver—also known as SEPIA-B5—can be found in Belitsky et al. (2018).

---

[2] `http://www.apex-telescope.org/heterodyne/shfi/`

[3] `http://www.apex-telescope.org/ns/instruments/sepia/`

2.2 *Observations and data calibration*

The observations were obtained with APEX 12 m telescope (Güsten et al., 2006) (see §2.1), toward the coordinates RA, DEC = $16^h12^m10.1^s$, $-51°28'38.1''$. We employed the Band 5 receiver of the Swedish-ESO PI Instrument (SEPIA-B5; Belitsky et al. 2018), together with APEX-1 and APEX-2 receivers of the Swedish Heterodyne Facility Instrument (SHeFI; Vassilev et al. 2008), to observe nine frequency setups within the intervals 170.8–205.1 GHz and 222–307.6 GH, respectively. As backend, the eXtended bandwidth Fast Fourier Transform Spectrometer2 (XFFTS2) was used, which consists of two units with 2.5 GHz bandwidth divided into 32768 channels each. The spectral resolution, corresponding to velocity resolutions, was obtained between 0.15 and 0.25 km s^{-1} for a noise level of ~30–50 mK.

The signal received from the sky is converted from the telescope count units to units of antenna temperature T$_A$ by observing a load with controlled temperature and comparing it to observations of the sky. T$_A$ is generally given by the expression (Milligan, 2005):

$$T_A = \frac{1}{4\pi} \int_0^{2\pi} \int_0^{\pi} G(\theta, \varphi) T_S(\theta, \varphi) \sin(\theta) d\theta d\varphi \tag{2.1}$$

where $G(\theta, \varphi)$ is the antenna's gain pattern and $T_S(\theta, \varphi)$ is the temperature distribution of the environment.

Atmospheric models are employed to aid the correction for atmospheric effects (Dumke and Mac-Auliffe, 2010). Moreover, the sky background is subtracted from the signal by means of the ON/OFF switching mode, in which the pointing direction of the antenna main-beam is switched repeatedly between an ON position and a reference position. This OFF position should not be too far (in terms of celestial coordinates) from the ON position. Thus, assuming that the broadband emission from the sky, ground, and/or continuum sources are similar at both ON and OFF positions, spatial and temporal signal fluctuations are canceled.

The antenna temperature, T$_A$, is then converted to the main-beam brightness temperature by:[4]

$$T_{mb} = T_A \, \frac{\eta_{fw}}{\eta_{mb}} \tag{2.2}$$

---

[4] `http://www.apex-telescope.org/telescope/efficiency/`

where η_{fw} and η_{mb} are the forward and main beam efficiencies, respectively. For all observations, $\eta_{fw} = 0.95$, whereas η_{mb}= 0.82 for SEPIA-B5 (Galametz et al., 2016; Zahorecz et al., 2017), and η_{mb}= 0.75 and 0.73 for APEX-1 and APEX-2, respectively (Mendoza et al., 2018; Duronea et al., 2019). The Half Power Beam Width (HPBW) varies between ∼17–39″ for the entire frequency range. We adopted a calibration uncertainty of about 10% (Dumke and Mac-Auliffe, 2010), and a surface accuracy (rms) of 17 μm.[5]

2.3 Data reduction

The data reduction was carried out using the CLASS package of the Grenoble Image and Line Data Anlysis Software (GILDAS).[6] This software has been adopted as the standard reduction package for APEX, and consists of five programs with different utilities:

- CLASS (Continuum and Line Analysis Single-dish Software), dedicated to processing single-dish data;
- GREG (Grenoble Graphic), dedicated to 1-D and 2-D imaging;
- ASTRO, dedicated to preparing observing sessions;
- CLIC (Continuum and Line Interferometric Calibration), dedicated to calibrating data from the NOEMA interferometer;
- Mapping, dedicated to interactive imaging and deconvolution.

First, the observations were inspected and those with calibration errors were discarded. Then, first-degree polynomial baselines were removed from each individual scan, by means of the *base* command. Finally, the baseline-corrected observations were averaged into a final spectrum using the *stitch* command.

2.4 Line identification and gaussian fitting

Line identifications were performed using the Weeds extension of CLASS, in combination with spectroscopic databases such as NIST[7] Recommended Rest Frequencies for

---

[5] `http://www.apex-telescope.org/telescope/`

[6] `https://www.iram.fr/IRAMFR/GILDAS/`

[7] `https://physics.nist.gov/cgi-bin/micro/table5/start.pl`

Observed Interstellar Molecular Microwave Transitions (Lovas, 2004), CDMS[8] (Endres et al., 2016), JPL[9] (Pickett et al., 1998), and Splatalogue[10]. The following criteria were defined to perform the identification:

- The peak frequencies of the observed lines should be consistent with $V_{lsr} \sim -90$ km s^{-1} (the systemic velocity of G331);
- The intensities of the observed lines should surpass the threshold of 3σ;
- Lines predicted through LTE modeling should agree with the observations to a reasonable extent.

The last requirement of the list involves a well defined rotational temperature—which is obtained through a rotational diagram analysis—and thus will be discussed in §2.5.2. In addition to Weeds, the CASSIS[11] software was used to confirm the detected lines. Moreover, we also inspected the identified lines for contamination by adjacent molecular transitions, by means of the line search engine within Weeds.

The spectroscopic properties of the lines were obtained through fitting a single gaussian profile to each line. This was performed by the *method gauss* command, whose fitted parameters are: area, position, and width. For features not completely resolved, the single gaussian fitting was ensured by means of the *set mask* keyword, which selects regions of the spectrum to be excluded from the fit. An example of this procedure is shown in Figure 2.2, where the observed $CH_3CCH(10_0–9_0)$ line is depicted together with its gaussian fitting.

2.5 LTE analyses

2.5.1 Rotational diagrams

The rotational diagram analysis (see §1.6) was carried out with CASSIS. In order to properly infer T_{exc} and N_{tot}, the error bars of the points in the diagram must be taken into account when fitting the 1^{st} order polynomial. The integrated area uncertainty is given by:

---

[8] `https://cdms.astro.uni-koeln.de/`

[9] `https://spec.jpl.nasa.gov/`

[10] `https://www.cv.nrao.edu/php/splat/`

[11] `http://cassis.irap.omp.eu/`

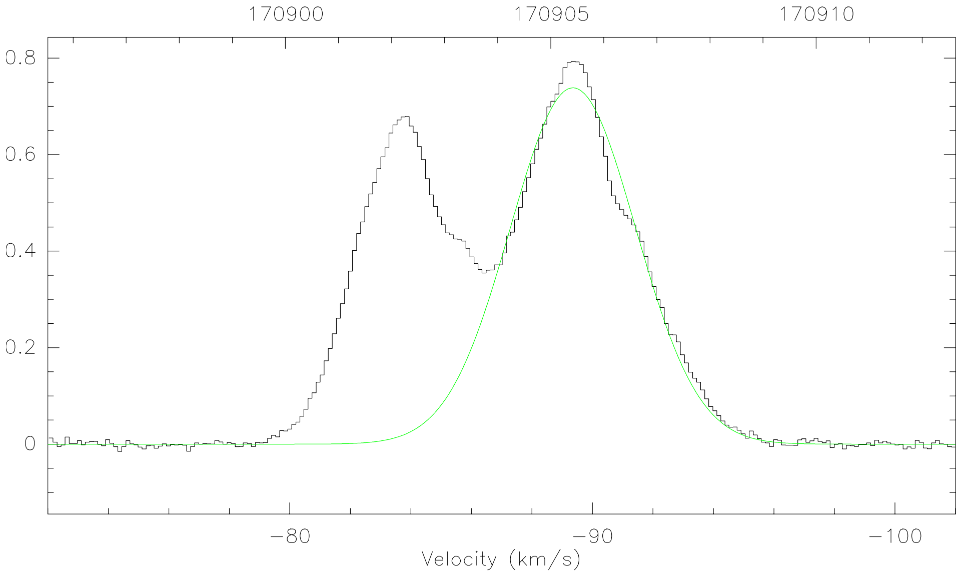

Figure 2.2: Gaussian fitting of the $CH_3CCH(10_0–9_0)$ line (green) over the observed spectrum (black). The upper and lower x-axes are given in frequency units (MHz) and velocity units (km s^{-1}), respectively. The y-axis is given in temperature units (K).

$$\Delta W = \sqrt{(cal/100 \times W)^2 + (rms\sqrt{2 \times FWHM \times \Delta v})^2} \tag{2.3}$$

where W is the integrated area (K km s^{-1}), rms is the noise around the selected species (K), FWHM is the fitted Full Width at Half Maximum (km s^{-1}), Δv is the bin size (km s^{-1}), and cal is the calibration value (∼10%). The plotted uncertainties are, thus:

$$\Delta \left(\ln \frac{N_u}{g_u} \right) = \frac{\Delta W}{W} \tag{2.4}$$

The uncertainties on the fitted parameters (T_{exc} and N_{tot}) are related, respectively, to the slope (a) and the y-intercept (b) of the fitted polynomial (i.e., y=ax+b). Since $T_{exc} = -1/a$ and $N_{tot} = Q(T_{exc}) \times e^b$, it yields:

$$\begin{gathered} \Delta T_{exc} = \tfrac{\Delta a}{a^2} \\ \Delta N_{tot} = Q(T_{exc}) \times \Delta b \times e^b \end{gathered} \tag{2.5}$$

The opacity correction (see §1.6.1) is incorporated iteratively by means of Equations 1.28 and 1.29, until a solution for T_{exc} and N_{tot} converges. The convergence criterion was defined as $\epsilon = 1\%$—that is to say, the values are deemed converged when the difference between the last two iterations is smaller than 1%.

The quality of the fit can be assessed through its reduced χ^2 values, in which the degrees of freedom correspond to:

$$dof = n - 2 \tag{2.6}$$

where n is the number of points on which the fit was performed. Since two values are extracted from the fit (T$_{exc}$ and N$_{tot}$), we must subtract 2 from n. Thus, χ^2_{red} is given by:

$$\chi^2_{red} \times dof = \sum_{i=1}^{n} \frac{(y_i - y)^2}{\sigma} \tag{2.7}$$

where σ corresponds to the uncertainty of the points (see Equation 2.4). The closer χ^2_{red} is to 1, the better is the fit.

2.5.2 Synthetic LTE spectra

The Weeds extension of CLASS allows to simulate molecular emission under the assumption of LTE (see Maret et al. 2011). The input parameters for each species are T$_{exc}$, N$_{tot}$, FWHM, as well as the source's systemic velocity and size. The LTE spectrum of a given species is computed by:

$$T_B(\nu) = \eta\,[J_\nu(T_{exc}) - J_\nu(T_{bg})]\,(1 - e^{-\tau(\nu)}) \tag{2.8}$$

where η is the beam dilution factor (see §1.6.2), T$_{bg}$ is the brightness temperature of the background emission (e.g., 2.73 K for the Cosmic Microwave Background (CMB)), and $\tau(\nu)$ is the opacity. The modeled lines can thus appear in absorption or emission, depending on the continuum and line excitation temperatures. Multiple species and/or components can be computed simultaneously, resulting in a spectrum that is the sum of the brightness temperature of each species/component given by Equation 2.8. In this case, it is assumed that the different species/components are not coupled radiatively, viz. one species/component will not absorb photons from another species/component.

The resulting model should, therefore, closely resemble the observed spectrum—provided the LTE assumption is met. For emission features, the background is computed as the sum of the CMB and the source continuum emission, which is assumed to be optically thin. Moreover, the continuum is presupposed to be originated from a location behind the medium where the lines are produced.

2.6 Rotational-spectrum simulations

Aside from radio-astronomical techniques, the present work also utilizes quantum-chemistry methods to explore the observations of CH_3CCH in a molecular level. The rotational spectrum of CH_3CCH was simulated at various temperatures using the PGOPHER (Western, 2017) general purpose software, which performs the diagonalization of the appropriate Hamiltonian matrix to yield the rotational energy levels (see §1.5).

For symmetric tops, such as CH_3CCH, the rotational Hamiltonian is standard (Papousek and Aliev, 1982), and yields ground-vibrational-state rotational energies according to:

$$\begin{aligned} E_{J,K} = {} & BJ(J+1) + (A-B)K^2 - D_J J^2(J+1)^2 - D_{JK} J(J+1)K^2 - D_K K^4 \\ & + H_J J^3(J+1)^3 + H_{JK} J^2(J+1)^2 K^2 + H_{KJ} J(J+1)K^4 + H_K K^6 \end{aligned} \tag{2.9}$$

The experimental rotational constants, centrifugal distortion constants, and dipole moment used in the simulations were taken from the JPL[12] database. The transition intensities are given by (Western, 2017):

$$I = \frac{S}{Q(T)} \left[\exp\left(-\frac{E_i}{kT}\right) - \exp\left(-\frac{E_j}{kT}\right) \right] \tag{2.10}$$

which is simply the line strength S times the Boltzmann factor, normalized to the temperature-dependent rotational partition function $Q(T)$ at the given temperature. E_i and E_j correspond to the energies of the lower and the upper states, respectively.

The temperature-dependent partition function for a molecule, $Q(T)$, is defined as:

$$Q(T) = \sum g_i e^{-E_i/kT} \tag{2.11}$$

where g_i is the statistical weight and E_i is the energy of the ith state. The computation is assumed to have converged when the highest J values have a contribution of $< 10^{-4}$ to the overall sum.

---

[12] `https://spec.jpl.nasa.gov/`

Chapter 3

Results and discussion

3.1 Line properties

In the present thesis, we have conducted a spectral survey of methyl acetylene toward the HMC G331. In total, 41 uncontaminated lines of CH_3CCH were detected within a frequency range from $\sim$170840 MHz to $\sim$307600 MHz. In other words, all the detected lines satisfy the criteria listed in §2.4 and no plausible line contamination was identified nearby the transitions. Those lines are distributed in nine different K-ladders, ranging from the J=10–9 to J=18–17 rotational levels, all of which are displayed in Figure 3.1. For all 41 detected lines, the ratios of line intensity to baseline rms were $\gtrsim$5.2, well above the 3σ threshold. For example, the baseline reduction of the $J=10_K$–9_K K-ladder yielded an rms of $\sim5.8\times10^{-3}$ K, whereas the intensity of the $J=10_4$–9_4 transition—which is the faintest detected line within this K-ladder—corresponds to $\sim6.3\times10^{-2}$ K. The resulting intensity/rms ratio is $\sim$10.8. Such a large number of detected lines provide an unique opportunity to explore the physical conditions of G331 with remarkably robust statistics. Isotopologue transitions were not unequivocally identified and therefore were not considered in our analyses.

Spectroscopic parameters obtained through single gaussian fittings of the lines are summarized in Table 3.1. In reality, most lines profiles require more components to be fitted accurately (e.g., Roberts et al. 2011; Galván-Madrid et al. 2013), warranting more demanding line fitting procedures. This level of sophistication, however, is beyond the scope of this work—for our purposes, a simplified approach suffices. For each observed J_u level, all transitions with K=3–0 were detected. In some cases (see Table 3.1), lines with K=4 were not detectable above the 3 sigma threshold. Nevertheless, all K-ladders

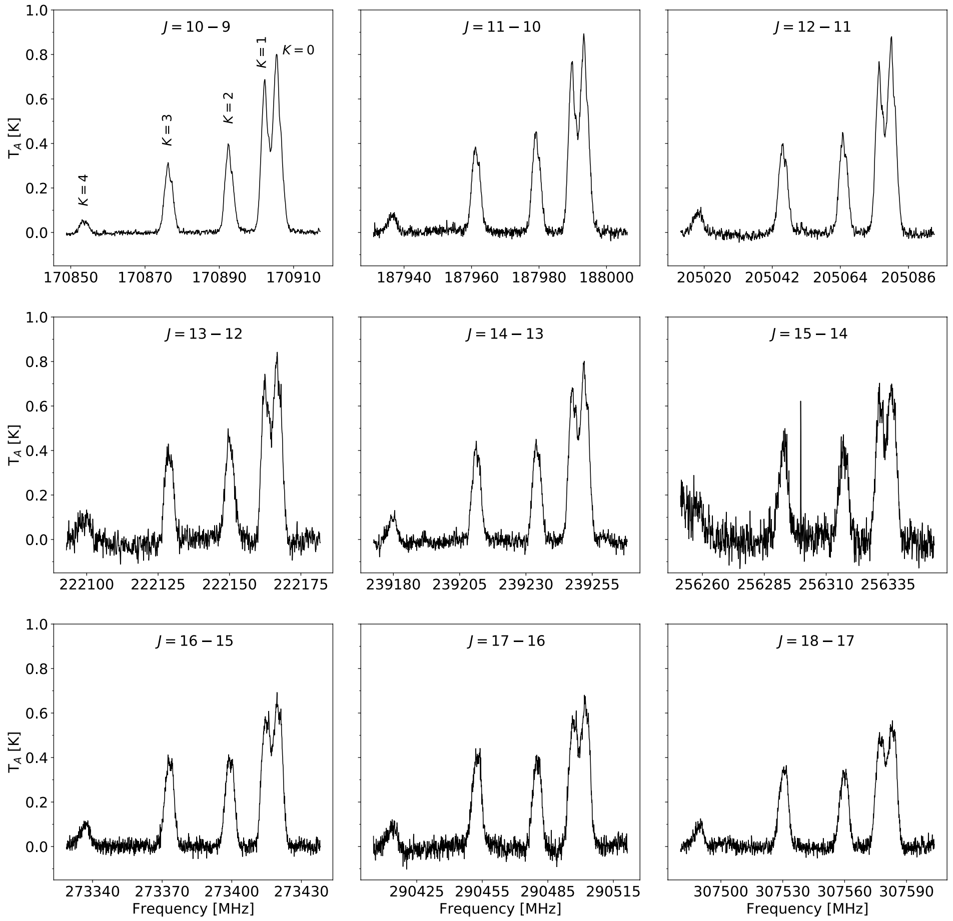

Figure 3.1: Spectra of CH_3CCH exhibiting the different K-ladders identified from J=10–9 to J=18–17. For each spectrum, a linear baseline was subtracted. K-level transitions are indicated for the J=10–9 K-ladder.

include a minimum of four detected transitions. The CH_3CCH lines present a low velocity dispersion ($\leq$ 0.68 km s^{-1}) around the systemic velocity of the source (V_{sys}=-90 km s^{-1}), and a mean systemic velocity of $\bar{V}_{lsr}$ = -90.007 ± 0.007 km s^{-1}. Observed line widths also show an overall small dispersion, with FWHM values ranging from 4.15 to 5.68 km s^{-1}. Moreover, line profiles are narrow, with average values of 4.94 ± 0.77 km s^{-1}. Hervías-Caimapo et al. (2019) have observed several molecular lines toward G331 and classified them according to the line profile, with narrow lines tracing the emission from the core ambient medium and lines with broad wings tracing the outflow and shocked region (see §1.3.1). Accordingly, we expect from the narrow line profiles that the observed CH_3CCH emission is originated from a quiescent (not expanding) core medium.

The K-ladder spectral profile characteristic of symmetric tops is particularly advantageous because of the wide range of energies associated with the different levels contained

Table 3.1 - Spectral lines of CH_3CCH observed toward G331 and their parameters obtained from Gaussian fits.

Quantum Numbers					Frequency	E_{up}	A_{ij}	$\int T_A dv$	V_{lsr}	FWHM
J_u	K_u	–	J_l	K_l	(MHz)	(K)	(1×10^{-5} s^{-1})	(K km s^{-1})	(km s^{-1})	(km s^{-1})
10	4		9	4	170853.576	160.7	1.43	0.23973 ± 0.01	-90.016 ± 0.09	4.382 ± 0.187
10	3		9	3	170876.41	110.1	1.55	1.4306 ± 0.015	-89.886 ± 0.024	4.571 ± 0.057
10	2		9	2	170892.726	74	1.63	1.7501 ± 0.022	-89.775 ± 0.027	4.415 ± 0.064
10	1		9	1	170902.518	52.3	1.68	3.0455 ± 0.062	-89.739 ± 0.044	4.439 ± 0.115
10	0		9	0	170905.783	45.1	1.70	3.9471 ± 0.04	-89.341 ± 0.024	4.994 ± 0.065
11	4		10	4	187936.23	169.7	1.97	0.38405 ± 0.013	-90.404 ± 0.081	4.763 ± 0.195
11	3		10	3	187961.342	119.2	2.10	1.8727 ± 0.019	-89.965 ± 0.023	4.677 ± 0.055
11	2		10	2	187979.286	83	2.20	2.0664 ± 0.024	-89.842 ± 0.025	4.451 ± 0.058
11	1		10	1	187990.055	61.4	2.25	3.5301 ± 0.071	-89.835 ± 0.044	4.568 ± 0.115
11	0		10	0	187993.645	54.1	2.27	4.4260 ± 0.044	-89.389 ± 0.024	5.06 ± 0.064
12	4		11	4	205018.114	179.6	2.63	0.48566 ± 0.015	-89.886 ± 0.074	4.98 ± 0.177
12	3		11	3	205045.501	129	2.77	1.9662 ± 0.021	-89.988 ± 0.025	4.805 ± 0.059
12	2		11	2	205065.07	92.9	2.88	2.0374 ± 0.021	-89.856 ± 0.023	4.518 ± 0.052
12	1		11	1	205076.816	71.2	2.94	3.5154 ± 0.065	-89.936 ± 0.041	4.632 ± 0.105
12	0		11	0	205080.732	64	2.96	4.4571 ± 0.049	-89.43 ± 0.027	5.184 ± 0.071
13	3		12	3	222128.815	139.7	3.57	1.9676 ± 0.037	-90.04 ± 0.043	4.551 ± 0.096
13	2		12	2	222150.01	103.5	3.69	2.3272 ± 0.031	-90.068 ± 0.031	4.841 ± 0.076
13	1		12	1	222162.73	81.9	3.75	3.7371 ± 0.09	-90.149 ± 0.058	5.019 ± 0.152
13	0		12	0	222166.971	74.6	3.78	4.4326 ± 0.062	-89.522 ± 0.035	5.241 ± 0.09
14	4		13	4	239179.281	201.7	4.34	0.44333 ± 0.016	-90.617 ± 0.073	4.154 ± 0.177
14	3		13	3	239211.215	151.1	4.51	2.0168 ± 0.027	-90.153 ± 0.03	4.554 ± 0.068
14	2		13	2	239234.034	115	4.63	2.0813 ± 0.026	-90.092 ± 0.028	4.512 ± 0.065
14	1		13	1	239247.728	93.3	4.70	3.6931 ± 0.074	-90.295 ± 0.049	5.209 ± 0.13
14	0		13	0	239252.294	86.1	4.73	4.2518 ± 0.058	-89.497 ± 0.034	5.337 ± 0.09
15	3		14	3	256292.63	163.4	5.59	2.2953 ± 0.057	-90.14 ± 0.058	5.113 ± 0.159
15	2		14	2	256317.071	127.3	5.72	2.1340 ± 0.056	-90.023 ± 0.062	4.907 ± 0.153
15	1		14	1	256331.739	105.7	5.80	3.2272 ± 0.065	-90.145 ± 0.045	4.765 ± 0.117
15	0		14	0	256336.629	98.4	5.83	3.9996 ± 0.055	-89.538 ± 0.037	5.426 ± 0.09
16	4		15	4	273336.519	227.1	6.64	0.58055 ± 0.019	-90.296 ± 0.08	5.451 ± 0.223
16	3		15	3	273372.99	176.6	6.84	2.0837 ± 0.024	-90.173 ± 0.027	4.913 ± 0.067
16	2		15	2	273399.051	140.4	6.97	2.1294 ± 0.025	-90.157 ± 0.027	4.931 ± 0.069
16	1		15	1	273414.692	118.8	7.06	3.4784 ± 0.061	-90.417 ± 0.043	5.529 ± 0.118
16	0		15	0	273419.906	111.5	7.09	3.8163 ± 0.021	-89.664 ± 0.025	5.478 ± 0.09
17	3		16	3	290452.224	190.5	8.25	2.3997 ± 0.049	-90.469 ± 0.044	5.426 ± 0.142
17	2		16	2	290479.904	154.4	8.40	2.0727 ± 0.033	-90.275 ± 0.033	4.931 ± 0.102
17	1		16	1	290496.516	132.7	8.49	3.5350 ± 0.062	-90.682 ± 0.044	5.679 ± 0.122
17	0		16	0	290502.054	125.5	8.52	3.8137 ± 0.054	-89.882 ± 0.036	5.448 ± 0.096
18	3		17	3	307530.263	205.3	9.84	1.8777 ± 0.021	-90.228 ± 0.027	4.899 ± 0.065
18	2		17	2	307559.559	169.1	1.00	1.7264 ± 0.02	-90.227 ± 0.028	4.764 ± 0.066
18	1		17	1	307577.141	147.5	1.01	2.9083 ± 0.038	-90.496 ± 0.033	5.394 ± 0.084
18	0		17	0	307583.003	140.3	1.01	3.2710 ± 0.052	-89.758 ± 0.042	5.575 ± 0.11
J_u	K_u	–	J_l	K_l	Frequency (MHz)	E_{up} (K)	A_{ij} (1×10^{-5} s^{-1})	$\int T_A dv$ (K km s^{-1})	V_{lsr} (km s^{-1})	FWHM (km s^{-1})

within each ladder (see Table 3.1). The energy distribution of those different levels plays an important role in the interpretation of the observed data and the analyses performed on them. In Figure 3.2, a plot of the Einstein A coefficient versus the energy of each observed CH_3CCH rotational level is presented. The transitions are grouped according to their K transitions, in order to facilitate comparisons between different K-ladders.

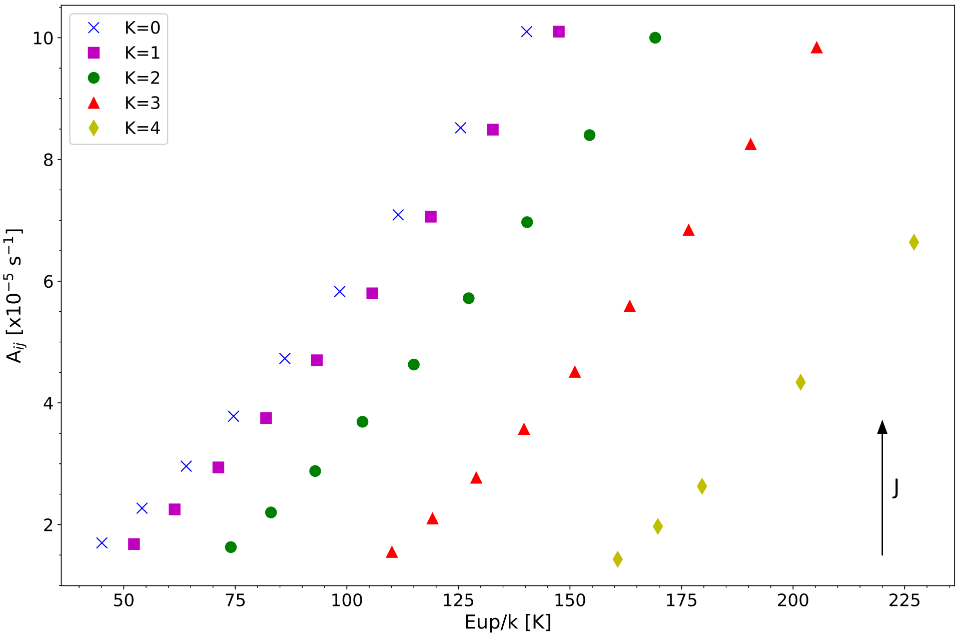

Figure 3.2: Plot of A_{ij} versus E_{up} of the observed CH_3CCH lines. The transitions are grouped according to their K quantum number: blue cross-marks correspond to transitions with K=0, magenta squares correspond to K=1, green circles correspond to K=2, red triangles correspond to K=3 and yellow diamonds correspond to K=4.

Levels within a given K-ladder have similar values of A_{ij}, which increases gradually with J. Moreover, the energy of the upper level also increases with J. Thus, states with higher J quantum numbers require higher energies to be populated, and therefore tend to be associated with warmer regions than the lower J states. Within each K-ladder, transitions with higher K quantum numbers present higher values of E_{up}, which results in the ladder-like spectral profile observed at lower temperatures (for a more detailed discussion see §3.3).

3.2 LTE analyses

3.2.1 Rotational diagrams

In order to estimate the excitation temperature (T_{exc}) and column density (N_{tot}) of CH_3CCH in G331, rotational diagrams were constructed. For a preliminary analysis, we adopted an average source size of 5″, in accordance with previous observations of G331 (Mendoza et al., 2018; Duronea et al., 2019). The rotational diagram of CH_3CCH

constructed under the assumption of optically thin lines is displayed in blue in the upper panel of Figure 3.3. We derived N$_{tot}$(CH$_3$CCH)=(2.4±0.2)×10^{16} cm^{-2} and T$_{exc}$=47.5±1.4 K from the fit (χ^2_{red}=2.95).

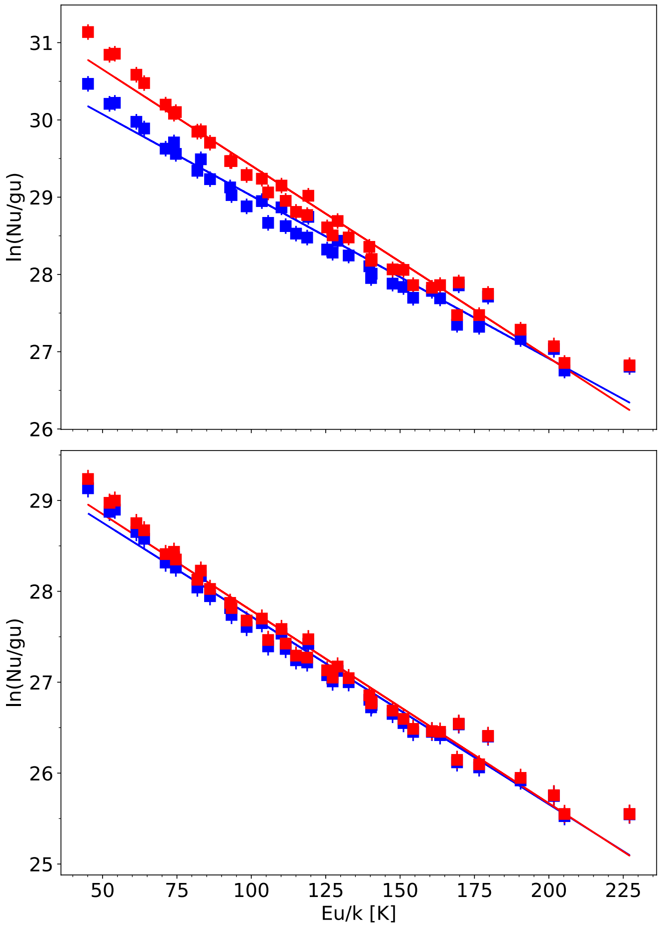

Figure 3.3: Upper panel: Rotational diagram of the CH$_3$CCH lines for a source size of 5″. Least squares fits with and without opacity corrections are shown in red and blue, respectively. *Lower panel:* Same as the upper panel, but for a source size of 10″.

To explore the validity of the optically thin assumption, we estimated the lines' optical depths (τ) using CASSIS. The opacity corrected rotational diagram of CH$_3$CCH is displayed in red in the upper panel of Figure 3.3. From the fit (χ^2_{red}=3.61) we obtained N$_{tot}$(CH$_3$CCH)=(3.9±0.3)×10^{16} cm^{-2} and T$_{exc}$=40.2±1.1 K. This correction leads to a new scaling of the diagram's ordinate axis, resulting in a decrease of 15% and an increase of 62% in the values of T$_{exc}$ and N$_{tot}$, respectively.

Given the rather low temperatures derived from the rotational diagrams (T$_{exc}$ $\sim$ 40 K), the hypothesis of a compact emission arising from a region of 5″ is unlikely. Rather, we infer that the CH$_3$CCH emission is originated from a cooler gas in the outer envelope of

G331, in accordance with other observational works toward star-forming regions (Andron et al., 2018; Hervías-Caimapo et al., 2019; Nagy et al., 2015; Churchwell and Hollis, 1983). Thus, we expect CH_3CCH to trace a more extended region, ranging between $5''$ and $10''$. The rotational diagram constructed for a source size of $10''$ is displayed in the lower panel of Figure 3.3. From the fit under the optically thin assumption (χ^2_{red}=2.33), we derived $N_{tot}(CH_3CCH)=(6.4\pm0.4)\times10^{15}$ cm^{-2} and $T_{exc}=48.4\pm1.3$ K. After including the opacity correction factor, we derived $N_{tot}(CH_3CCH)=(6.9\pm0.5)\times10^{15}$ cm^{-2} and $T_{exc}=47.1\pm1.3$ K from the fit (χ^2_{red}=2.32). For this source size, the contribution of C_τ to the diagram is much less significant than for a more compact emission. Indeed, the corrected fit yielded T_{exc} and N_{tot} values only slightly different from the optically thin scenario, with respective changes of −2.68% and 7.24%. Table 3.2 summarizes the excitation temperatures and column densities derived from the rotational-diagram analysis.

Table 3.2 - Values of T_{exc} and N_{tot} of CH_3CCH toward G331 obtained from the analysis of the rotational diagrams.

Parameter	Source size: $5''$		Source size: $10''$	
	With C_τ	Without C_τ	With C_τ	Without C_τ
T_{exc} [K]	40.2 ± 1.1	47.5 ± 1.4	47.1 ± 1.2	48.4 ± 1.3
N [$\times$ 10^{16} cm^{-2}]	3.9 ± 0.3	2.4 ± 0.2	0.69 ± 0.05	0.64 ± 0.04
χ^2_{red}	3.61	2.95	2.32	2.33

In terms of the reduced χ^2 values, the fit of the $5''$ diagram with opacity corrections was less accurate in comparison with the uncorrected counterpart, whereas no significant change was observed for the $10''$ diagram. This could potentially be due to an overestimation of the lines' optical depths in the compact-emission scenario, in particular for the K=0 and K=1 transitions at lower J values. Indeed, the CH_3CCH emission seems to be optically thin (Churchwell and Hollis, 1983; Fontani et al., 2002), especially for the range of J quantum numbers observed in this work. Thus, the underestimation of the source size is likely being compensated by an overestimation of the opacity—which explains why the opacity correction is almost negligible in the extended-emission scenario. In Figure 3.4, the estimated τs assuming a source size of $10''$ are plotted against the line's upper energy. The more intense lines within a K-ladder, corresponding to K values of 0 and 1, are associated with higher τs, in comparison with the more optically thin K≥2 lines. As E_{up} increases, the optical depth of the K=0,1 transitions show a steep decrease. Moreover, optical depths also decrease with J. Given that $\tau \lesssim 0.2$, it is fair to assume an optically thin emission for

CH_3CCH.

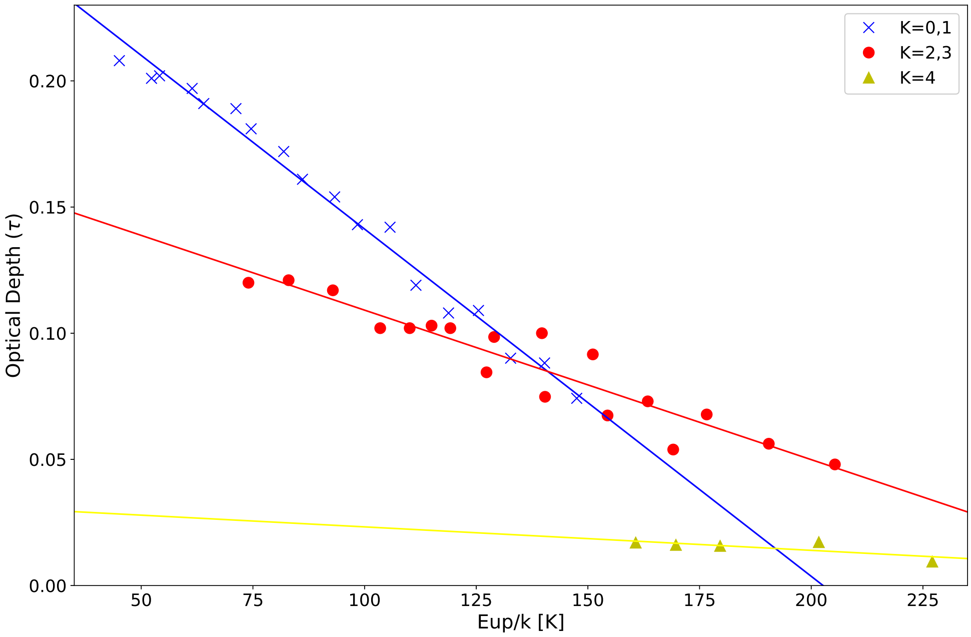

Figure 3.4: Optical depth (τ) vs. E_u of the CH_3CCH lines assuming a source size of 10″. Blue cross marks represent transitions with K=0 and K=1, red circles represent transitions with K=2 and K=3, and yellow triangles represent transitions with K=4. Linear fits to the points are shown for each group of K quantum numbers, to guide the eye.

In both optically-thin and optically-thick scenarios, the 10″ emission yielded better fits than the compact counterpart, which further supports the hypothesis of an extended CH_3CCH emission. Nevertheless, this analysis alone in only conjectural, as interferometry data would be necessary to properly determine the emission size.

3.2.2 Synthetic spectra

The values of T_{exc} and N_{tot} derived from the rotational diagrams were employed to model the emission of CH_3CCH under LTE conditions. We have simulated the spectra considering both 5″ and 10″ scenarios, and including the opacity correction. The modeled and observed spectra of the J=10–9 and J=18–17 K-ladders are shown in Figure 3.5. Overall, the synthetic spectra are in good agreement with the observations, although the accordance is sensibly higher for K-ladders with lower J quantum numbers. Notwithstanding, the opacities of the K=0 and K=1 transitions in the lower K-ladders are clearly overestimated in the scenario of a compact emission—in agreement with our previous discussion.

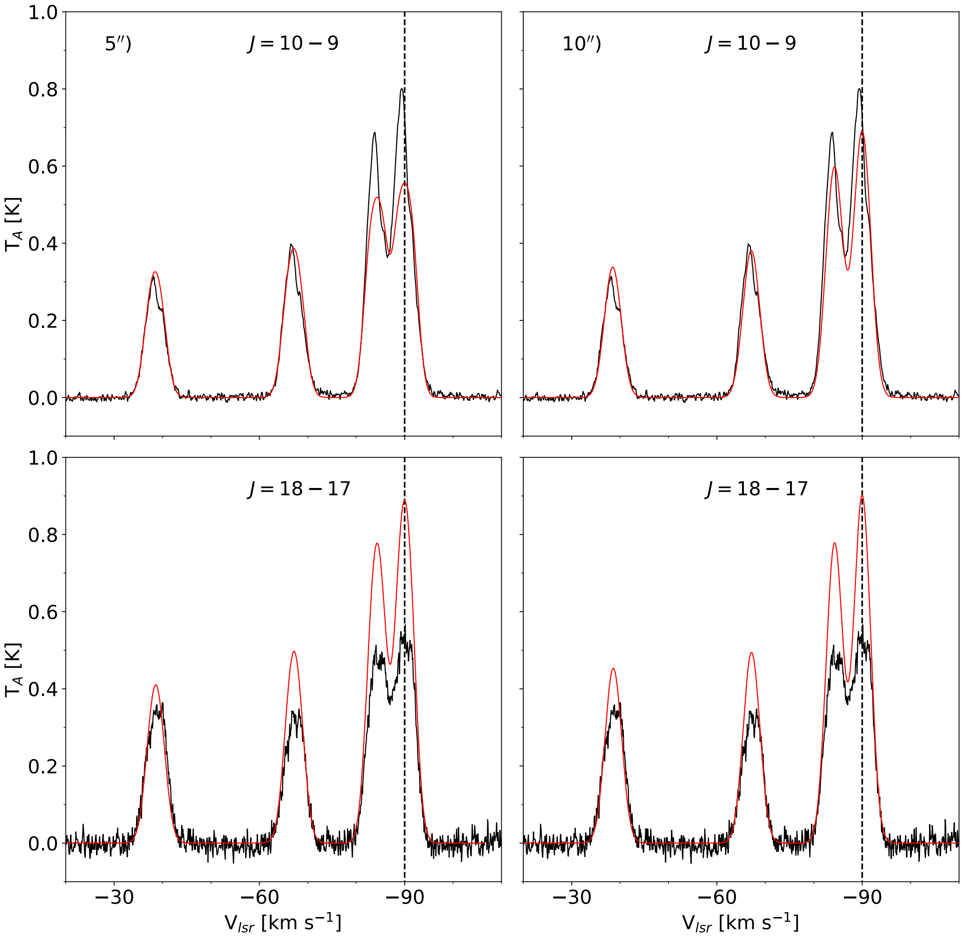

Figure 3.5: Spectra of CH_3CCH observed toward G331. *Upper pannels*: J=10–9, ∼ 170.87–170.91 GHz; *Lower pannels*: J=18–17, ∼ 307.52–307.59 GHz. *Left pannels*: LTE models simulated for a compact emission (5″). *Right pannels*: LTE models simulated for an extended emission (10″). For all panels, the black and red spectra correspond to the observation and the LTE model, respectively. The dashed line indicates the systemic velocity of the source. The abscissas of all spectra were adjusted to the systemic velocity of the K=0 transition.

The gradual decrease in accuracy of the models for higher K-ladders raises suspicion with respect to the LTE assumption. Moreover, the relative intensities of the K=2 and K=3 transitions predicted by the LTE models do not agree with the observations for all frequencies. Although the K=2 lines are predicted to be more intense than the K=3 even at higher frequencies, they are, in fact, observed to be less. Since the population distribution within each K-ladder is dictated by collisions (see §1.7), this behavior implies, *ipso facto*, that the data cannot be described by only one temperature component. This supposition will be addressed further in §3.3. Nonetheless, the synthetic spectra do accurately predict all of the observed CH_3CCH lines to a reasonable extent. In Figure 3.6 we show a superposition of all observed and modeled K-ladders, assuming a source size of 10″ and including opacity corrections. Thus, the CH_3CCH line identifications are thereby definitely confirmed.

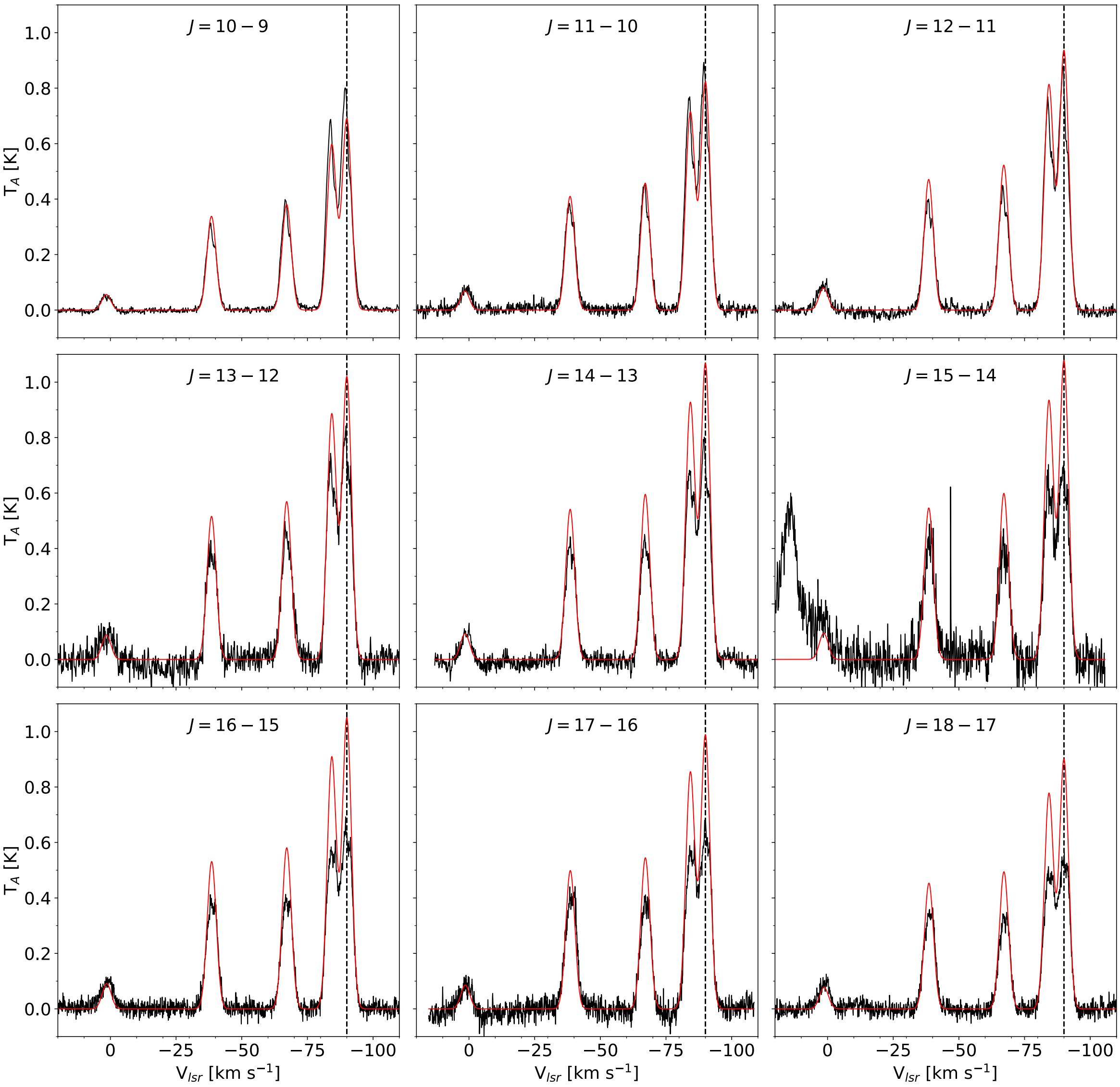

Figure 3.6: Observed spectra of the detected CH_3CCH lines (black), superimposed by the LTE models (red). The dashed line indicates the systemic velocity of the source. The abscissas of all spectra were adjusted to the systemic velocity of the K=0 transition.

3.2.3 CH_3CCH abundance

From its column density, it is possible to infer the abundance of CH_3CCH with respect to H_2. This measure can then be compared to other environments, giving information on the chemical inventory and distribution of the ISM. The abundance of CH_3CCH relative to H_2, X(CH_3CCH), is defined as the ratio of the column densities $N_{tot}(CH_3CCH)/N_{tot}(H_2)$. We have estimated the H_2 column density in G331 from the ALMA measurements of $N_{tot}(H^{13}CO^+)\approx(1.5–3)\times10^{13}$ cm^{-2} (Merello et al., 2013a,b; Hervías-Caimapo et al., 2019), adopting an abundance ratio $N_{tot}(H^{13}CO^+)/N_{tot}(H_2)=3.3\times10^{-11}$, as measured by Blake et al. (1987) in Orion KL. Then, by dividing the estimated CH_3CCH column density (in the extended-emission and optically-corrected scenarios) by the inferred $N_{tot}(H_2)$, we obtained a ratio of X(CH_3CCH)$\approx(1.5–7.6)\times10^{-8}$. Giannetti et al. (2017) have derived similar methyl acetylene abundances, X(CH_3CCH)$\approx(0.5–2.8)\times10^{-8}$, for a statistically significant sample of massive clumps with temperatures ranging from ∼20 to ∼60 K. This value is roughly one order of magnitude higher than the CH_3CCH abundance in Sgr B2 (Churchwell and Hollis, 1983). For further comparison, Table 3.3 lists the CH_3CCH abundances observed toward three massive star-forming regions (G12.89+0.49, G16.86-2.16 and G28.28-0.36)—in addition to G331—as well as toward a low-mass star-forming core (L1527).

Table 3.3 - Abundances of CH_3CCH observed toward high- and low-mass star-forming sites. [a] From Taniguchi et al. (2019).

Source	Abundance
G12.89+0.49	$2.1^{+1.4}_{-1.1}\times10^{-8}$ [a]
G16.86-2.16	$1.6^{+0.95}_{-0.75}\times10^{-8}$ [a]
G28.28-0.36	$3.8^{+2.6}_{-2.2}\times10^{-8}$ [a]
L1527	$(1.07\pm0.05)\times10^{-9}$ [a]
G331	$(1.5–7.6)\times10^{-8}$

Although the estimated abundance of CH_3CCH shows good agreement with other observational works conducted toward similar sources, there is a caveat to our approach. The $N_{tot}(H^{13}CO^+)$ column density derived for G331 was confined in a region of $\leq5''$, which is much more compact than the expected CH_3CCH emitting region. As a result, the inferred $N_{tot}(H_2)$ and X(CH_3CCH) are only approximations, with the former and the latter potentially being under- and overestimated, respectively.

3.3 Intensity inversion

3.3.1 Rotational-spectrum simulations

The relative intensities of the lines within a given K-ladder are dictated by collisions, and thus will change depending on the temperature of the environment. For this reason, symmetric rotors act as excellent temperature probes, as was mentioned before. In particular, our observations of CH_3CCH toward G331 show an unexpected behavior of the K-ladder profiles for different J transitions, which motivated us to explore this temperature dependence in a molecular level. Accordingly, we simulated the rotational spectra of CH_3CCH at temperatures ranging from 10 K to 100 K, with 10 K steps, by means of the PGOPHER general purpose software (Western, 2017). The rotational constants (A and B), the quartic and sextic centrifugal distortion constants (D_J, D_{JK}, H_J, H_{JK} and H_{KJ}), and the dipole moment (μ) employed in the simulations are listed in Table 3.4.

Table 3.4 - Spectroscopic parameters employed in the spectrum simulations. The experimental measurements of the B rotational constant and the centrifugal distortion constants were obtained from Dubrulle et al. (1978). The dipole moment was measured by Muenter and Laurie (1966). Since the A rotational constant cannot be determined directly from the measured spectra, the estimated constant from the JPL database was used.

Parameter	Value	Parameter	Value
A [MHz]	158590	H_J [Hz]	0.0097
B [MHz]	8545.87712	H_{JK} [Hz]	0.935
D_J [kHz]	2.9423	H_{KJ} [Hz]	5.23
D_{JK} [kHz]	163.423	μ [D]	0.75

The transitions' intensities are given by Equation 2.10, which is normalized to the partition function given in Equation 2.11. The rotational energies are calculated from Equation 2.9. For validation purposes, the CH_3CCH rotational spectrum was also simulated at 300 K, with J_u values up to 79. In Figure 3.7, we present the spectrum at 300 K together with the experimental counterpart, measured at the same temperature. The predicted frequencies were very close to experiment, with an average error of $\sim$1.2 MHz for $J_u \leq 30$ and $K \leq 4$, which corresponds to frequencies up to $\sim$500 GHz. The relative intensities of the transitions within each K-ladder also show a very good agreement between the simulated and experimental spectra (see the inset in Figure 3.7). Thus, this approach can be considered a reliable source of information on the temperature dependence of the K-ladder spectral profile.

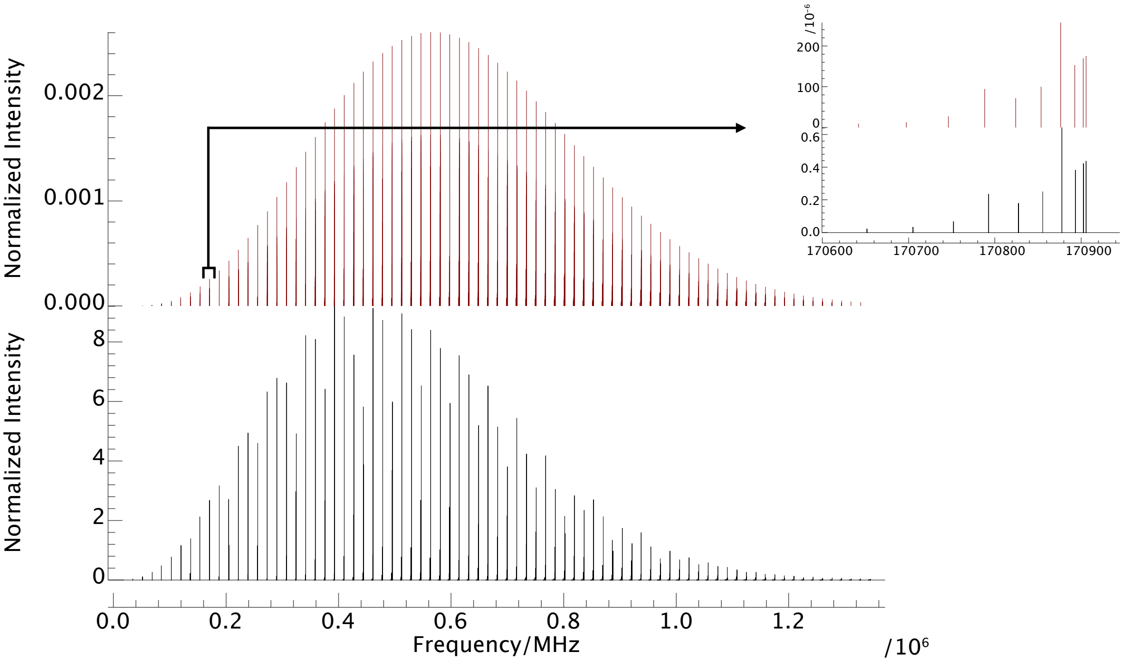

Figure 3.7: Experimental (red, upper panel) and simulated (black, lower panel) pure rotational spectra of CH_3CCH at 300 K. The inset shows the J=10–9 K-ladder.

The J=10–9 K-ladders of CH_3CCH simulated at 10, 40, 70 and 100K are displayed in Figure 3.8. Moreover, in Figure 3.9, we plot the intensity ratios I[K=n]/I[K=0] of the predicted lines within a K-ladder versus the temperature, with n=1, 2 and 3. We show the results for the J=10–9 and J=18–17 transitions, corresponding to the extremities of the observed bandwidth. As seen in the plot, the behavior of the intensity ratios are overall analogous for the range of J values explored in this work.

As speculated in the previous sections, an interesting phenomenon is evinced by Figures 3.8 and 3.9. At low temperatures, the spectrum is dominated by the K=0 transitions, with small contributions from the other K levels. As the temperature rises, however, the ratios of all K transitions increase at different rates. The intensity ratios of both K=1 and K=2 transitions, compared to K=0, follow a similar trend: they show an initial stage of rapid growth, which becomes gradually slower as the temperature continues to rise. As can be seen for the K=1 transitions, the curve will eventually reach a plateau, which stabilizes the K=1/K=0 intensity ratios at values around 0.8–0.9. Comparatively, the ratios for K=3 present a more dramatic increase. At around 50 K, the K=3 lines become more intense than the K=2 transitions. Further, at around 100 K, their intensities surpass those of the K=1 transitions. At even higher temperatures, they ultimately become the most intense

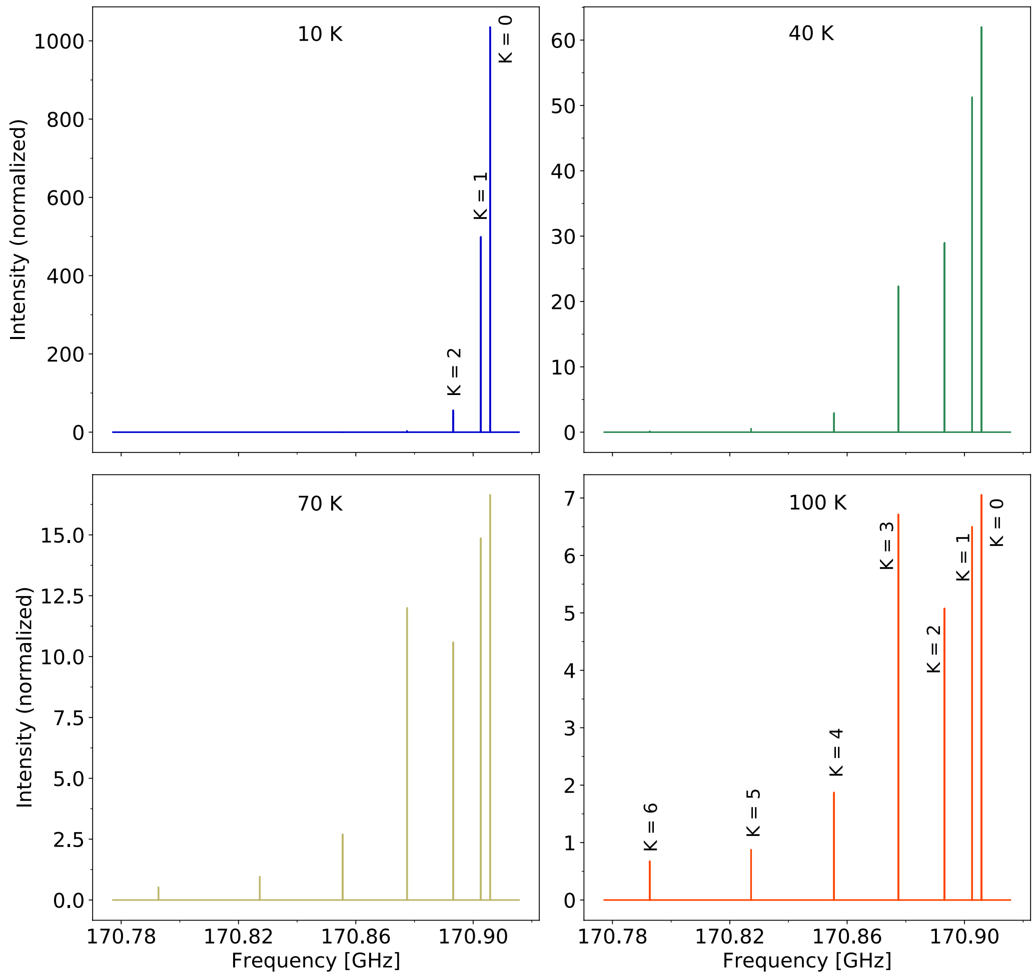

Figure 3.8: J=10_K–9_K K-ladder of CH_3CCH simulated at 10 K (upper-left panel), 40 K (upper-right panel), 70 K (lower-left panel) and 100 K (lower-right panel).

line of the given K-ladder.

This behavior can be explained by nuclear spin statistics. Symmetric tops with three equivalent hydrogens, such as CH_3CCH (see Figure 1.10), have two different spin symmetries—namely, A and E. The A states correlate with the transitions with K=0, 3, 6, 9, 12..., whereas the E states correspond to the remaining transitions, and the states have relative statistical weights of $A : E = 2 : 1$ (Herzberg, 1945). As a result, the population distribution and therefore the relative intensities of the transitions at higher temperatures will favor the states with higher degeneracies, while, at lower temperatures, the energy acts as a limiting factor. For this reason, the K=3 transition, which corresponds to a doubly-degenerate A state, rapidly increases in intensity as the temperature rises—eventually becoming the most intense line in a given K-ladder. This phenomenon is similar to the temperature-dependent abundance ratio of ortho/para hydrogen, and makes

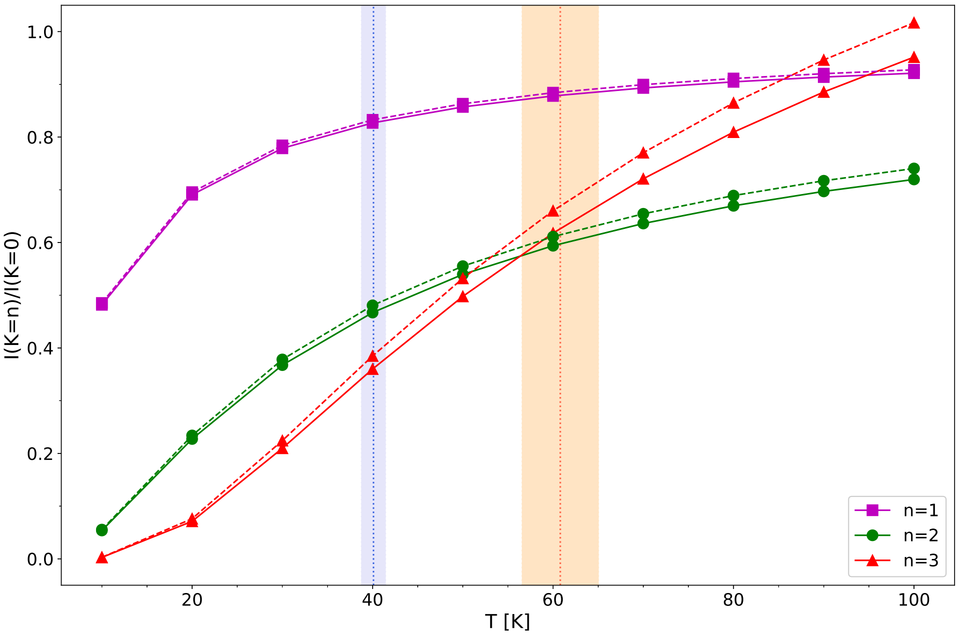

Figure 3.9: Intensity ratios I[K=n]/I[K=0] versus temperature for transitions within a given K-ladder. Purple squares represent ratios with $n = 1$, green circles represent ratios with $n = 2$, and red triangles represent ratios with $n = 3$. Solid and dashed lines correspond to, respectively, the J=10–9 and J=18–17 K-ladders. The red and blue regions are discussed in §3.3.4.

the CH_3CCH K-ladder profile highly sensitive to the local temperature, in particular with regards to the relative intensities of the K=3 transitions.

3.3.2 Inversion in the observed spectra

As can be seen in Figure 3.1, we serendipitously observed a frequency window in which the CH_3CCH K-ladder profiles gradually change as a function of the rotational quantum number. For low J values, which are associated with cooler regions, the K=2 lines are more intense than the K=3. However, as we observe transitions with higher J values, which are consequently associated with warmer regions, the K=2/K=3 intensity ratios consistently decrease. From J=15–14 onward, the K=3 lines become more intense than the K=2. This gradual inversion can be easily inferred by visual inspection, as is clearly shown in Figure 3.10.

In order to quantify this inversion, we have plotted the K=2/K=3 ratios of the observed areas listed in Table 3.1 as a function of the upper J value (Figure 3.11). To evaluate

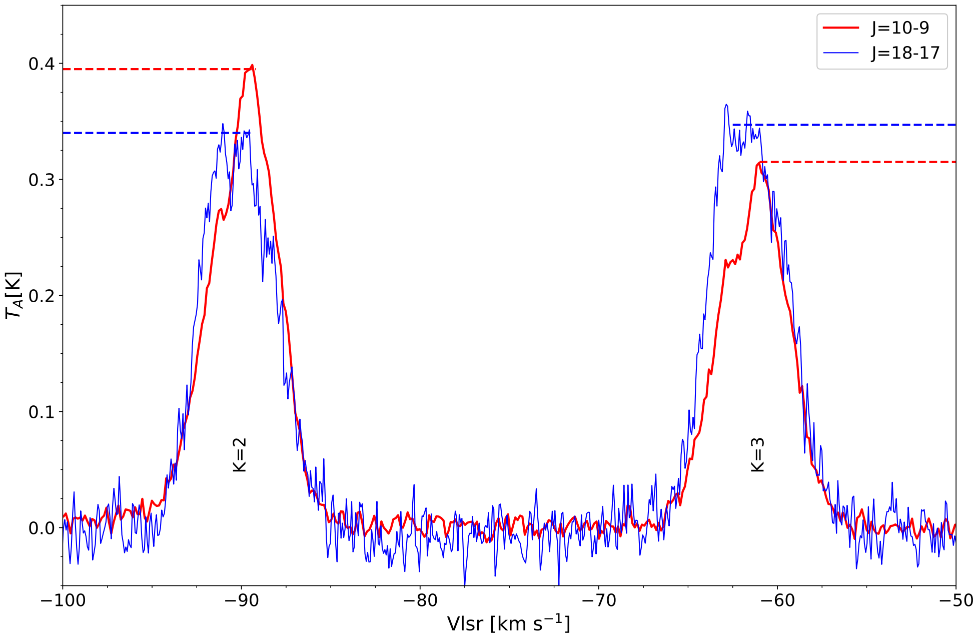

Figure 3.10: Superposition of the K=2 and K=3 lines of the J=10–9 (red) and K=18–17 (blue) K-ladders, evincing the intensity inversion of the peaks. The abscissa is adjusted to the systemic velocity of the K=2 lines.

the strength of the correlation seen in the plot, we have derived its Pearson correlation coefficient (r), which is calculated as the covariance of the two variables divided by the product of their standard deviation. Hence, this test calculates the normalized covariance of two variables, yielding a coefficient with values ranging from -1 to 1. The -1 and 1 limits correspond, respectively, to perfectly-linear negative and positive correlations. The $r = 0$ result corresponds to no correlation. A value of $r \geq |0.5|$ indicates a noticeable correlation, and $r \geq |0.8|$ is considered a strong correlation.

This plot of Figure 3.11 yields a Pearson correlation coefficient of r=-0.84, which, given the small FWHM dispersion of the observed lines, clearly indicates a decreasing trend of the K=2/K=3 intensity ratios with J. This result strongly suggests that the lines are tracing a region with a temperature gradient, which explains the loss in accuracy of the synthetic LTE spectra for higher J transitions (see §3.2.2).

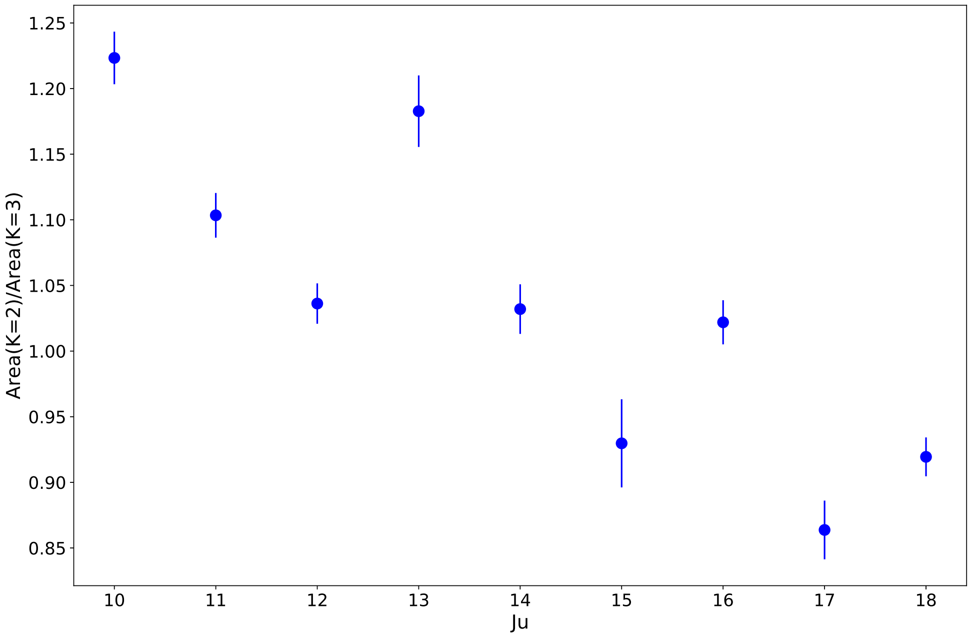

Figure 3.11: Ratios of the areas for K=2 and K=3 lines versus the upper J value of the transition. Areas and uncertainties were obtained through gaussian fittings of the observed data using CLASS.

3.3.3 Modified rotational diagrams

The rotational-diagram analysis described in §1.6 works under the assumption of an isothermal gas in LTE. In such cases, there will be a linear correlation between ln N_u and E_{up}. However, in a scenario where the lines cannot be characterized by only one temperature component, the rotational diagram will deviate from the linear trend. Mauersberger et al. (1988) have explored the case of a spherically symmetric cloud in which the temperature has a power-law dependence on the distance from the center, and demonstrated that, in those circumstances, there should be a linear correlation between ln N_u and ln E_{up}. Fontani et al. (2002) have applied this reasoning to investigate the temperature profile toward 12 ultracompact HII regions. They constructed “modified”rotational diagrams—namely, ln N_u versus ln E_{up}—with observations of three CH_3CCH K-ladders. Based on the quality of their linear fits, they concluded that the emission should originate from roughly isothermal regions.

To further investigate the hypothesis of a temperature gradient to describe the observed CH_3CCH emission in G331, we have plotted modified rotational diagrams for both 5″ and

10″ source sizes. We also consider both optically thin and opacity corrected scenarios. The modified diagrams are shown in Figure 3.12. A comparison between the χ^2_{red} values of the linear fits of both the traditional and the modified rotational diagrams is presented in Table 3.5.

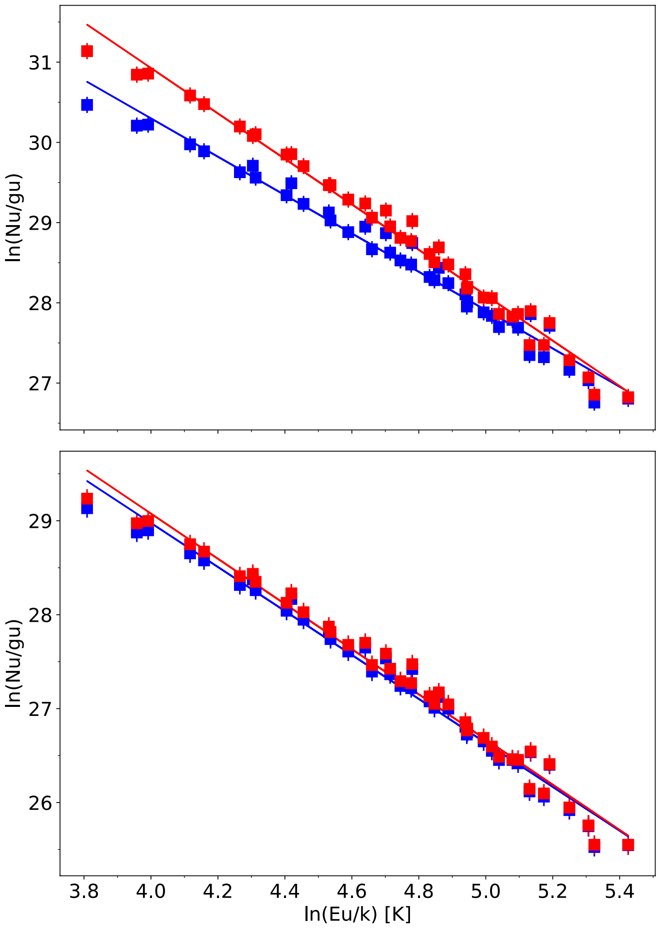

Figure 3.12: Upper panel: Modified rotational diagram of the CH_3CCH lines for a source size of 5″. Least squares fits with and without opacity corrections are shown in red and blue, respectively. *Lower panel:* Same as the upper panel, but assuming a source size of 10″.

Table 3.5 - Values of χ^2_{red} obtained from the least square fits of the traditional and modified rotational diagrams.

Source size (″)	Opacity correction	χ^2_{red} Traditional diagram	χ^2_{red} Modified diagram
5	With C_τ	3.61	1.83
	Without C_τ	2.95	2.26
10	With C_τ	2.32	1.79
	Without C_τ	2.33	1.85

For all the explored situations, the linear fits of the modified rotational diagrams were consistently better than the traditional counterparts, favoring the hypothesis of an emission with a non-negligible temperature gradient.

3.3.4 Quantifying the temperature gradient

At this point, the supposition of a temperature gradient is deemed fairly substantiated by the amount of evidence presented in the previous subsections. Thus, for the next step, we estimated the extent of the temperature profile by grouping the points in the rotational diagram into two subsets (Figure 3.13). The groups were separated at E_{up} ≈125 K, according to the behavior of the observed K=2 and K=3 intensity ratios. The lower-energy group contains all K=2 transitions with J≤14, for which K=2/K=3≥1. Contrarily, the higher-energy subset encompasses all K=2 transitions with J¿14, for which K=2/K=3¡1. The resulting T_{exc} and N_{tot} obtained from the linear fit of each subset are listed in Table 3.6.

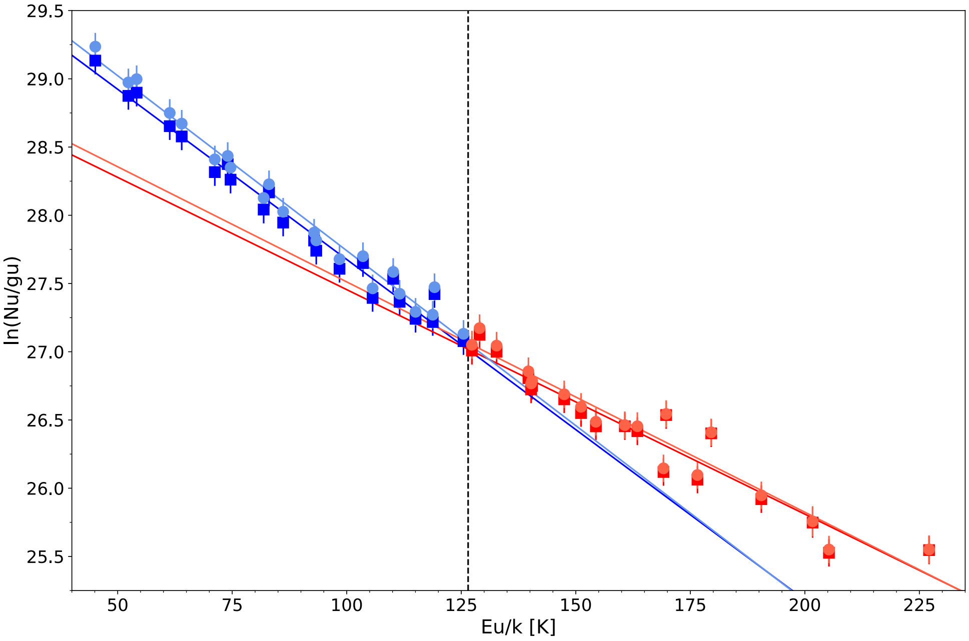

Figure 3.13: rotational diagram of the CH_3CCH lines for a source size of 10″. The points were divided into two subsets indicated by the dashed line. The points pertaining to the low- and high-energy subsets are shown in blue and red, respectively. Least squares fits to the points within each subset are shown. Circles and squares correspond to the lines with and without opacity corrections, respectively.

Assuming an optically thick scenario, the rotational diagram divided into two subsets yields temperature components of ∼40 and ∼60 K. Although the points in the rotational diagram show an overall fairly linear trend, the T_{exc} obtained from this analysis is highly

Table 3.6 - Values of T_{exc} and N_{tot} of CH_3CCH obtained from the 2-component rotational diagrams for a source size of 10″.

Parameter	Lower-energy comp. (blue)		Higher-energy comp. (red)	
	With C_τ	Without C_τ	With C_τ	Without C_τ
T_{exc} [K]	39.0 ± 1.2	40.1 ± 1.3	59.3 ± 3.9	60.8 ± 4.2
N [$\times$ 10^{15} cm^{-2}]	7.5 ± 0.5	6.9 ± 0.5	4.8 ± 0.9	4.5 ± 0.8
χ^2_{red}	0.72	0.78	1.62	1.74

sensitive to the fitted slope. Consequently, a difference of around 20 K arises between the values derived from the linear fittings of the two subsets. This temperature interval coincides with the region of Figure 3.9 where the intensity inversion of K=2 and K=3 occurs. Thus, one can regard the two temperature components extracted from the blue and red subsets in Figure 3.13 as, respectively, lower and upper limits to the temperature profile of the observed emitting region—indicated as the blue and red regions in Figure 3.9. Not coincidentally, the rotational diagram analysis of §3.2.1 yielded an averaged temperature of T_{exc} ~50 K, which corresponds approximately to the threshold where the intensity inversion of the K=2 and K=3 lines happens for the observed J transitions. The rotational diagram is an averaged approach, and therefore is suited to evaluate the large-scale emission of CH_3CCH. The intrinsic spectroscopic properties of methyl acetylene, however, enable a more direct and meticulous assessment of the temperature of the source, giving information beyond the limitations of the rotational diagram. The same discussion is valid for the optically thin scenario.

The synthetic spectra under the LTE assumption shown in Figure 3.5 reproduces more accurately the observed data for lower J quantum numbers. This gradual loss in accuracy for higher J transitions is likely a consequence of the intensity inversion that occurs around J_u=14 toward G331 (see Figure 3.11). Indeed, throughout the entire ~170840–307600 MHz frequency range, modeled transitions with K=3 are less intense than the K=2 counterparts, as shown in Figure 3.6. Since our observations cannot be accurately described by only one temperature component, the model will be increasingly amiss as the bulk of the emission transitions to regions with different average gas temperatures than the T_{exc} derived from the rotational diagram. Hence, our LTE model seems to best describe the cooler environment, traced by the lines with lower J values. Ergo, the rotational diagram is apparently biased toward the lower-temperature gas.

Previously, Hervías-Caimapo et al. (2019) have used ALMA to observe four CH_3CCH lines within the J=21–20 K-ladder toward G331, which showed a peak of emission located at a radius of $\sim$1.2″. From the rotational diagram constructed with the CH_3CCH lines, they obtained an excitation temperature of T_{exc} = 70±7 K. Their results are in accordance with our hypothesis of a temperature gradient, which indeed predicts that transitions with higher J quantum numbers will be associated with higher excitation temperatures and more compact regions.

3.4 Kinematics

3.4.1 Velocity vs. frequency

The transitions' spectroscopic parameters (see Table 3.1), obtained through fitting a Gaussian profile to each line, are directly related to the kinematics of the emitting region—or, at least, of the gas where the bulk of the emission is coming from. By examining the line shape variation as a function of the excitation energy, one can gather information on the small-scale structure of the source even with low-angular-resolution data. In Figure 3.14, we show plots of the peak velocities of the lines versus their frequencies. For the sake of clarity, each K transition was plotted separately. Since they are fainter and harder to observe, the K=4 transitions were not included in this analysis.

In all of the plots, the lines' peak velocities are strongly negatively correlated with frequency, with Pearson coefficients of r=-0.93, -0.94, -0.94 and -0.88 for, respectively, K=0, K=1, K=2 and K=3. Moreover, the mean velocity shift between lines with the same K quantum number within the J=10–9 and J=18–17 K-ladders is $\sim$0.49 km s^{-1}, which is almost twice the poorest obtained velocity resolution (see §2.2). Those numbers bolster the claim that the CH_3CCH lines with higher excitation energies, and therefore higher frequencies, are tracing regions with slightly different physical conditions. The lines associated with colder regions (i.e., with lower frequencies) are characterized by more redshifted velocities, whereas warmer regions seem to be systematically blueshifted.

3.4.2 FWHM vs. frequency

To inspect the line width as a function of the transition energy, we plotted the lines' FWHMs versus their rest frequencies (Figure 3.15). Again, different K transitions are

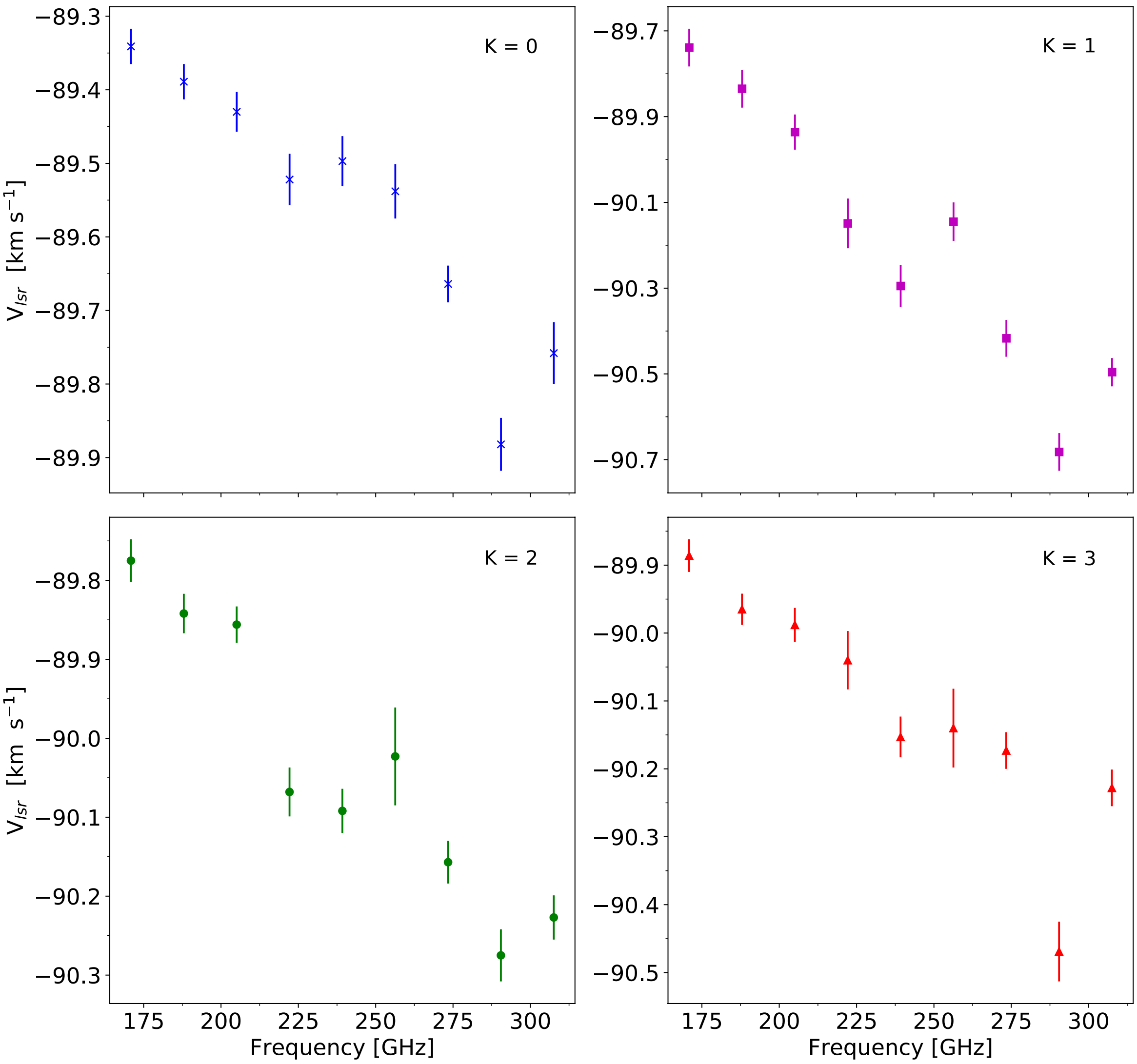

Figure 3.14: Peak velocities versus line frequency obtained from gaussian fittings to the CH_3CCH lines. Each plot contains only transitions with the same K quantum number.

plotted separately, and the K=4 lines were not included in the analysis. From the plot, it is clear that the FWHM is correlated to the line frequency, with r=0.98, 0.88, 0.77 and 0.67 for K=0, K=1, K=2 and K=3. The K=0 lines show a particularly strong correlation, which presents a quasi-linear trend. This relationship implies that warmer regions are associated with broader lines.

The increase in FWHM for transitions with higher frequencies cannot be explained by thermal broadening, since its effects are negligible for radio lines. The contribution to the FWHM due to thermal broadening is calculated by (Draine, 2011):

$$FWHM = 2\sqrt{\ln 2}b \tag{3.1}$$

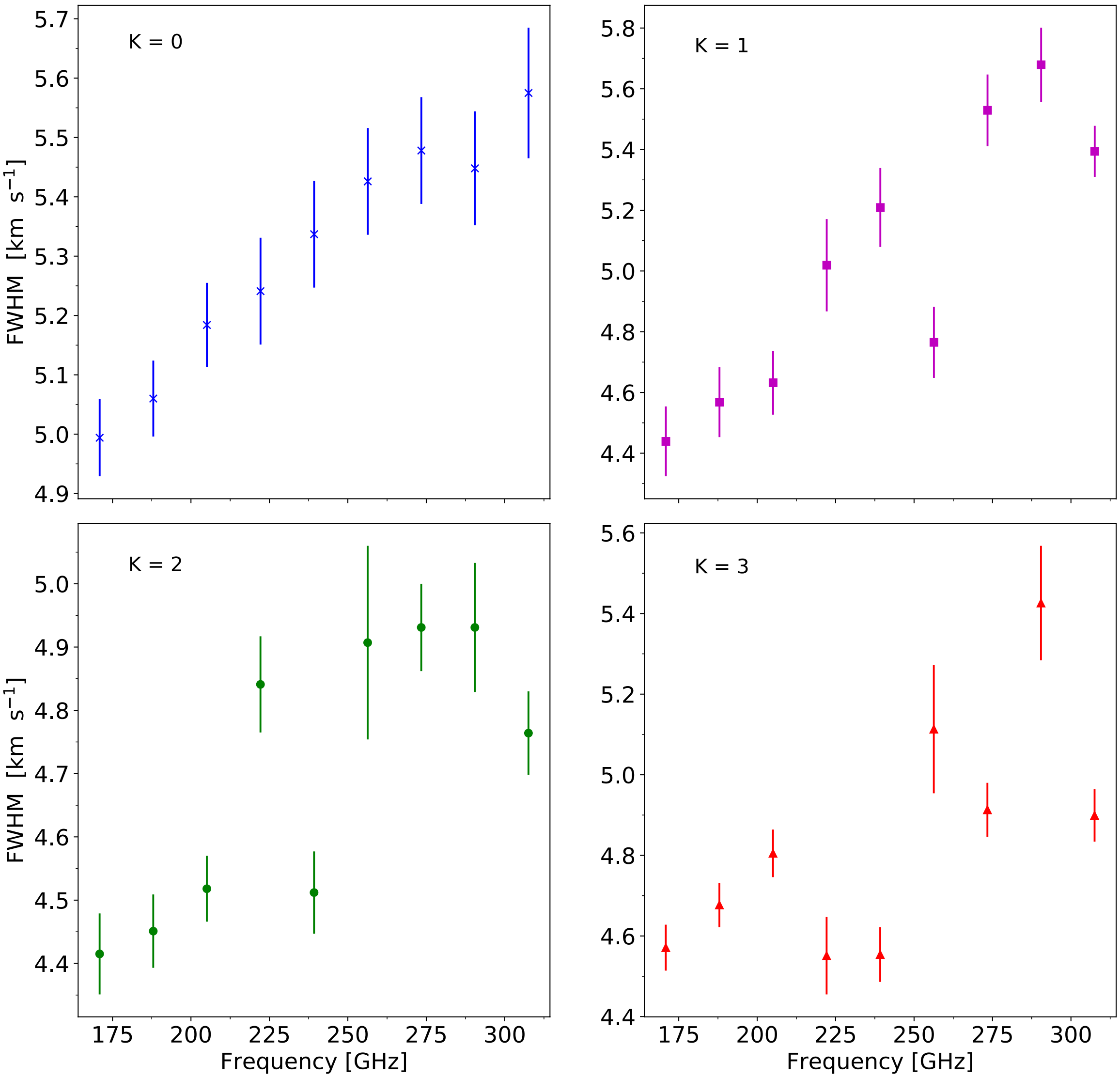

Figure 3.15: Line widths vs. rest frequencies obtained from gaussian fittings of the observed transitions. Each subplot contains only transitions with the same K quantum number

in which

$$b = \sqrt{\frac{2kT}{m}} \tag{3.2}$$

As discussed in §3.3.4, the gas where the bulk of the CH_3CCH emission originates is believed to present a temperature profile with lower and upper limits of, respectively, ~40 and ~60 K. At such temperatures, the contribution to the CH_3CCH line width from thermal broadening is of ~0.21 and ~0.26 km s^{-1}, respectively, which corresponds to a variation of ~1.25% of the line widths, assuming a FWHM of ~4 km s^{-1}. This contribution is ten times smaller than the average FWHM variation between the J=10–9 and J=18–17 lines with the same K quantum number.

Instead, the line broadening is likely to be caused by turbulence effects. In other words, the broader widths associated with higher J values indicate that the gas where the bulk of the emission arises from must become gradually more turbulent as the temperature increases. This is a fairly reasonable suggestion, considering that the warmer emission comes from the inner parts of the envelope surrounding the MYSO. A similar reasoning is discussed by Fontani et al. (2002), who observed lines of CH_3CCH toward 12 UC HII regions and also found a positive correlation between their widths and frequencies.

3.4.3 FWHM vs. velocity

In the previous subsections, we demonstrated that both the line widths and peak velocities of the observed CH_3CCH transitions correlate with their frequencies, giving information on the small-scale structure of G331. Now, we investigate the correlation between those two parameters. In Figure 3.16, we present a plot of the widths and peak velocities of the observed lines, which are listed in Table 3.1.

The line widths and peak velocities of transitions with the same K quantum number are overall strongly correlated. Indeed, the Pearson correlation coefficient of the K=0, K=1, K=2 and K=3 groups are, respectively, r=-0.85, r=-0.97, r=-0.78, and r=-0.80. As for the previous subsections, the lines with K=4 were not included in the comparison. Their smaller signal-to-noise ratios hampers their spectroscopic fittings, which is reflected in their higher associated uncertainties reported in Table 3.1. Nonetheless, for each plotted K group, there is a clear tendency for broader lines to present increasingly blueshifted velocities, as would be expected considering the results of §3.4.1 and §3.4.2. The same trend was also observed by Di Francesco et al. (2004) with N_2H^+ lines toward the Ophiuchus A star-forming core.

Interestingly, the K=0 lines are systematically broader and less blueshifted than the other groups, indicating that they might be tracing a slightly different region than the bulk of the emission of the other K transitions. To properly interpret this feature, observations with higher angular resolution are essential, but currently unavailable. Therefore, we can only provide a speculative discussion on a possible explanation to this plot: at low temperatures, the contributions from transitions with $K\neq0$ to the rotational spectrum of CH_3CCH are minor, and the emission is dominated by the K=0 lines (see Figures 3.8 and

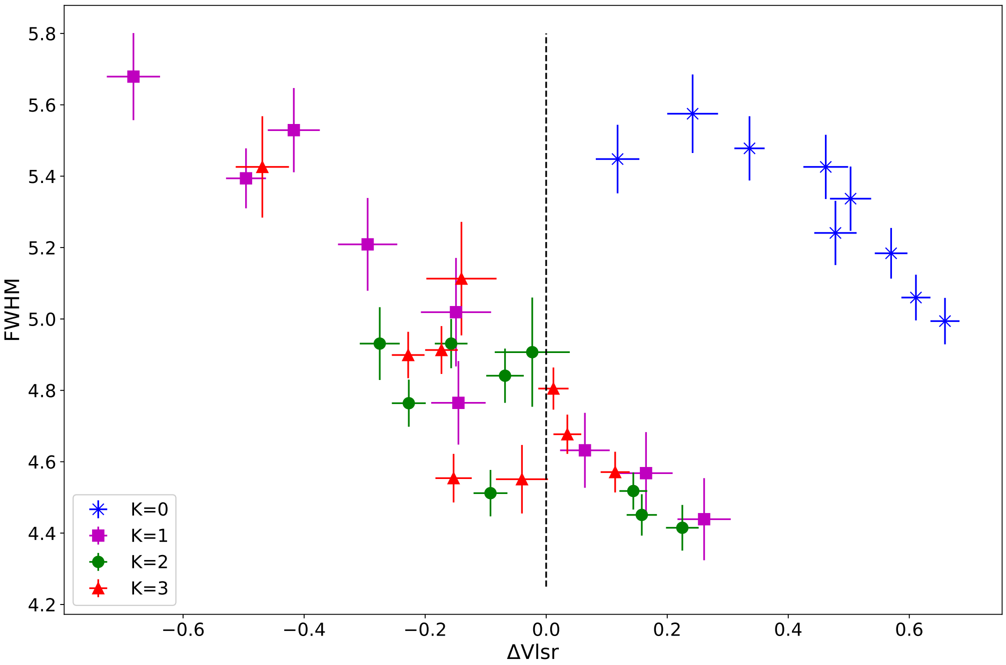

Figure 3.16: Line widths vs. peak velocities obtained from gaussian fittings of the observed transitions. Blue cross marks represent transitions with K=0, purple squares represent transitions with K=1, green circles represent transitions with K=2 and red triangles represent transitions with K=3. The black dashed line separates the blue- and red-shifted regions of the plot. G331 has a systemic velocity of -90 km s^{-1}.

3.9). As the temperature rises, however, the relative intensities of the K≠0 transitions rapidly increase, resulting in richer K-ladders. Thus, it is likely that the bulk of the K=0 emission is originated from a cooler and more extended region, which does not contribute as significantly to the lines with K≠0. These, in turn, must be tracing a hotter and more compact environment, resulting in a different kinematic signature. The systematic redshift of the peak velocities for the K=0 lines compared the other groups also suggests interesting velocity features of the cold component.

In Figure 3.17, we illustrate the variation in the line widths and peak velocities by plotting the K=0 and K=1 transitions of the J=10–9 and J=18–17 K-ladders. The gaussian fittings show that lines with higher frequencies are broader, and the dash-dotted lines evince the negative correlation of the peak velocities with frequency. Further surveys of the CH_3CCH emission toward G331 with higher angular resolution are therefore imperative to better understand the different gas components it might be tracing, as well as the “microphysics”of the hot core.

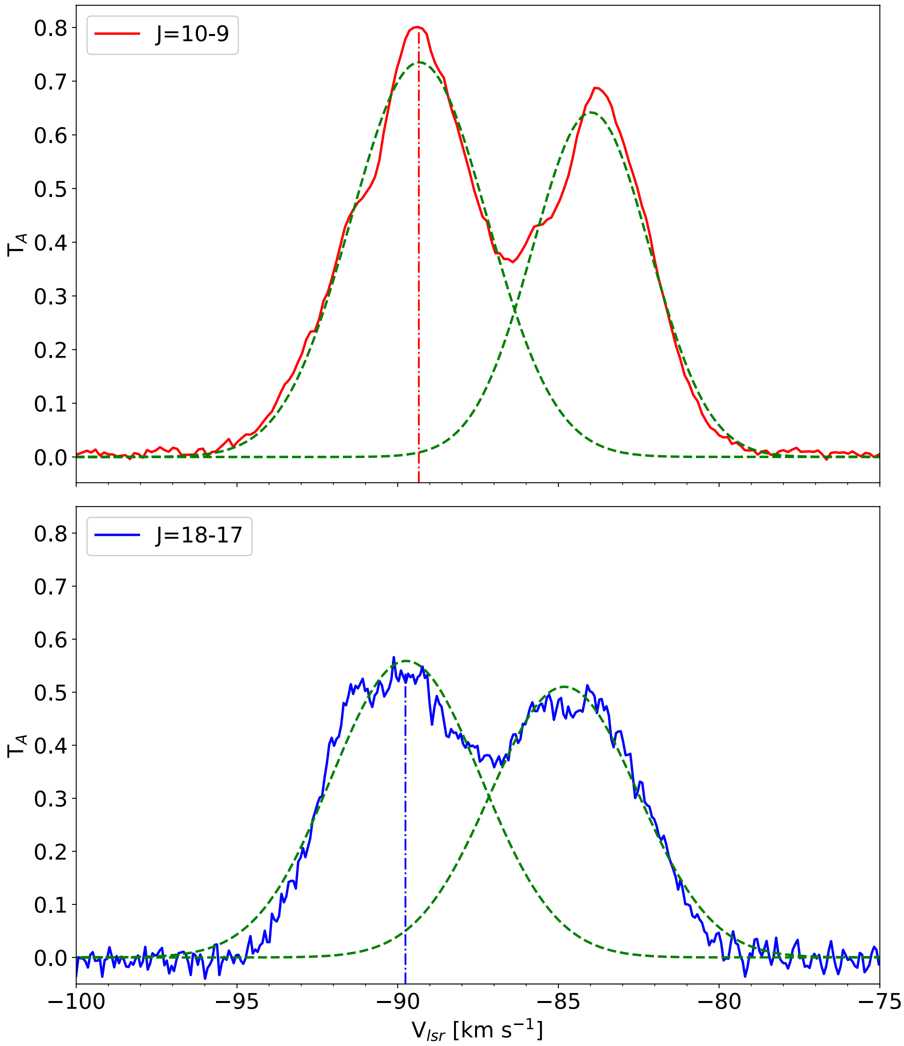

Figure 3.17: Top pannel: Spectrum of G331 showing the 10_0–9_0 and 10_1–9_1 transitions of CH_3CCH in solid red line. Dashed green lines are the Gaussian profile fittings. The red dash-dot line indicates the peak velocity of the 10_0–9_0 transition. *Bottom pannel:* Same as the top pannel, but for the 18_0–17_0 and 18_1–17_1 transitions—in blue instead of red.

Chapter 4

Conclusions and future perspectives

4.1 Conclusions

In the present master's thesis, we have conducted a spectral survey of methyl acetylene (CH_3CCH) toward the Hot Molecular Core G331.512–0.103, using the APEX 12m telescope. We observed a total of 41 clear lines of CH_3CCH above the detection limit of 3σ, without any contamination. To the best of our knowledge, the number of different lines of CH_3CCH detected in this work was unprecedented, making this project the first spectral survey of methyl acetylene, and resulting in interesting insights on the physics of the source.

To investigate the excitation conditions of the CH_3CCH emission and their implications on the physical properties of G331, we constructed rotational diagrams using all of the 41 detected lines. This analysis allows to estimate the excitation temperature (T_{exc}) and total column density (N_{tot}) of the species under consideration, provided that the emission is under Local Thermodynamic Equilibrium (LTE). Since the observations were performed with a single-dish facility, the source size cannot be directly inferred from our data. Nonetheless, we explored both possible limiting scenarios of a compact ($\sim5''$) or an extended ($\sim10''$) emission. Opacity corrections were also considered in this analysis.

Synthetic LTE spectra of CH_3CCH were constructed based on the values of T_{exc} and N_{tot} derived from the rotational diagrams. Moreover, pure rotational spectra of CH_3CCH were simulated at a wide range of temperatures, in order to investigate the temperature dependence of the K-ladders' spectral profile. Adaptations of the rotational diagram technique, including modified diagrams and multiple-component fittings, were employed to scrutinize the temperature profile of the source. Finally, spectroscopic properties derived from fitting single gaussian profiles to the lines were used to explore the kinematics of the emitting gas. This approach is common for single-dish observations, which lack the angular resolution to directly study the small-scale structure of the source.

The main findings and conclusions achieved by virtue of the aforementioned procedures are listed below:

- From the rotational diagram analysis, we estimated an excitation temperature of T_{exc}= 40.2±1.1 K and a total column density of N_{tot}=$(3.9\pm0.3)\times10^{16}$ cm^{-2} for a compact source, including opacity corrections. Comparatively, we derived T_{exc}=47.1±1.2 K and N_{tot}=$(6.9\pm0.5)\times10^{15}$ cm^{-2} for an extended emission. Those values of T_{exc} indicate that the bulk of the CH_3CCH emission is originated from a cool gas, which is in accordance with other observational works and is inconsistent with a source size of $\sim5''$. Thus, we additionally infer that the emission should encompass an extended region.

- Adopting the N_{tot} value of CH_3CCH estimated for a source size of $\sim10''$, and assuming an H_2 column density of $\sim(4.5–9.1)\times10^{23}$ cm^{-2}, we derived a CH_3CCH abundance of $X(CH_3CCH)=N_{tot}(CH_3CCH)/N_{tot}(H_2)\sim(1.5–7.6)\times10^{-8}$. This value agrees with other observational works of CH_3CCH toward star-forming regions.

- The synthetic LTE spectra based on the T_{exc} and N_{tot} values derived from the rotational diagrams become gradually less accurate for higher frequency transitions. Moreover, the K=2/K=3 line intensity ratios of transitions within a given K-ladder are strongly negatively correlated with J_u, which is not predicted by the LTE models. Those observations firmly imply that the emission cannot be described by only one temperature component. Rather, we suggest that it is arising from a region with a temperature profile. Modified rotational diagrams with the abscissa plotted in logarithmic scale yield a better fit than the traditional diagram, which reinforces the hypothesis of a non-isothermal emission. Additionally, an analysis of the rotational diagram separated into two subsections provides upper and lower limits of, respectively, ∼60 and ∼40 K for the temperature gradient. This approach enables us to assess the small-scale structure of the source with data from single-dish facilities, further broadening the temperature-probing capabilities of symmetric tops with three equivalent hydrogens—such as CH_3CCH. For a thorough analysis of the temperature profile of the source, however, it is imperative to observe a wide range of CH_3CCH lines with high angular resolution, by means of interferometry instruments such as ALMA.

- The line widths and peak velocities of transitions with the same K quantum number are strongly correlated to their rest frequencies: for higher J quantum numbers, the lines become gradually broader and more blueshifted. Those trends indicate that the CH_3CCH lines are indeed tracing different components of the gas, and that the warmer region—associated with higher-frequency transitions—is likely under stronger turbulence effects.
- By comparing the correlation between the line widths and the peak velocities, we observe that the $K=0$ transitions present a different kinematic signature than the rest of the lines. Thus, these transitions seem to be tracing a slightly different region than the bulk of the $K\neq0$ lines: a potentially cooler and more extended gas. Surveys of this species with higher angular resolution are also fundamental to further explore the origin of this differentiation.

4.2 *Future perspectives*

A forthcoming paper on the research that was described in this thesis is currently under preparation. We expect to submit it to a peer-review journal on astrophysics by the first trimester of 2021.

As was constantly mentioned in the previous section and throughout §3, higher angular resolution is necessary to properly explore our conclusions. For this reason, the conduction of a spectral survey of CH_3CCH toward G331 using interferometry instruments is paramount. Observations at higher frequencies are also desired in order to verify the intensity behavior of the $K=2$ peaks, and possibly constrain the temperature profile. Accordingly, we plan to submit an observing proposal to ALMA in the near future, hopefully encompassing an even broader frequency range than the current work, and possibly including other promising HMCs additionally to G331.

Moreover, theoretical models of the time-dependent chemical abundances in star-forming regions are extremely useful to explore their evolution. By comparing the theoretical and observed abundances of different molecular species, those models allow to estimate the source's evolutionary stage, providing key information to put together the puzzle-pieces of massive star-formation. Thus, another future perspective of this work is to investigate the chemical network of CH_3CCH in G331. By comparing its observed abundances to related species, such as CCH, we aim to further our knowledge on the age of this source, and hopefully expand those findings to other young star-forming sites.

Bibliography

Abgrall, H., Roueff, E., and Drira, I. (2000). Total transition probability and spontaneous radiative dissociation of B, C, B' and D states of molecular hydrogen. *A&AS*, 141:297–300.

Acharyya, K. and Herbst, E. (2017). Gas-grain Fluorine and Chlorine Chemistry in the Interstellar Medium. *ApJ*, 850(1):105.

Andre, P., Ward-Thompson, D., and Barsony, M. (2000). From Prestellar Cores to Protostars: the Initial Conditions of Star Formation. In Mannings, V., Boss, A. P., and Russell, S. S., editors, *Protostars and Planets IV*, page 59.

Andron, I., Gratier, P., Majumdar, L., Vidal, T. H. G., Coutens, A., Loison, J.-C., and Wakelam, V. (2018). Methyl cyanide (CH_3CN) and propyne (CH_3CCH) in the low-mass protostar IRAS 16293-2422. *MNRAS*, 481(4):5651–5659.

Belitsky, V., Lapkin, I., Fredrixon, M., Meledin, D., Sundin, E., Billade, B., Ferm, S. E., Pavolotsky, A., Rashid, H., Strandberg, M., Desmaris, V., Ermakov, A., Krause, S., Olberg, M., Aghdam, P., Shafiee, S., Bergman, P., De Beck, E., Olofsson, H., Conway, J., De Breuck, C., Immer, K., Yagoubov, P., Montenegro-Montes, F. M., Torstensson, K., Pérez-Beaupuits, J. P., Klein, T., Boland, W., Baryshev, A. M., Hesper, R., Barkhof, J., Adema, J., Bekema, M. E., and Koops, A. (2018). SEPIA - a new single pixel receiver at the APEX telescope. *A&A*, 612:A23.

Belloche, A., Müller, H. S. P., Menten, K. M., Schilke, P., and Comito, C. (2013). Complex organic molecules in the interstellar medium: IRAM 30 m line survey of Sagittarius B2(N) and (M). *A&A*, 559:A47.

Bergin, E. A., Goldsmith, P. F., Snell, R. L., and Ungerechts, H. (1994). CH 3C 2H as a Temperature Probe in Dense Giant Molecular Cloud Cores. *ApJ*, 431:674.

Beuther, H., Zhang, Q., Greenhill, L. J., Reid, M. J., Wilner, D., Keto, E., Shinnaga, H., Ho, P. T. P., Moran, J. M., Liu, S. Y., and Chang, C. M. (2005). Line Imaging of Orion KL at 865 μm with the Submillimeter Array. *ApJ*, 632(1):355–370.

Bisschop, S. E., Jørgensen, J. K., van Dishoeck, E. F., and de Wachter, E. B. M. (2007). Testing grain-surface chemistry in massive hot-core regions. *A&A*, 465(3):913–929.

Blake, G. A., Sutton, E. C., Masson, C. R., and Phillips, T. G. (1987). Molecular Abundances in OMC-1: The Chemical Composition of Interstellar Molecular Clouds and the Influence of Massive Star Formation. *ApJ*, 315:621.

Bøgelund, E. G., Barr, A. G., Taquet, V., Ligterink, N. F. W., Persson, M. V., Hogerheijde, M. R., and van Dishoeck, E. F. (2019). Molecular complexity on disc scales uncovered by ALMA. Chemical composition of the high-mass protostar AFGL 4176. *A&A*, 628:A2.

Bonnell, I. A. and Bate, M. R. (2002). Accretion in stellar clusters and the collisional formation of massive stars. *MNRAS*, 336(2):659–669.

Bonnell, I. A., Bate, M. R., Clarke, C. J., and Pringle, J. E. (2001). Competitive accretion in embedded stellar clusters. *MNRAS*, 323(4):785–794.

Bonnell, I. A., Bate, M. R., and Zinnecker, H. (1998). On the formation of massive stars. *MNRAS*, 298(1):93–102.

Bottinelli, S., Ceccarelli, C., Neri, R., Williams, J. P., Caux, E., Cazaux, S., Lefloch, B., Maret, S., and Tielens, A. G. G. M. (2004). Near-Arcsecond Resolution Observations of the Hot Corino of the Solar-Type Protostar IRAS 16293-2422. *ApJ*, 617(1):L69–L72.

Brogan, C. L., Hunter, T. R., Cyganowski, C. J., Chandler, C. J., Friesen, R., and Indebetouw, R. (2016). The Massive Protostellar Cluster NGC 6334I at 220 au Resolution: Discovery of Further Multiplicity, Diversity, and a Hot Multi-core. *ApJ*, 832(2):187.

Bronfman, L., Alvarez, H., Cohen, R. S., and Thaddeus, P. (1989). A Deep CO Survey of Molecular Clouds in the Southern Milky Way. *ApJS*, 71:481.

Bronfman, L., Casassus, S., May, J., and Nyman, L. Å. (2000). The radial distribution of OB star formation in the Galaxy. *A&A*, 358:521–534.

Bronfman, L., Garay, G., Merello, M., Mardones, D., May, J., Brooks, K. J., Nyman, L.-Å., and Güsten, R. (2008). Discovery of an Extremely High Velocity, Massive, and Compact Molecular Outflow in Norma. *ApJ*, 672(1):391–397.

Buhl, D. and Snyder, L. E. (1973). The Detection of MM-Wave Transition of Methlacetylene. In Gordon, M. A. and Snyder, L. E., editors, *Molecules in the Galactic Environment*, page 187.

Burgdorf, M., Orton, G., van Cleve, J., Meadows, V., and Houck, J. (2006). Detection of new hydrocarbons in Uranus' atmosphere by infrared spectroscopy. *Icarus*, 184(2):634–637.

Calcutt, H., Willis, E. R., Jørgensen, J. K., Bjerkeli, P., Ligterink, N. F. W., Coutens, A., Müller, H. S. P., Garrod, R. T., Wampfler, S. F., and Drozdovskaya, M. N. (2019). The ALMA-PILS survey: propyne (CH_3CCH) in IRAS 16293-2422. *A&A*, 631:A137.

Caselli, P. and Myers, P. C. (1995). The Line Width–Size Relation in Massive Cloud Cores. *ApJ*, 446:665.

Caswell, J. L. and Haynes, R. F. (1987). Southern HII regions : an extensive study of radio recombination lineemission. *A&A*, 171:261–276.

Cazaux, S., Tielens, A. G. G. M., Ceccarelli, C., Castets, A., Wakelam, V., Caux, E., Parise, B., and Teyssier, D. (2003). The Hot Core around the Low-mass Protostar IRAS 16293-2422: Scoundrels Rule! *ApJ*, 593(1):L51–L55.

Ceccarelli, C. (2005). Observations of low-mass protostars: Cold envelopes and hot corinos. *Proceedings of the International Astronomical Union*, 1(S231):1–16.

Cerqueira, H. B. A., Santos, J. C., Fantuzzi, F., Ribeiro, F. d. A., Rocco, M. L. M., Oliveira, R. R., and Rocha, A. B. (2020). Structure, stability, and spectroscopic properties of small acetonitrile cation clusters. *The Journal of Physical Chemistry A*, 124(34):6845–6855. PMID: 32702984.

Cesaroni, R. (2005). Hot molecular cores. In Cesaroni, R., Felli, M., Churchwell, E., and Walmsley, M., editors, *Massive Star Birth: A Crossroads of Astrophysics*, volume 227, pages 59–69.

Cesaroni, R., Felli, M., Testi, L., Walmsley, C. M., and Olmi, L. (1997). The disk-outflow system around the high-mass (proto)star IRAS 20126+4104. *A&A*, 325:725–744.

Cesaroni, R., Hofner, P., Walmsley, C. M., and Churchwell, E. (1998). Sub-arcsecond structure of hot cores in the NH_3 (4,4) line. *A&A*, 331:709–725.

Cesaroni, R., Walmsley, C. M., Koempe, C., and Churchwell, E. (1991). Molecular clumps associated with ultra compact HII regions. *A&A*, 252:278.

Churchwell, E. and Hollis, J. M. (1983). The kinetic temperature and CH3CCH column density profiles in SGR B2,Orion and DR 21. *ApJ*, 272:591–608.

Comito, C., Schilke, P., Phillips, T. G., Lis, D. C., Motte, F., and Mehringer, D. (2005). A Molecular Line Survey of Orion KL in the 350 Micron Band. *ApJS*, 156(2):127–167.

Cordiner, M. A., Palmer, M. Y., Nixon, C. A., Irwin, P. G. J., Teanby, N. A., Charnley, S. B., Mumma, M. J., Kisiel, Z., Serigano, J., Kuan, Y. J., Chuang, Y. L., and Wang, K. S. (2015). Ethyl Cyanide On Titan: Spectroscopic Detection and Mapping Using Alma. *ApJ*, 800(1):L14.

de Graauw, T., Feuchtgruber, H., Bezard, B., Drossart, P., Encrenaz, T., Beintema, D. A., Griffin, M., Heras, A., Kessler, M., Leech, K., Lellouch, E., Morris, P., Roelfsema, P. R., Roos-Serote, M., Salama, A., Vandenbussche, B., Valentijn, E. A., Davis, G. R., and Naylor, D. A. (1997). First results of ISO-SWS observations of Saturn: detection of CO_2_, CH_3_C_2_H, C_4_H_2_ and tropospheric H_2_O. *A&A*, 321:L13–L16.

Di Francesco, J., André, P., and Myers, P. C. (2004). Quiescent Dense Gas in Protostellar Clusters: The Ophiuchus A Core. *ApJ*, 617(1):425–438.

Draine, B. T. (2011). *Physics of the Interstellar and Intergalactic Medium.* Princeton University Press.

Dubrulle, A., Boucher, D., Burie, J., and Demaison, J. (1978). Microwave spectra of propyne and its [13c] isotopic species: Refined molecular structure of propyne. *Journal of Molecular Spectroscopy*, 72(1):158 – 164.

Dumke, M. and Mac-Auliffe, F. (2010). The APEX calibration plan: goals, implementation, and achievements. In *Observatory Operations: Strategies, Processes, and Systems III*, volume 7737 of *Proc. SPIE*, page 77371J.

Duronea, N. U., Bronfman, L., Mendoza, E., Merello, M., Finger, R., Reyes, N., Hervías-Caimapo, C., Faure, A., Cappa, C. E., Arnal, E. M., Lépine, J. R. D., Kleiner, I., and Nyman, L. Å. (2019). Cyanoacetylene in the outflow/hot molecular core G331.512-0.103. *MNRAS*, 489(2):1519–1532.

Edgar, R. (2004). A review of Bondi-Hoyle-Lyttleton accretion. *New A Rev.*, 48(10):843–859.

Endres, C. P., Schlemmer, S., Schilke, P., Stutzki, J., and Müller, H. S. P. (2016). The Cologne Database for Molecular Spectroscopy, CDMS, in the Virtual Atomic and Molecular Data Centre, VAMDC. *Journal of Molecular Spectroscopy*, 327:95–104.

Fontani, F., Cesaroni, R., Caselli, P., and Olmi, L. (2002). The structure of molecular clumps around high-mass young stellar objects. *A&A*, 389:603–617.

Fouchet, T., Lellouch, E., Bézard, B., Feuchtgruber, H., Drossart, P., and Encrenaz, T. (2000). Jupiter's hydrocarbons observed with ISO-SWS: vertical profiles of C_2H_6 and C_2H_2, detection of CH_3C_2H. *A&A*, 355:L13–L17.

Galametz, M., Zhang, Z. Y., Immer, K., Humphreys, E., Aladro, R., De Breuck, C., Ginsburg, A., Madden, S. C., Møller, P., and Arumugam, V. (2016). Water, methanol and dense gas tracers in the local ULIRG Arp 220: results from the new SEPIA Band 5 Science Verification campaign. *MNRAS*, 462(1):L36–L40.

Galván-Madrid, R., Liu, H. B., Zhang, Z. Y., Pineda, J. E., Peng, T. C., Zhang, Q., Keto, E. R., Ho, P. T. P., Rodríguez, L. F., Zapata, L., Peters, T., and De Pree, C. G. (2013). MUSCLE W49: A Multi-Scale Continuum and Line Exploration of the Most Luminous Star Formation Region in the Milky Way. I. Data and the Mass Structure of the Giant Molecular Cloud. *ApJ*, 779(2):121.

Garay, G. and Lizano, S. (1999). Massive Stars: Their Environment and Formation. *PASP*, 111(763):1049–1087.

García, P., Bronfman, L., Nyman, L.-Å., Dame, T. M., and Luna, A. (2014). Giant Molecular Clouds and Massive Star Formation in the Southern Milky Way. *ApJS*, 212(1):2.

Garrod, R. T. and Herbst, E. (2006). Formation of methyl formate and other organic species in the warm-up phase of hot molecular cores. *A&A*, 457(3):927–936.

Genzel, R. (1991). Physical conditions and heating/cooling processes in high mass star formation regions. In Lada, C. J. and Kylafis, N. D., editors, *The Physics of Star Formation and Early Stellar Evolution*. Springer Netherlands.

Giannetti, A., Leurini, S., Wyrowski, F., Urquhart, J., Csengeri, T., Menten, K. M., König, C., and Güsten, R. (2017). ATLASGAL-selected massive clumps in the inner Galaxy. V. Temperature structure and evolution. *A&A*, 603:A33.

Gibb, A. G., Wyrowski, F., and Mundy, L. G. (2004). High-Velocity Gas toward Hot Molecular Cores: Evidence for Collimated Outflows from Embedded Sources. *ApJ*, 616(1):301–318.

Goldsmith, P. F. and Langer, W. D. (1999). Population Diagram Analysis of Molecular Line Emission. *ApJ*, 517(1):209–225.

Gomez, Y., Garay, G., and Lizano, S. (1995). Warm Molecular Gas Associated with Cometary H II Regions. *ApJ*, 453:727.

Gordy, W. and Cook, R. L. (1984). *Microwave molecular spectra*. John Wiley & Sons.

Güsten, R., Nyman, L. Å., Schilke, P., Menten, K., Cesarsky, C., and Booth, R. (2006). The Atacama Pathfinder EXperiment (APEX) - a new submillimeter facility for southern skies -. *A&A*, 454:L13–L16.

Guzmán, A. E., Guzmán, V. V., Garay, G., Bronfman, L., and Hechenleitner, F. (2018). Chemistry of the High-mass Protostellar Molecular Clump IRAS 16562-3959. *ApJS*, 236(2):45.

Hatchell, J., Fuller, G. A., Millar, T. J., Thompson, M. A., and Macdonald, G. H. (2000). SCUBA imaging of high mass star formation regions. *A&A*, 357:637–650.

Heaton, B. D., Little, L. T., and Bishop, I. S. (1989). THE “ultracompact hot core” of G 34.3+0.15 : arcsecond resolution ammonia observations. *A&A*, 213:148–154.

Heays, A. N., Visser, R., Gredel, R., Ubachs, W., Lewis, B. R., Gibson, S. T., and van Dishoeck, E. F. (2014). Isotope selective photodissociation of N_2 by the interstellar radiation field and cosmic rays. *A&A*, 562:A61.

Herbst, E. and van Dishoeck, E. F. (2009). Complex Organic Interstellar Molecules. *ARA&A*, 47(1):427–480.

Hervías-Caimapo, C., Merello, M., Bronfman, L., Åke-Nyman, L., Garay, G., Lo, N., Evans, Neal J., I., López-Calderón, C., and Mendoza, E. (2019). ALMA Observations of the Massive Molecular Outflow G331.512-0.103. II. Physical Properties, Kinematics, and Geometry Modeling. *ApJ*, 872(2):200.

Herzberg, G. (1945). *Molecular Spectra And Molecular Structure. Volume II.* D. Van Nostrand Company, Inc.

Hickson, K. M., Wakelam, V., and Loison, J.-C. (2016). Methylacetylene (CH_3CCH) and propene (C_3H_6) formation in cold dense clouds: A case of dust grain chemistry. *Molecular Astrophysics*, 3:1–9.

Hofner, P., Wyrowski, F., Walmsley, C. M., and Churchwell, E. (2000). A $C^{17}O$ Survey toward Ultracompact H II Regions. *ApJ*, 536(1):393–405.

Hollas, M. (2004). *Modern Spectroscopy.* john Wiley & Sons.

Hollis, J. M., Snyder, L. E., Blake, D. H., Lovas, F. J., Suenram, R. D., and Ulich, B. L. (1981). New interstellar molecular transitions in the 2 millimeter range. *ApJ*, 251:541–548.

Hunter, T. R., Brogan, C. L., Cyganowski, C. J., and Young, K. H. (2014). Subarcsecond Imaging of the NGC 6334 I(N) Protocluster: Two Dozen Compact Sources and a Massive Disk Candidate. *ApJ*, 788(2):187.

Keto, E. (2002). On the Evolution of Ultracompact H II Regions. *ApJ*, 580(2):980–986.

Keto, E. (2003). The Formation of Massive Stars by Accretion through Trapped Hypercompact H II Regions. *ApJ*, 599(2):1196–1206.

Krumholz, M. R. (2006). High Mass Star Formation by Gravitational Collapse of Massive Cores. *arXiv e-prints*, pages astro–ph/0607429.

Krumholz, M. R. and Bonnell, I. A. (2007). Models for the Formation of Massive Stars. *arXiv e-prints*, page arXiv:0712.0828.

Krumholz, M. R., Cunningham, A. J., Klein, R. I., and McKee, C. F. (2010). Radiation Feedback, Fragmentation, and the Environmental Dependence of the Initial Mass Function. *ApJ*, 713(2):1120–1133.

Krumholz, M. R., Klein, R. I., and McKee, C. F. (2011). Radiation-hydrodynamic Simulations of the Formation of Orion-like Star Clusters. I. Implications for the Origin of the Initial Mass Function. *ApJ*, 740(2):74.

Krumholz, M. R., McKee, C. F., and Klein, R. I. (2005). The formation of stars by gravitational collapse rather than competitive accretion. *Nature*, 438(7066):332–334.

Kuiper, R. and Yorke, H. W. (2013). On the Effects of Optically Thick Gas (Disks) around Massive Stars. *ApJ*, 763(2):104.

Kuiper, T. B. H., Kuiper, E. N. R., Dickinson, D. F., Turner, B. E., and Zuckerman, B. (1984). Methyl acetylene as a temperature probe for dense interstellar clouds. *ApJ*, 276:211–220.

Lada, C. J. and Kylafis, N. D. (1999). *The Origin of Stars and Planetary Systems*. Springer, Dordrecht.

Levine, I. N. (1975). *Molecular Spectroscopy*. John Wiley & Sons.

Li, X., Heays, A. N., Visser, R., Ubachs, W., Lewis, B. R., Gibson, S. T., and van Dishoeck, E. F. (2013). Photodissociation of interstellar N_2. *A&A*, 555:A14.

Linnartz, H., Ioppolo, S., and Fedoseev, G. (2015). Atom addition reactions in interstellar ice analogues. *International Reviews in Physical Chemistry*, 34(2):205–237.

Lovas, F. J. (2004). NIST Recommended Rest Frequencies for Observed Interstellar Molecular Microwave Transitions-2002 Revision. *Journal of Physical and Chemical Reference Data*, 33:177–355.

Lovas, F. J., Johnson, D. R., Buhl, D., and Snyder, L. E. (1976). Millimeter emission lines in Orion A. *ApJ*, 209:770–777.

Maret, S., Hily-Blant, P., Pety, J., Bardeau, S., and Reynier, E. (2011). Weeds: a CLASS extension for the analysis of millimeter and sub-millimeter spectral surveys. *A&A*, 526:A47.

Mauersberger, R., Henkel, C., Walmsley, C. M., Sage, L. J., and Wiklind, T. (1991). Dense gas in nearby galaxies. V. Multilevel studies of CH3CCH and CH3CN. *A&A*, 247:307.

Mauersberger, R., Wilson, T. L., and Henkel, C. (1988). A multilevel study of ammonia in a star-forming regions. IV. Emissionand absorption toward W3 (OH). *A&A*, 201:123–130.

McGuire, B. A. (2018). 2018 Census of Interstellar, Circumstellar, Extragalactic, Protoplanetary Disk, and Exoplanetary Molecules. *ApJS*, 239(2):17.

McKee, C. F. and Tan, J. C. (2003). The Formation of Massive Stars from Turbulent Cores. *ApJ*, 585(2):850–871.

McLaughlin, D. E. and Pudritz, R. E. (1997). Gravitational Collapse and Star Formation in Logotropic and Nonisothermal Spheres. *ApJ*, 476(2):750–765.

Mendoza, E., Bronfman, L., Duronea, N. U., Lépine, J. R. D., Finger, R., Merello, M., Hervías-Caimapo, C., Gama, D. R. G., Reyes, N., and Åke-Nyman, L. (2018). G331.512-0.103: An Interstellar Laboratory for Molecular Synthesis. I. The Ortho-to-para Ratios for CH_3OH and CH_3CN. *ApJ*, 853(2):152.

Merello, M., Bronfman, L., Garay, G., Lo, N., Evans, Neal J., I., Nyman, L.-Å., Cortés, J. R., and Cunningham, M. R. (2013a). ALMA Observations of the Massive Molecular Outflow G331.512-0.103. *ApJ*, 774(1):L7.

Merello, M., Bronfman, L., Garay, G., Nyman, L.-Å., Evans, Neal J., I., and Walmsley, C. M. (2013b). Physical Characteristics of G331.5-0.1: The Luminous Central Region of a Giant Molecular Cloud. *ApJ*, 774(1):38.

Millar, T. J. and Freeman, A. (1984). Chemical modelling of molecular sources - I. TMC-1. *MNRAS*, 207:405–423.

Millar, T. J. and Williams, D. A. (1988). *Rate Coefficients in Astrochemistry. Proceedings of a Conference held in UMIST, Manchester, United Kingdom, September 21-24, 1987.*, volume 146. Springer Netherlands.

Milligan, T. A. (2005). *Modern Antenna Design*. John Wiley & Sons.

Mills, I. M. (1972). *Molecular Spectroscopy: Modern Research*. Academic Press, Inc.

Molinari, S., Merello, M., Elia, D., Cesaroni, R., Testi, L., and Robitaille, T. (2016). Calibration of Evolutionary Diagnostics in High-mass Star Formation. *ApJ*, 826(1):L8.

Muenter, J. S. and Laurie, V. W. (1966). Deuterium isotope effects on molecular dipole moments by microwave spectroscopy. *The Journal of Chemical Physics*, 45(3):855–858.

Myers, P. C. and Fuller, G. A. (1992). Density Structure and Star Formation in Dense Cores with Thermal and Nonthermal Motions. *ApJ*, 396:631.

Nagy, Z., van der Tak, F. F. S., Fuller, G. A., and Plume, R. (2015). Physical and chemical differentiation of the luminous star-forming region W49A. Results from the JCMT Spectral Legacy Survey. *A&A*, 577:A127.

Neufeld, D. A., Falgarone, E., Gerin, M., Godard, B., Herbst, E., Pineau des Forêts, G., Vasyunin, A. I., Güsten, R., Wiesemeyer, H., and Ricken, O. (2012). Discovery of interstellar mercapto radicals (SH) with the GREAT instrument on SOFIA. *A&A*, 542:L6.

Nyman, L. Å., Lerner, M., Nielbock, M., Anciaux, M., Brooks, K., Chini, R., Albrecht, M., Lemke, R., Kreysa, E., Zylka, R., Johansson, L. E. B., Bronfman, L., Kontinen, S., Linz, H., and Stecklum, B. (2001). SIMBA explores the southern sky. *The Messenger*, 106:40–44.

Öberg, K. I., Boamah, M. D., Fayolle, E. C., Garrod, R. T., Cyganowski, C. J., and van der Tak, F. (2013). The Spatial Distribution of Organics toward the High-mass YSO NGC 7538 IRS9. *ApJ*, 771(2):95.

Offner, S. S. R., Kratter, K. M., Matzner, C. D., Krumholz, M. R., and Klein, R. I. (2010). The Formation of Low-mass Binary Star Systems Via Turbulent Fragmentation. *ApJ*, 725(2):1485–1494.

Osorio, M., Lizano, S., and D'Alessio, P. (1999). Hot Molecular Cores and the Formation of Massive Stars. *ApJ*, 525(2):808–820.

Papousek, D. and Aliev, M. R. (1982). *Molecular Vibrational Rotational Spectra*. Elsevier.

Pickett, H. M., Poynter, R. L., Cohen, E. A., Delitsky, M. L., Pearson, J. C., and Müller, H. S. P. (1998). Submillimeter, millimeter and microwave spectral line catalog. *J. Quant. Spec. Radiat. Transf.*, 60:883–890.

Plume, R., Jaffe, D. T., Evans, Neal J., I., Martín-Pintado, J., and Gómez-González, J. (1997). Dense Gas and Star Formation: Characteristics of Cloud Cores Associated with Water Masers. *ApJ*, 476(2):730–749.

Puzzarini, C. (2017). Astronomical complex organic molecules: Quantum chemistry meets rotational spectroscopy. *International Journal of Quantum Chemistry*, 117(2):129–138.

Puzzarini, C. and Barone, V. (2020). The challenging playground of astrochemistry: an integrated rotational spectroscopy - quantum chemistry strategy. *Physical Chemistry Chemical Physics (Incorporating Faraday Transactions)*, 22(12):6507–6523.

Puzzarini, C., Stanton, J. F., and Gauss, J. (2010). Quantum-chemical calculation of spectroscopic parameters for rotational spectroscopy. *International Reviews in Physical Chemistry*, 29(2):273–367.

Qasim, D., Fedoseev, G., Chuang, K. J., He, J., Ioppolo, S., van Dishoeck, E. F., and Linnartz, H. (2020). An experimental study of the surface formation of methane in interstellar molecular clouds. *Nature Astronomy*, 4:781–785.

Qasim, D., Fedoseev, G., Lamberts, T., Chuang, K.-J., He, J., Ioppolo, S., Kästner, J., and Linnartz, H. (2019). Alcohols on the Rocks: Solid-State Formation in a H3CC≡CH + OH Cocktail under Dark Cloud Conditions. *ACS Earth and Space Chemistry*, 3(6):986–999.

Qiu, J., Zhang, J., Zhang, Y., Jia, L., and Tang, X. (2020). $\lambda = 2$ mm spectroscopy observations toward the circumnuclear disk of NGC 1068. *A&A*, 634:A125.

Qiu, K., Zhang, Q., Megeath, S. T., Gutermuth, R. A., Beuther, H., Shepherd, D. S., Sridharan, T. K., Testi, L., and De Pree, C. G. (2008). Spitzer IRAC and MIPS Imaging of Clusters and Outflows in Nine High-Mass Star Forming Regions. *ApJ*, 685(2):1005–1025.

Roberts, H., van der Tak, F. F. S., Fuller, G. A., Plume, R., and Bayet, E. (2011). Dense molecular gas towards W49A: a template for extragalactic starbursts? *A&A*, 525:A107.

Russeil, D., Schneider, N., Anderson, L. D., Zavagno, A., Molinari, S., Persi, P., Bontemps, S., Motte, F., Ossenkopf, V., André, P., Arzoumanian, D., Bernard, J. P., Deharveng, L., Didelon, P., Di Francesco, J., Elia, D., Hennemann, M., Hill, T., Könyves, V., Li, J. Z., Martin, P. G., Nguyen Luong, Q., Peretto, N., Pezzuto, S., Polychroni, D., Roussel, H., Rygl, K. L. J., Spinoglio, L., Testi, L., Tigé, J., Vavrek, R., Ward-Thompson, D., and White, G. (2013). The Herschel view of the massive star-forming region NGC 6334. *A&A*, 554:A42.

Rybicki, G. B. and Lightman, A. P. (1985). *Radiative Processes in Astrophysics*. Wiley-VCH.

Sadaghiani, M., Sánchez-Monge, Á., Schilke, P., Liu, H. B., Clarke, S. D., Zhang, Q., Girart, J. M., Seifried, D., Aghababaei, A., Li, H., Juárez, C., and Tang, K. S. (2020). Physical properties of the star-forming clusters in NGC 6334. A study of the continuum dust emission with ALMA. *A&A*, 635:A2.

Santos, J. C., Rocha, A. B., and Oliveira, R. R. (2020). Rotational spectrum simulations of asymmetric tops in an astrochemical context. *Journal of Molecular Modeling*, 26(278).

Schiff, H. I. and Bohme, D. K. (1979). An ion-molecule scheme for the synthesis of hydrocarbon-chain and organonitrogen molecules in dense interstellar clouds. *ApJ*, 232:740–746.

Schmidt, D. R. and Ziurys, L. M. (2019). Exotic Carbon Chemistry in a Planetary Nebula: The Unusual Case of K4-47. *ApJ*, 881(2):L38.

Shu, F. H. (1977). Self-similar collapse of isothermal spheres and star formation. *ApJ*, 214:488–497.

Shu, F. H., Adams, F. C., and Lizano, S. (1987). Star formation in molecular clouds: observation and theory. *ARA&A*, 25:23–81.

Silva, A., Zhang, Q., Sanhueza, P., Lu, X., Beltran, M. T., Fallscheer, C., Beuther, H., Sridharan, T. K., and Cesaroni, R. (2017). SMA Observations of the Hot Molecular Core IRAS 18566+0408. *ApJ*, 847(2):87.

Stahler, S. W., Shu, F. H., and Taam, R. E. (1980). The evolution of protostars. I - Global formulation and results. *ApJ*, 241:637–654.

Tan, J. C. (2018). Fire from Ice - Massive Star Birth from Infrared Dark Clouds. *IAU Symposium*, 332:139–152.

Tan, J. C., Beltrán, M. T., Caselli, P., Fontani, F., Fuente, A., Krumholz, M. R., McKee, C. F., and Stolte, A. (2014). Massive Star Formation. In Beuther, H., Klessen, R. S., Dullemond, C. P., and Henning, T., editors, *Protostars and Planets VI*, page 149.

Taniguchi, K., Herbst, E., Caselli, P., Paulive, A., Maffucci, D. M., and Saito, M. (2019). Cyanopolyyne Chemistry around Massive Young Stellar Objects. *ApJ*, 881(1):57.

Taniguchi, K., Saito, M., Majumdar, L., Shimoikura, T., Dobashi, K., Ozeki, H., Nakamura, F., Hirota, T., Minamidani, T., Miyamoto, Y., and Kaneko, H. (2018). Chemical Diversity in Three Massive Young Stellar Objects Associated with 6.7 GHz CH_3OH Masers. *ApJ*, 866(2):150.

Tielens, A. G. G. M. (2005). *The Physics and Chemistry of the Interstellar Medium.* Cambridge University Press.

Townes, C. H. and Schawlow, A. L. (1975). *Microwave Spectroscopy.* Dover Publications.

Turner, B. E., Terzieva, R., and Herbst, E. (1999). The Physics and Chemistry of Small Translucent Molecular Clouds. XII. More Complex Species Explainable by Gas-Phase Processes. *ApJ*, 518(2):699–732.

van Dishoeck, E. F. (2014). Astrochemistry of dust, ice and gas: introduction and overview. *Faraday Discussions*, 168:9.

van Dishoeck, E. F. and Black, J. H. (1988). The Photodissociation and Chemistry of Interstellar CO. *ApJ*, 334:771.

Vassilev, V., Meledin, D., Lapkin, I., Belitsky, V., Nyström, O., Henke, D., Pavolotsky, A., Monje, R., Risacher, C., Olberg, M., Strandberg, M., Sundin, E., Fredrixon, M., Ferm, S. E., Desmaris, V., Dochev, D., Pantaleev, M., Bergman, P., and Olofsson, H. (2008). A Swedish heterodyne facility instrument for the APEX telescope. *A&A*, 490(3):1157–1163.

Vastel, C., Ceccarelli, C., Lefloch, B., and Bachiller, R. (2014). The Origin of Complex Organic Molecules in Prestellar Cores. *ApJ*, 795(1):L2.

Visser, R., van Dishoeck, E. F., Doty, S. D., and Dullemond, C. P. (2009). The chemical history of molecules in circumstellar disks. I. Ices. *A&A*, 495(3):881–897.

Walmsley, C. M., Cesaroni, R., Olmi, L., Churchwell, E., and Hofner, P. (1995). The Massive Hot Core Associated with G31.41+0.31. *Ap&SS*, 224(1-2):173–175.

Wang, P., Li, Z.-Y., Abel, T., and Nakamura, F. (2010). Outflow Feedback Regulated Massive Star Formation in Parsec-Scale Cluster-Forming Clumps. *ApJ*, 709(1):27–41.

Western, C. M. (2017). PGOPHER: A program for simulating rotational, vibrational and electronic spectra. *J. Quant. Spec. Radiat. Transf.*, 186:221–242.

Williams, D. A. and Cecchi-Pestellini, C. (2016). *The Chemistry of Cosmic Dust*. The Royal Society of Chemistry.

Wilson, T., Rohlfs, K., and Huettemeister, S. (2009). *Tools of Radio Astronomy*. Springer-Verlag Berlin Heidelberg.

Wyrowski, F., Schilke, P., Walmsley, C. M., and Menten, K. M. (1999). Hot Gas and Dust in a Protostellar Cluster near W3(OH). *ApJ*, 514(1):L43–L46.

Zahorecz, S., Jimenez-Serra, I., Testi, L., Immer, K., Fontani, F., Caselli, P., Wang, K., and Toth, L. V. (2017). Gas versus solid-phase deuterated chemistry: HDCO and D_2CO in massive star-forming regions. *A&A*, 602:L3.

Zhang, C.-P., Wang, J.-J., Xu, J.-L., Wyrowski, F., and Menten, K. M. (2014). Submillimeter Array and Very Large Array Observations in the Hypercompact H II Region G35.58-0.03. *ApJ*, 784(2):107.

Zhang, Q., Sridharan, T. K., Hunter, T. R., Chen, Y., Beuther, H., and Wyrowski, F. (2007). A jet-like outflow toward the high-mass (proto) stellar object IRAS 18566+0408. *A&A*, 470(1):269–279.

Zinnecker, H. and Yorke, H. W. (2007). Toward Understanding Massive Star Formation. *ARA&A*, 45(1):481–563.

Appendix

Appendix A

Total spectrum of G331

A.1 Here we present the total spectrum of G331, including the observations conducted with the SEPIA180, APEX-1 and APEX-2 receivers of the APEX 12 m telescope.

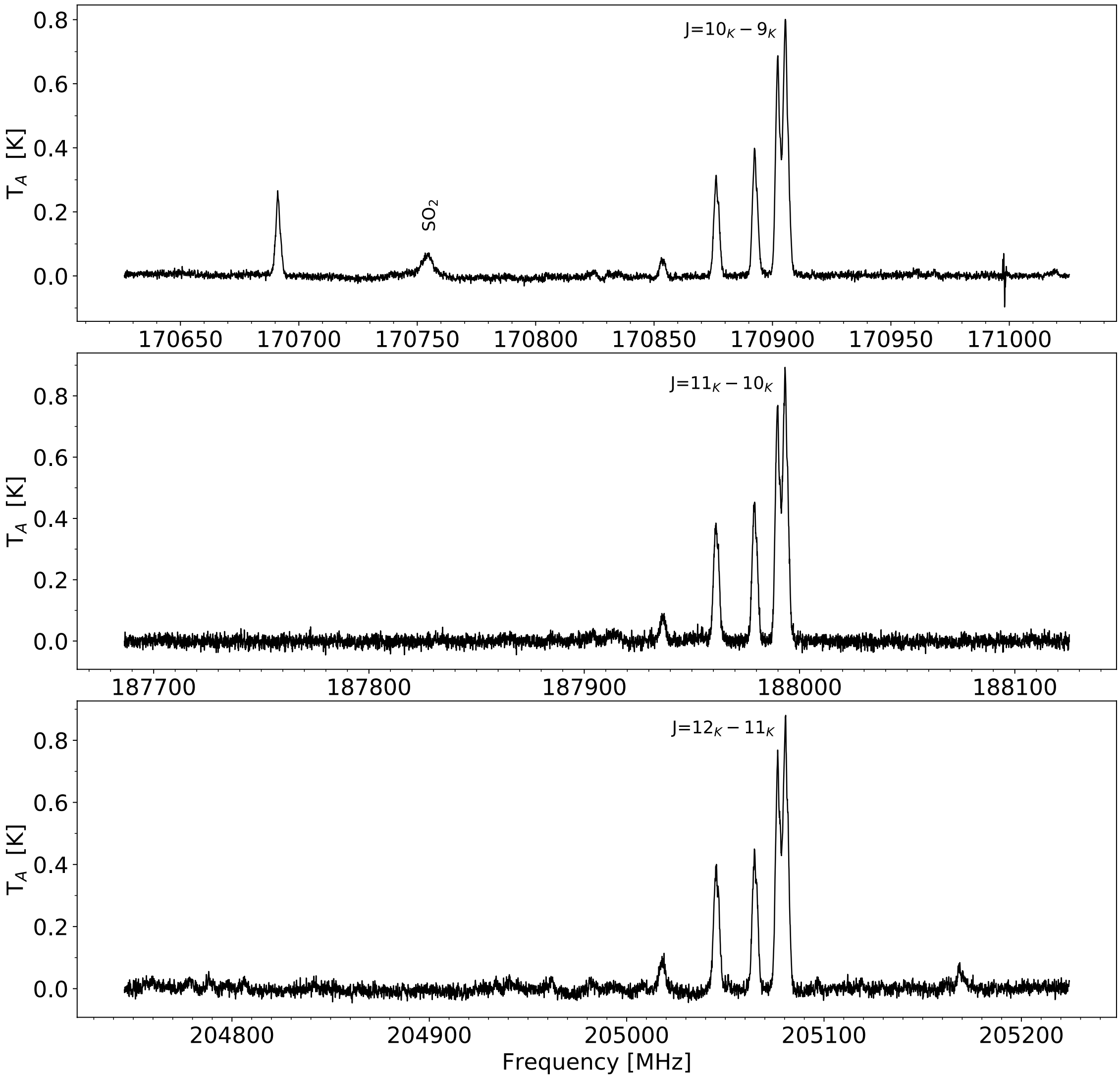

Figure A.1: Spectral bands: ∼170630–171030 MHz; ∼187690–188130 MHz; ∼204750–205220 MHz

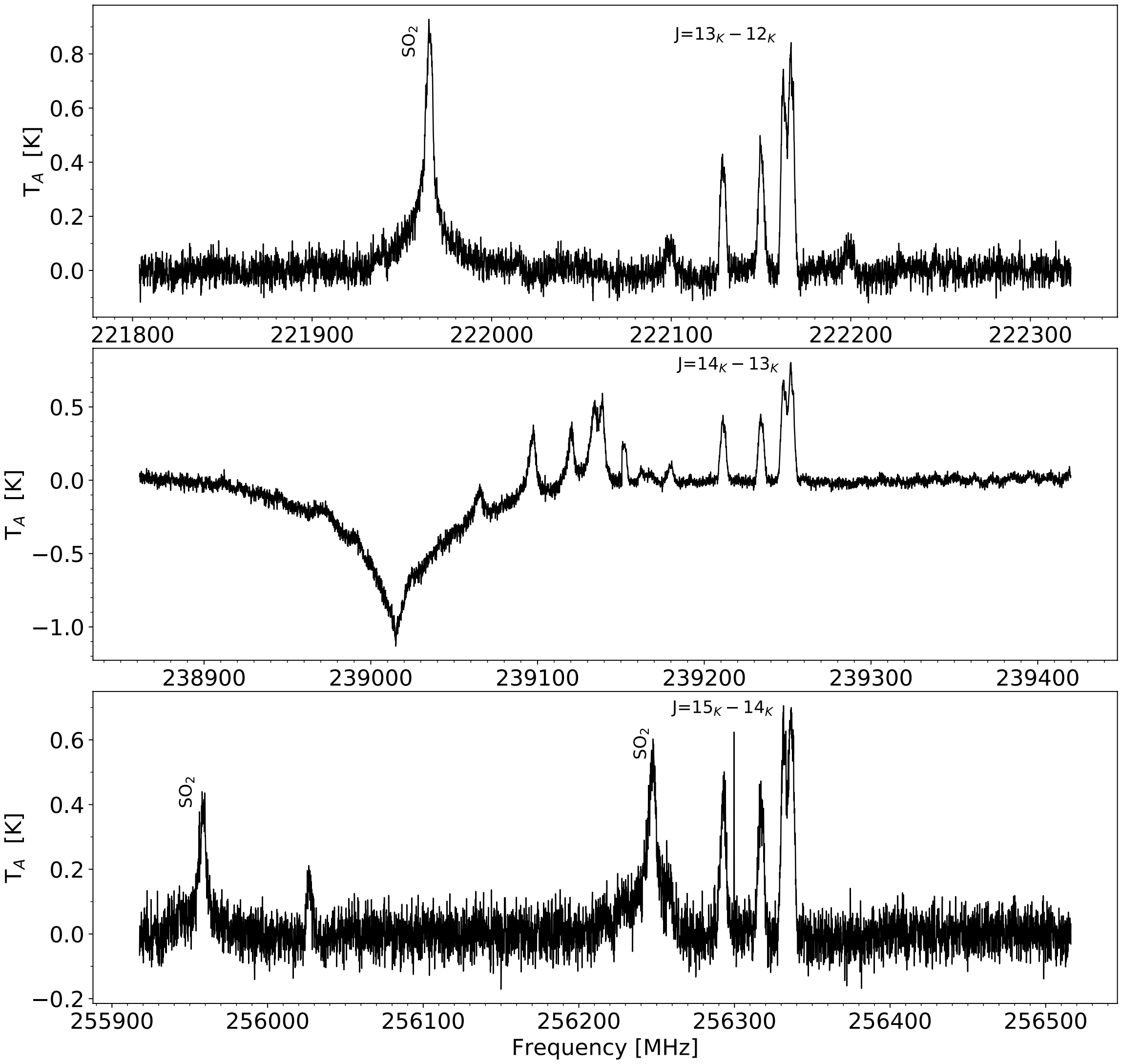

Figure A.2: Spectral bands: ~221800–222320 MHz; ~238840–239430 MHz; ~255920–256520 MHz

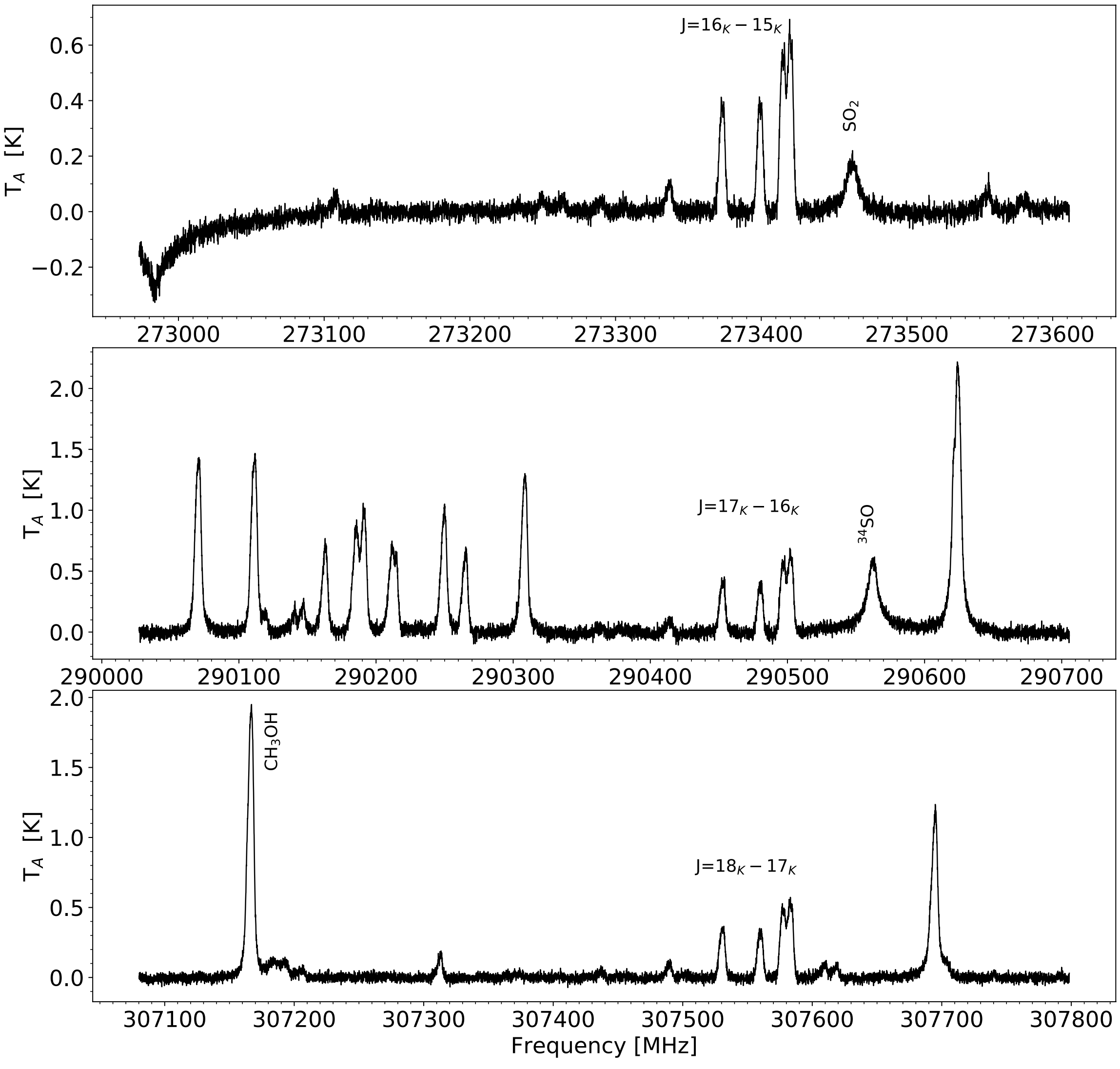

Figure A.3: Spectral bands: ∼272970–273610 MHz; ∼290030–290710 MHz; ∼307080–307800 MHz